Numerical simulation of a three-stage Stirling-type pulse-tube refrigerator

Numerical Simulation of a Three-stage Stirling-type Pulse-Tube Refrigerator

Mohammad Ali Etaati

Numerical Simulation of a Three-stage Stirling-type Pulse-Tube Refrigerator

PROEFSCHRIFT

ter verkrijging van de graad van doctor aan de
Technische Universiteit Eindhoven, op gezag van de
rector magnificus, prof.dr. C.J. van Duijn, voor een
commissie aangewezen door het College
voor Promoties in het openbaar te verdedigen
op woensdag 22 juni 2011 om 16.00 uur

door

Mohammad Ali Etaati

geboren te Shiraz, Iran

Dit proefschrift is goedgekeurd door de promotoren:

prof.dr. R.M.M. Mattheij
en
prof.dr. A.T.A.M. de Waele

Copromotor:
dr.ir. A.S. Tijsseling

To my parents

Contents

Summary

The pulse-tube refrigerator (PTR) is a rather new device for cooling down to extremely low temperatures, i.e. below 4 K. The PTR works by the cyclic compression and expansion of helium that flows through a regenerator made of porous material, a cold heat exchanger, a tube, a hot heat exchanger and an orifice, in series. In a Stirling-type PTR compression and expansion are generated by a piston. The compression increases the temperature of the helium in the tube and makes it flow towards the orifice; the expansion decreases the temperature and makes the helium flow backwards to the regenerator. The net effect of warmer helium flowing in one direction and colder helium in the opposite direction is that of cooling power at the cold heat exchanger. Three PTRs are inter-connected aiming to obtain the desired 4 K lowest temperature.

The conservation laws of mass, momentum and energy, and an equation of state, are simplified using asymptotic analysis based on low Mach-numbers. The regenerator is modelled one-dimensionally with Darcy's law for flow resistance. The tube is modelled either one-dimensionally without resistance or two-dimensionally with axisymmetric laminar viscous flow. The heat transfer in the porous medium of the regenerator and in the solid tube wall is taken into account. The gas can be either ideal or real. All the material properties, including viscosity and conductivity, are taken temperature and pressure dependent. Three single-stage PTRs are connected with the regenerators in series and the tubes in parallel and six flow possibilities at the junctions are considered. Three by-passes (double-inlets) are used to enhance and tune the performance.

The governing equations are numerically solved with a finite-difference method of nominally second-order accuracy in space and time. Pressure correction, flux limiter, 1D-2D connections and domain decomposition are the keywords here. Special attention is paid to suitable initial conditions, high resolution in the boundary layers and to the correct calculation of the three-way junctions in multi-stage PTRs.

The model describes the fluid dynamics and thermodynamics of the pulse tubes and regenerators. The heat exchangers are assumed to be ideal in the whole analysis. The equation of state for real gas and other real properties of gas and regenerator material, which are temperature and/or pressure dependent, are applied in the three-stage PTR which works with extreme low temperatures, where the ideal gas law does not hold.

The numerical methods require special attention. Typically for flow problems we deal with various length scales. Straight forward discretisation will result in unnecessary fine grids and therefore unacceptable computational time. We developed robust and efficient algorithms to deal with boundary layer problems. The employed domain de-

composition technique allows for using coarse grids in areas where the solution does not change significantly. It also decouples a larger system into smaller ones, leading to smaller complexities.

The objective of computing accurately and efficiently the steady oscillatory flow and heat transfer in a PTR has been achieved. In particular the tiny viscous and thermal boundary layers of a PTR operating at high frequency (20 Hz) could be resolved. The simulated three-stage PTR was able to cool down close to 5 K. The developed software is intended for use in design and optimisation of multi-stage PTRs.

Samenvatting

De pulsbuiskoeler is een relatief nieuwe uitvinding om af te koelen naar extreem lage temperaturen, dat is onder 4 Kelvin. De pulsbuiskoeler werkt aan de hand van de periodieke samendrukking en uitzetting van helium dat achtereenvolgens stroomt door een regenerator gemaakt van poreus materiaal, een koude warmtewisselaar, een buis, een hete warmtewisselaar en een uitstroomopening naar een reservoir. In een pulsbuiskoeler van het Stirling type zorgt een zuiger voor het samendrukken en weer uitzetten van het helium. Het samendrukken verhoogt de temperatuur van het helium in de buis en geeft een stroming in de richting van de uitstroomopening. Bij het uitzetten stroomt het helium terug naar de regenerator. Het netto effect van warmer helium stromend in de ene richting en kouder helium stromend in de andere richting is dat van koelend vermogen in de koude warmtewisselaar. Drie pulsbuiskoelers zijn aan elkaar gekoppeld om zo een gewenste laagste temperatuur van 4 Kelvin te bereiken.

De behoudswetten van massa, impuls en energie, en een toestandsvergelijking, zijn vereenvoudigd in een asymptotische analyse gebaseerd op kleine getallen van Mach. De regenerator is eendimensionaal gemodelleerd met Darcy's wet voor stromingsweerstand. De buis is zowel eendimensionaal gemodelleerd zonder weerstand als tweedimensionaal met axiaalsymmetrische laminaire viskeuze stroming. Het warmtetransport in het poreuze medium van de regenerator en in de stalen buiswand zijn daarbij in rekening gebracht. Het gas zelf is ideaal of reel. Alle materiaaleigenschappen, waaronder viscositeit en warmtegeleiding, zijn temperatuur- en drukafhankelijk genomen. Drie pulsbuiskoelers zijn samengevoegd met de regeneratoren in serie en de pulsbuizen parallel, waarbij zes stromingsmogelijkheden bij de drie-weg verbindingsstukken zijn beschouwd. Drie bypasses (dubbele inlaten) zijn gebruikt om de efficiency te verhogen en te optimaliseren.

De geldende vergelijkingen worden numeriek opgelost met een eindige-differentie methode van nominaal tweede-orde nauwkeurigheid in plaats en tijd. Drukcorrectie, "flux limiter", 1D-2D verbindingen en domeindecompositie zijn hierbij de trefwoorden. Bijzondere aandacht wordt besteed aan geschikte beginvoorwaarden, hoge resolutie in de grenslagen en de correcte berekening van de drie-weg verbindingsstukken in meertraps pulsbuiskoelers.

Het model beschrijft de vloeistof- en thermodynamica van pulsbuizen en regeneratoren. De warmtewisselaars zijn ideaal verondersteld in de hele analyse. De toestandsvergelijking van een reel gas en andere rele eigenschappen van gas- en regeneratormateriaal, zijnde temperatuur- en/of drukafhankelijk, worden gebruikt in de drie-traps pulsbuis-

koeler. Deze werkt immers met extreem lage temperaturen, waar de ideale gaswet niet meer geldt.

De numerieke methoden vragen bijzondere aandacht. Kenmerkend voor stromingsproblemen hebben we te maken met verschillende lengteschalen. Rechttoe rechtaan discretisatie zal resulteren in onnodig fijne roosters en daardoor onacceptabele rekentijden. We hebben robuuste en efficinte algoritmes ontwikkeld die de grenslaagproblematiek verdisconteren. De gebruikte domeindecompositie techniek staat het gebruik van grove roosters toe in gebieden waar de oplossing niet beduidend verandert. Het splitst tevens een groter systeem op in kleinere, wat leidt tot lagere rekencomplexiteit.

Het doel om stationair oscillerende stromingen en warmtetransport in een pulsbuiskoeler nauwkeurig en efficint te berekenen is bereikt. In het bijzonder kunnen de smalle viskeuze en thermische grenslagen worden berekend van pulsbuiskoelers draaiend met hoge frequentie (20 Hertz). De gesimuleerde drie-traps pulsbuiskoeler was in staat om af te koelen tot nabij de 5 Kelvin. De ontwikkelde software is bedoeld voor gebruik bij het ontwerpen en optimaliseren van meer-traps pulsbuiskoelers.

Chapter 1

Introduction

1.1 The pulse-tube refrigerator: general background and applications

Cryogenics comes from the Greek word "kryos", which means cold, and "genein", which means to produce. Cryogenics can be described as the branch of physics and engineering that involves the study of producing temperatures in the range from practically zero to, say, 125 K and of material behaviour at these temperatures. A *cryocooler* is a refrigeration machine that reaches temperatures below, say, 125 K with a small refrigeration capacity.

Reliability of small cryocoolers is a topic that has been studied for many years. One way to increase reliability is the elimination of moving parts in mechanical refrigerators. A typical machine used for cryocooling is a Stirling refrigerator [46]. Stirling refrigerators have two moving parts only: the compressor piston and the displacer. In 1963 a refrigeration technique that eliminates the displacer from the Stirling machine was discovered [30]. This new technique was called *pulse tube refrigeration* (PTR). The first design was based on a tube with one end closed, see Figure 1.1. The closed end is connected to a heat exchanger to release heat to the environment. Heat exchange between gas, tube wall and the two heat exchangers makes a temperature difference develop in the tube such that the open end cools down and the closed end heats up. Due to its simplicity and the enhanced reliability, the pulse-tube refrigerator has become one of the most important innovations in the field of cryogenics. The main advantage of this new device, as compared to the conventional *Stirling* or *Gifford-McMahon* (GM) systems, is the ability to reach low temperatures without moving parts in the low temperature zone. These moving parts in conventional coolers need oil lubrication and maintenance. This first type of cooler nowadays is called the basic pulse-tube refrigerator (B-PTR). In 1984 the machine was improved by adding an orifice and a reservoir to the hot end of the tube, open end, so that the efficiency increased significantly [52]. See Fig. 2.1. This
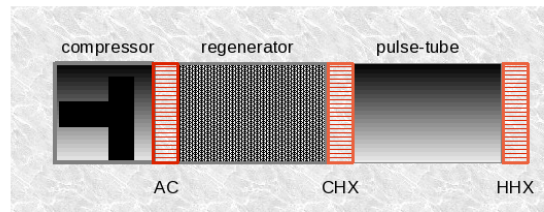
Figure 1.1: Basic pulse-tube refrigerator with the compressor, the regenerator, the tube, the cold heat exchanger (CHX), the hot heat exchanger (HHX), the after cooler (AC).

system is referred to as "orifice pulse-tube refrigerator". This important modification initiated and stimulated further research in the field of cryogenic engineering. In [62] an improvement to the pulse tube refrigerator by adding a second inlet, connecting the compressor of the system to the hot end of the pulse-tube directly via a bypass, is reported. It was shown how to make the refrigeration power per unit mass flow higher. The essential elements of the Stirling-type pulse-tube refrigerator, especially the tube and the regenerator, will be explained in detail in Chapter 2. In Figure 1.2 a typical single-stage pulse tube refrigerator made by the 'Stirling Cryogenics and Refrigeration B.V.' is shown.

Pulse-tube cryocoolers are used in industrial applications such as semiconductor fabrication and in military applications such as the cooling of infrared sensors. Pulse-tubes are also being developed for the cooling of astronomical detectors where liquid *cryogens* are typically used, such as the Atacama Cosmology Telescope. Pulse tubes will be particularly useful in space-based telescopes where it is impossible to replenish the cooling agents as they are depleted. The largest commercial application of cryocoolers has been in cryopumps for the semiconductor fabrication industry. These cryopumps require a few Watts of refrigeration at a temperature of about 15 K to cool a charcoal adsorbent bed and a few tens of Watts at about 80 K to cryopump mostly water vapour [58]. Large pulse-tube refrigerators are also being developed for the liquefaction of natural gas, for clean-burning fuel in fleet vehicles and for liquefaction of the methane-rich gas emitted from landfills of large cities [58]. In medicine the pulse-tube refrigeration technology is used to cool superconducting magnets in diagnostic imaging systems (MRI), thereby replacing the conventional liquid-helium bath. This improves the quality of images due to the reduction of vibration and it makes MRI systems smaller and cheaper.

1.2   Modelling approaches for Stirling-type PTR

A variety of models exists for studying the pulse-tube refrigerator [48]. Below we review a few of them.

Harmonic analysis is a simple but efficient way of analysing the fluid flow and thermodynamic behaviour in the pulse tube. All variables are expanded in harmonic terms.
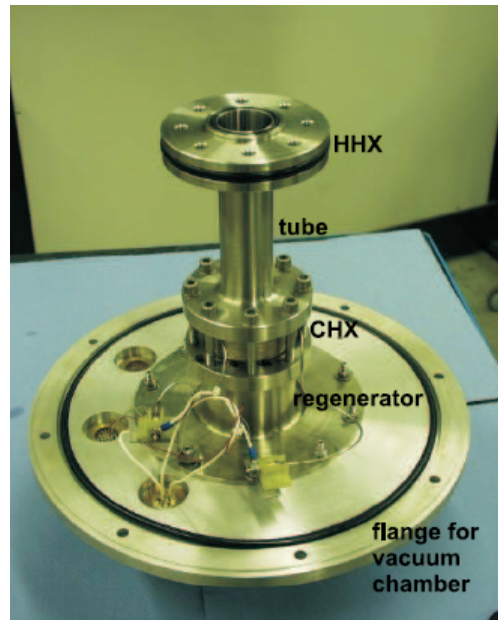
Figure 1.2: A pulse-tube refrigerator made by 'Stirling Cryogenics and Refrigeration B.V.', with the regenerator, the pulse tube, the cold heat exchanger (CHX), the hot heat exchanger (HHX) [79].

The obtained first-order differential equations are solved with standard numerical techniques such as Runge-Kutta integration. The method is used for quick optimisation of the pulse tube in terms of the geometry parameters, distribution of the various materials, orifice settings, etc. This method is restricted to small amplitude harmonic pressure variations [9], [12], [36].

Thermodynamic models [59], [8], [9–12, 15–19], [43], [54], [65] provide a way to analyse the performance of the PTR using the basic laws of thermodynamics. They are used to predict the behaviour of the regenerator, the pulse tube and their adjacent heat exchangers to determine the enthalpy flow through the whole system. General relationships for the entropy production in the components of the pulse tubes, which have a wide range of validity, are derived. The thermodynamic models are time-averaged per cycle. These models explain precisely how pulse-tube refrigerators cool down.

Fluid dynamics models [81], [64] are used to predict the behaviour of the gas flowing in the pulse tube refrigerator by analytical solutions after some simplification of the governing equations. Two-dimensional models for the pulse tube are used to accommodate the tube wall effects caused by friction and heat transfer, cf. [3, 4, 57].

In practice one has to use numerical tools to compute the various quantities appearing in these models, cf. [41], [47], [37], [80], [79]. The conservation laws are too complex and cannot be solved analytically. The finite volume method was developed in [75] for a PTR with ideal gas, ideal heat exchangers and negligible axial heat conduction. It was shown that the gas flow resistance cannot be neglected since it causes phase and amplitude differences in pressure at different parts of the regenerator. In later pa-

pers [76], [42] it was shown that the opening of the bypass valve in a double-inlet pulse tube refrigerator (DPTR) caused a higher cooling power with lower compressor work than conventional orifice pulse tube refrigerators (OPTs). The performance of 4 K pulse tube coolers, which involves non-ideal gas properties of ^{4}He and special properties of the regenerative material was studied in [72]. Numerical studies on multi-sage PTRs with respect to their performance are reported in [74] and [73], addressing the effect of DC flow on the temperature profile along the regenerator and on the temperature at the cold end. In [37] and [80], 3D simulations of OPTRs and DPTRs were performed, with interests in the effects of gravity, streaming and turbulence.

Because of the complexity of the conservation laws for compressible fluid flow in PTRs, much research has been done using commercial software. The USA Institute of Standards and Technology (NIST) numerical model for PTR simulation known as REGEN, which in fact is not commercial, was applied to simulate a Gifford-McMahon type PTR in [20]. A two-stage PTR was modeled based on one-dimensional theory. Through a series of simulations using REGEN, the lowest temperature was minimised for a two-stage refrigerator. The effect of three different matrix materials was discussed. In [5] a two-dimensional computational fluid dynamic (CFD) simulation of a GM-type double-inlet pulse tube refrigerator (DIPTR), operating under a variety of thermal boundary conditions, was presented. The transient CFD model successfully predicted pulse tube refrigerator functioning. *Sage* is an object orientated commercial software package particularly suited for Stirling-type machine design [29].

This project is a continuation and extension of past work on the numerical simulation of pulse tube refrigerators in the Department of Mathematics and Computer Science (TU/e) [28], [48], [49], [50]. Therefore, some parts had to be repeated to ensure the continuity. The research has been carried out in close cooperation with the Low Temperatures group (LT) at the Department of Applied Physics (TU/e). The LT group started working on the topic about fifteen years ago [9–12, 15–19], resulting in several PhD theses on the theoretical and experimental aspects of pulse-tube refrigerators [35], [65], [67], [78].

1.3   Our objectives

For an efficient PTR the fine-tuning of all its components is imperative and a simulation tool is most helpful in the design phase. The modelling of such systems concerns the development of an accurate mathematical model to simulate a three-stage PTR operating at high frequencies. The model describes the fluid dynamics and thermodynamics of the tubes, regenerators, and the coupling of the three individual stages. There is a number of aspects that makes this problem challenging. For instance steep temperature gradients, viscous and thermal boundary layers, the possible onset of turbulence, and the high operating frequencies. A common feature is the presence of various scales. Indeed, small scales only matter in a limited part of the modelling domain. Yet they tend to govern numerical results everywhere if no special attention is paid to them. As a consequence the required mesh width in a numerical method may be unduly small, and therefore the simulation very time-consuming, if possible at all. This is why existing software for this problem is not directly useful, as has been shown in a previous project,

cf. [48]. Based on this the major task will be to develop new methods dealing with efficiently computing solutions for this type of multiscale problems. We can summarise the main objectives of this project as follows

1. development of a mathematical model for simulating a single-stage pulse-tube refrigerator for the pulse-tube (1D and 2D) and for the regenerator (1D),

2. development of a mathematical model for simulating a three-stage pulse tube refrigerator for the important temperature range around 4 K at high frequencies imposing real gas and temperature/pressure dependent material properties,

3. coupling the 1D model of the regenerator with the 1D and 2D models of the pulse tube,

4. coupling of the three individual stages in a three-stage PTR,

5. imposing the proper physical boundary, interface and initial conditions (IC),

6. imposing IC in such a way as to prevent any unwanted peaks (overshooting) for the gas temperature in the tube, as it appeared in previous work [48], by employing a suitable technique,

7. development and testing of appropriate numerical methods,

8. to apply a 2D domain decomposition method (DD) for high-activity regions to improve computational efficiency,

9. implementation of the developed model in a simulation tool for calculating (among others) the coefficient of performance of the cooling system,

10. to predict the fluid dynamic behaviour of the gas flowing in the PTR, especially the temperature profile in the pulse tube,

11. to calculate the lowest attainable temperature in a three-stage pulse tube refrigerator.

1.4 Outline of the thesis

Chapter 2 describes the physical modelling of a pulse tube refrigerator. The basic principle of the thermodynamic behaviour of the gas inside the pulse tube in terms of the temperature variation versus the pressure variation is explained. The main aspects of the multi-stage PTR are briefly described. The temperature and pressure dependent material properties of the gas together with the temperature dependent properties of the regenerator solid are given.

Chapter 3 presents the mathematical modelling of the fluid flow and heat transfer inside the pulse-tube refrigerator. We assume the fluid to be a continuum and Newtonian, and the flow to be laminar, compressible and unsteady. External forces like gravity are

neglected. The heat exchangers are assumed to operate ideally, which means that the gas flowing out of the heat exchanger takes the heat exchanger's temperature and there is no resistance and heat capacity effect within the heat exchangers. The basic equations are the three laws of conservation and the equation of state. The four unknowns are the density, the velocity, the thermodynamic pressure, and the absolute temperature. Other thermodynamic parameters are: the two transport properties (dynamic viscosity and thermal conductivity) and the specific heat capacity introduced in Chapter 2. We derive the low-Mach number equations governing the fluid flow inside the PTR. One-dimensional formulations for the pulse-tube and the regenerator as well as interface conditions are given. An axisymmetrical two-dimensional formulation is considered for the pulse-tube only so that wall effects due to heat transfer and friction can be investigated. A one-dimensional formulation with non-ideal gas is derived, so that more realistic behaviour of the gas at extremely low temperatures is modelled. Proper junction conditions for multi-stage pulse-tube refrigerators based on the local conservation of mass, momentum and energy are formulated.

Chapter 4 describes the numerical methods that solve governing equations derived in Chapter 3. The first step in obtaining a numerical solution is to discretise the geometric domain, i.e. a numerical grid must be defined. Since the domain of computation in 1D and 2D is of simple shape, a finite difference (FD) method is an appropriate method to discretise the equations. In addition, a domain-decomposition method is applied in the two-dimensional computations for the pulse-tube so that an accurate solution is obtained in an efficient way. The regenerator is still modelled as a 1D domain where the wall effects including friction and heat transfer with the solid are taken into account using the Darcy's law. The ideal gas assumption is not valid for extremely low temperatures. Therefore in the case of multi-stage PTR, where the last regenerator is in such a temperature range, we consider real gas. The numerical methods are validated by a number of studied laminar flow problems.

Chapter 5 gives the numerical results for a typical single-stage PTR. First, we present the one-dimensional results for the velocity and the temperature of the gas in the pulse-tube as well as the gas velocity, gas temperature, regenerator material temperature and pressure in the regenerator. Meanwhile we explain the importance of choosing the initial condition for the temperature in the pulse-tube. Second, we present the two-dimensional results of a typical single-stage PTR (that is 2D pulse-tube and 1D regenerator), where all aspects of friction at and heat transfer with the wall are included. Third, we improve our 2D computations by using the domain decomposition method to increase the efficiency in terms of CPU time complexity and memory storage. Finally, we present the physical efficiency of the PTR in terms of mass and enthalpy flow and we check the coefficient of performance of the system.

Chapter 6 applies the method described before, for the case of non-ideal gas and temperature and/or pressure dependent material properties of the gas and solid, to a low-frequency three-stage PTR with the reported experimental data in order to validate our code. Next, we apply the method to a high-frequency PTR, referred to as the final aim of this project, to investigate the fluid dynamic behaviour of such system in terms of velocity, gas temperature and pressure variation in the pulse tubes and the regenerators. Finally, we show the effect of the non-ideality of the gas on the temperature and other system variables.

Chapter 2

Physical modelling

In this chapter we describe the physical modeling of the pulse-tube refrigerator. The thermodynamic behaviour of the gas inside the pulse tube in terms of the temperature versus the pressure variation of a gas parcel initially inside the regenerator, but moving into and and out of the pulse tube, is explained. The general operation and design of multi-stage PTRs is briefly described. The temperature and pressure dependent material properties of helium and the regenerator solid are given.

2.1 Pulse-tube refrigerator

There are two types of PTRs, Stirling and Gifford-McMahon (GM). In the Stirling machine the pressure oscillation is produced by a compressor which is directly connected
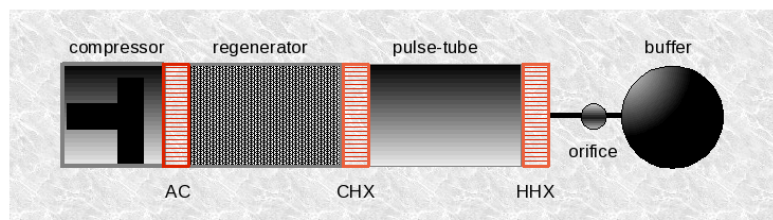
Figure 2.1: Schematic Stirling pulse-tube refrigerator with orifice and buffer.
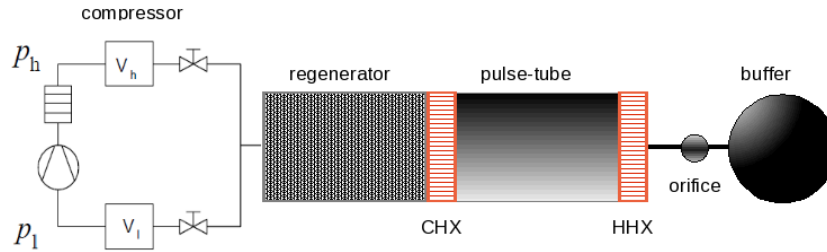
Figure 2.2: Schematic diagram of a Gifford-McMahon cooler. V_l and V_h are buffer volumes of the compressor. The two valves alternatively connect the cooler to the high- and the low-pressure side of the compressor. The two valves are often replaced by rotating one valve.

to the aftercooler, see Figure 2.1, and in GM machine a compressor generates continuously high and low pressures and uses a rotary valve to generate the pressure oscillation, see Figure 2.2. The operational principle of the pulse-tube refrigerator due to the cyclic compression and expansion of a fixed quantity of gas, usually helium, is explained. In the following all essential parts of the system shown in Figure 2.1 are explained [48], [65] and [67].

The *aftercooler* (AC), only exists in a Stirling machine. The heat generated by the compressor during the gas compression is removed by AC. The *regenerator* consists of porous material with a high heat capacity. Its function is to store the heat released by the gas during compression (the gas is moving towards the pulse tube) and to return the heat to the gas during expansion (the gas is moving towards the compressor). The *cold heat exchanger* (CHX) is used to absorb the heat from the object (application) to be cooled and the *hot heat exchanger* (HHX) transports this heat to the surroundings. The HHX is maintained at the ambient temperature often with the aid of an additional cooler. The orifice-type PTR has a *buffer* and an *orifice*. The orifice is a resistance that is tuned for obtaining the most suitable phase difference between the pressure and the gas velocity. The volume of the buffer is large compared to that of the pulse tube; it is typically 10 times larger. The pressure in the buffer is nearly constant and practically equal to the average pressure in the system.

2.1.1 Gas circulation

The thermodynamic and the fluid dynamic behaviour of the heat exchangers is rather complicated. It is necessary to make simplifying assumptions. In an ideal heat exchanger [44] the heat contact between the gas and the matrix is perfect, the flow resistance of the matrix is zero and the thermal conductivity is infinitely large.

Let us now consider two gas parcels at two sides of the tube [48], [65] [67], i.e. one at the HHX and one at the CHX. Schematic drawings of the temperature-position curves
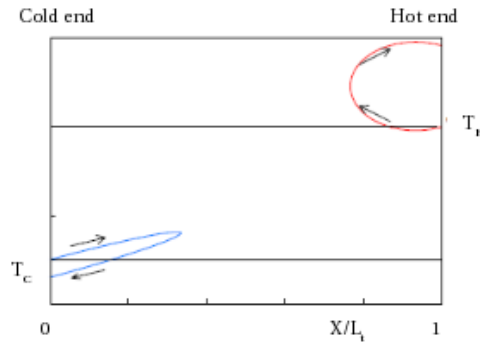
Figure 2.3: Left side: A gas parcel enters the tube at temperature T_C and leaves it at a lower temperature producing cooling. Right side: A gas element enters the tube at temperature T_H and leaves it at a higher temperature producing heating.

of two gas parcels, for a sinusoidal pressure wave, are given in Fig. 2.3. At the HHX the gas parcel flows with a temperature T_H from the buffer into the tube as long as the pressure in the tube, P_t, is smaller than the pressure inside the buffer, P_b, i.e. $P_t < P_b$. At a certain time $P_t = P_b$ and the gas parcel stops moving, and subsequently with pressure increment in the tube, i.e. $P_t > P_b$, the gas moves back towards the hot end of the tube. The final pressure is larger than the initial pressure and consequently the final temperature will be higher than the initial temperature T_H. Pressure and flow velocity are directly related via the orifice resistance.

The analysis of the situation at the CHX is more complicated due to the fact that the velocity at the cold end is determined by the velocity of the gas at the hot end and the compression of the gas column in the tube. However the principle is basically the same. At the cold end the gas parcel enters the tube at a high pressure and at a temperature T_C and leaves it at a low pressure and hence with a temperature below T_C which produces cooling. One full cycle results in net enthalpy flow from the cold end to the hot end. This cooling mechanism at the cold end can also be explained by means of Figure 2.4. We consider the following idealised pressure-time and temperature-position of a gas parcel near the CHX. Figure 2.4.a shows the pressure variation in the tube with the following four steps

Step 1. The compression step. While the orifice is closed the pressure in the pulse tube rises from the low pressure p_L to the high pressure p_H by moving the piston to the right.
Step 2. The orifice is open and the piston still moves to the right. The gas flows from the tube to the buffer. The pressure in the tube remains at the value of p_H and the pressure in the buffer increases slightly.
Step 3. The expansion step. At this stage the orifice is closed and the piston moves to the left. The pressure in the pulse tube decreases from p_H to p_L.
Step 4. The piston still moves to the left while the orifice is open. Now the pressure in

(a) pressure cycle   (b) temperature cycle
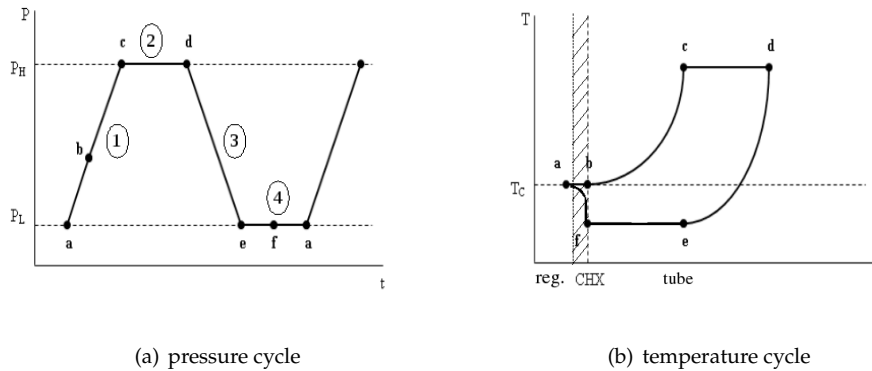
Figure 2.4: Pressure and temperature of a gas parcel as a function of time and position ([65], Fig. 2.7).

the buffer is higher than the pressure in the pulse tube. So the gas flows from the buffer into the tube, but the pressure in the tube remains constant at p_L.

We now follow a gas parcel, which is inside the regenerator at the start of the cycle (point **a**) at pressure p_L and temperature T_C, see Figure 2.4.b.

Step 1. From **a** to **b** when the pressure rises the gas element moves to the right. Due to the good thermal contact with the regenerator material the temperature of the element follows the temperature of the regenerator. At point **b** the gas element leaves the regenerator and enters the pulse tube via the heat exchanger CHX with temperature T_C. From **b** to **c** the gas element is thermally isolated from its surroundings (adiabatic process) and by increasing the pressure its temperature rises.

Step 2. From **c** to **d** the gas element still moves to the right. The pressure is constant and so is the temperature.

Step 3. At point **d** the gas parcel stops moving to the right. The pressure drops, and the gas parcel moves to the left. As it is thermally isolated the temperature drops together with the pressure. Since some amount of gas is already in this stage stuck in the buffer, the gas parcel gets a lower temperature than the initial one, T_C.

Step 4. From **e** to **f** the gas parcel moves to the left at constant pressure. The temperature is constant as long as the gas element is inside the tube. At point **f** the gas element leaves the pulse tube and enters the heat exchanger CHX with the temperature $T < T_C$. The gas then extracts heat (produces cooling) from the CHX to reach the regenerator temperature T_C. From **f** to **a** the gas parcel is inside the CHX and moves with a lower temperature T and then T_C back to its initial position in the regenerator.

2.1.2 Double-inlet PTR

In the *double-inlet* PTR the hot end of the pulse tube is connected to the entrance (hot end) of the regenerator by an orifice adjusted to an optimal value [62]. See Fig. 2.5. The double inlet is a bypass for the regenerator and the pulse tube and as such reduces the cooling power. In addition it is a dissipative device which further deteriorates the performance. However, both these disadvantages are overcome by the fact that the optimised double inlet reduces the flow and thus the dissipation in the regenerator. As a result the over-all system performance can be improved significantly. The first orifice and the double-inlet orifice are two adjustable valves for each stage of the PTR. For a three-stage system the number of valves then need to be adjusted and optimised is six. The adjustment of all these valves in the development phase in the laboratory takes a lot of patience and skill of the PTR-operator.
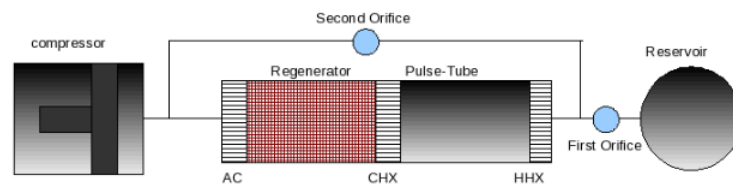
Figure 2.5: Schematic picture of a single-stage PTR with double-inlet orifice.

2.1.3 Three-stage pulse-tube refrigerator

To reach temperatures below 15 K it is not practical to use a single-stage PTR. A multi-stage PTR is unavoidable as has been shown in experimental cryogenics literature [17], [68]. Basically one PTR can be used to precool another. Figure 2.6 shows a photo of a three-stage PTR taken in the laboratory of the Applied Physics Department of TU Eind-hoven. Figure 2.7 is a schematic picture of a three-stage PTR. There are three pulse-tubes in parallel with corresponding orifices, buffers and heat exchangers, three regenerators in series, one compressor and three double-inlets. According to this set-up, the first tube is the shortest and the thickest and the third one is the thinnest and the longest. The first regenerator is made of stainless steel, the second one of lead and the third one of Erbium-Nickel (ErNi). The three regenerators have different porosity and permeability. The lengths of the regenerators are approximately the same. The parameters used for optimising the system mainly are the geometry and the material properties, e.g. the
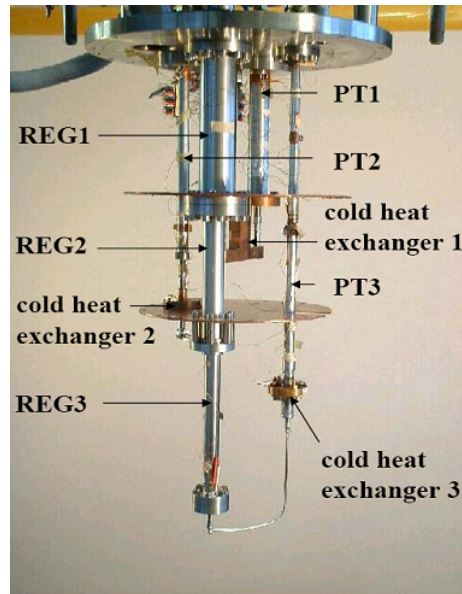
Figure 2.6: Three-stage Stirling pulse-tube refrigerator [67].

volume of the buffers and the conductance of the orifices. The final aim of a design is to maximise the cooling power and to minimise the input power for a given lowest temperature. The pressure variation produced by the compressor plays an important role and is in the range of 8-25 bar. The disadvantage of multi-staging is that precooling reduces the flow to the next stage, hence the cooling power is less [67].

2.1.4 Flow and heat straighteners

In practice the pulse-tube at HHX is connected via the orifice to the buffer through tubes. See Figure 2.8. At the cold end the pulse tube and the regenerator are connected by a tube too [67]. At such junctions, there are narrow-wide connections which may cause turbulent eddies at the entrances of the wide tubes. See Fig. 2.9.a. Therefore, *flow straighteners* are used to prevent such undesired eddies which might decrease the efficiency of the system. They are intended to make the flow in both the pulse tube and the regenerator (porous medium) uniformly parallel and the heat transfer perfect. These straighteners also make the temperature uniform if the flow is dominated by convection. See Fig. 2.9.b.

As we can see in Fig. 2.7 there are flow straighteners at the entrance of each regenerator for the three-stage PTR. Fig. 2.10 shows a zoom at junction I of Fig. 2.7. The connecting tube is linked into a gap in between the regenerators I and II. After this gap at both sides there are straighteners that uniformly distribute the flow and heat into the regenerators to prevent any probable eddy at the entrances.

Figure 2.7: Schematic three-stage Stirling pulse-tube refrigerator.

Figure 2.8: Single-stage PTR with connecting tubes.

(a) without straightener

(b) with straightener
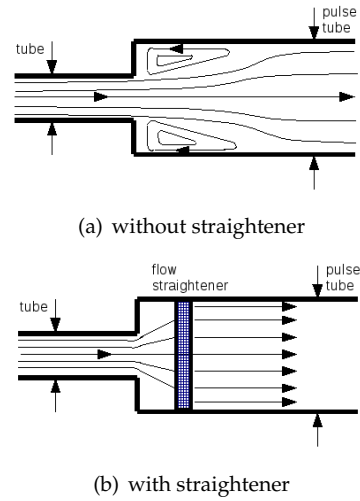
Figure 2.9: The gas flows from the small tube into the pulse-tube a) without straightener, b) with the straightener.

(a) zoom of junction I of Fig. 2.7

(b) construction of the 2nd stage regenerator [67]
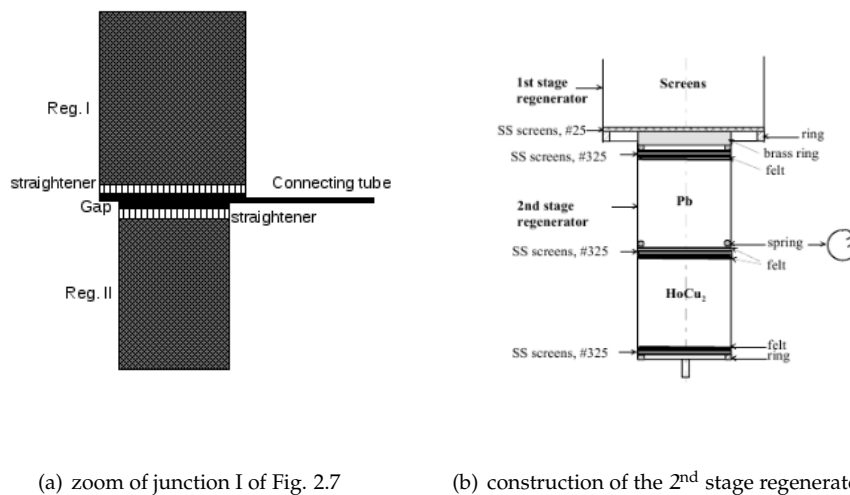
Figure 2.10: Zoom of junction I of Fig. 2.7 showing the gap and two straighteners at both sides.
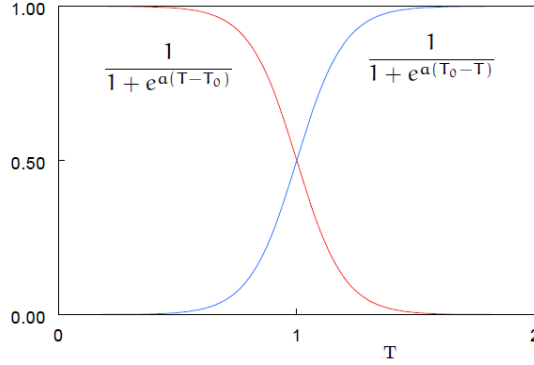
Figure 2.11: The functions f_L and f_H of T. In this example we have chosen $a = 10$ and $T_0 = 1$.

2.2 Temperature and pressure dependent material properties

The properties of gases vary with temperature and pressure. Pulse-tube refrigerators are able to cool down to about 2 K in one tube in the case of multi-stage PTR where the hot end is at room temperature. Therefore, we need to consider the temperature and/or pressure dependent gas/material properties. Such properties are the specific heat capacity c_p, thermal conductivity κ and viscosity μ of the gas together with specific heat capacity C_S and thermal conductivity κ of the solid. Below we give practical values and approximations for the thermal and hydrodynamic properties of ^{4}He [14], [13]. We will frequently use the functions

$$f_L(a, T_0) = \frac{1}{1 + e^{a(T - T_0)}}, \tag{2.2.1}$$

$$f_H(a, T_0) = \frac{1}{1 + e^{a(T_0 - T)}}, \tag{2.2.2}$$

where T is a variable and a and T_0 are constants. The first function is close to to 1 when $T \ll T_0$ and close to zero when $T \gg T_0$. For the second function it is the other way around. The parameter $1/a$ represents the width of the transition and the value of T_0 is the transition temperature. An example is given in Figure 2.11 where $a = 10$ and $T_0 = 1$. These functions are convenient when using symbolic expressions for matching curves in low-temperature and high-temperature ranges. By choosing proper values for the parameters a and T_0 the region of overlap can be fitted to data available in [55] and [66]. Pulse-tube refrigerators usually operate with ^{4}He in the pressure region between 8 and 25 bar. The critical pressure is 2.29 bar at 5 K (see Figure 2.12), so PTRs operate in a region where no liquid-vapour phase transition takes place. Below the λ-line the thermal conductivity becomes practically infinitely large (super fluidity). At temperatures just above the λ-line the thermal expansion coefficient becomes zero. These are the two
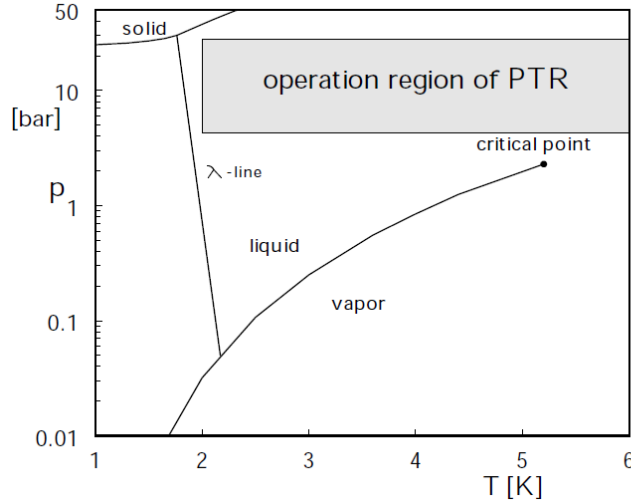
Figure 2.12: Phase diagram of ^{4}He. PTRs, using ^{4}He, operate above 2.1 K in the pressure range between 5 and 25 bar [55], [66]

.

major reasons why it is impossible to cool down below the λ-line using ^{4}He. PTRs operating close to 2 K may hit the λ-line during part of the cooling cycle. The specific heat capacity (c_p) is not constant for a real gas. Using the functions (2.2.1), (2.2.2) and tabulated values measured in the laboratory [55] we can find the following fit for c_p

$$c_p := a_1 + (-a_3 + a_4 T) f_L(1, T_1 - 1) + \frac{a_2}{T^2} f_H(1, T_1), \tag{2.2.3}$$

Here we have approximately (p in MPa)

$$a_1 = 20.76, \tag{2.2.4}$$
$$a_2 = 650p + 125, \tag{2.2.5}$$
$$a_3 = 2p + 16, \tag{2.2.6}$$
$$a_4 = -0.3p + 2.8, \tag{2.2.7}$$
$$T_1 = 6p. \tag{2.2.8}$$

The second term in (2.2.3) gives the high-temperature dependence and the third term the low-temperature dependence. For an ideal gas $c_p = 20.77$ [J/molK], which is about the value of a_1. Since we will use the average pressures of about 15 bar, we use (2.2.9) curve-fitting of the measured temperature-dependent specific heat capacity at that specific pressure. Using (2.2.3) one obtains

$$c_p := 20.76 + (-19 + 2.35T) f_L(1, 8) + \frac{1100}{T^2} f_H(1, 9). \tag{2.2.9}$$

Figure 2.13 shows the plot of the specific heat capacity of ^{4}He at low temperature at 15 bar.
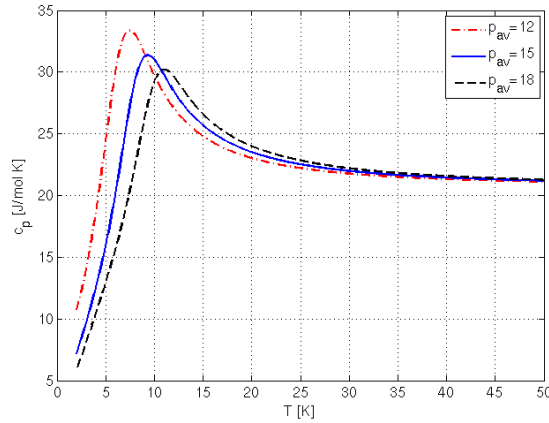
Figure 2.13: Specific heat capacity of helium at low temperature at 12 bar, 15 bar and 18 bar [55], [66].

An expression for the thermal conductivity of ^{4}He at 15 bar in the temperature range 0-300 K is

$$\kappa_{He} := 0.0038T^{0.65} + 0.0172e^{-0.025(T-6)^2}. \tag{2.2.10}$$

Above 40 K may use

$$\kappa_{He} := 0.0038T^{0.65}.$$

If an accuracy of 15% above 20 K is sufficient then the simple relation

$$\kappa_{He} := 0.008\sqrt{T}.$$

can be used. Figure 2.14 shows various approximations of temperature-dependence of ^{4}He conductivity. The dot curve represents the experimental data measured in the laboratory.
An expression for the dynamic viscosity of ^{4}He is

$$\mu_{He} := \left(\frac{29}{T^{1.27}} + 0.52T^{0.64} \right) \times 10^{-6}, \tag{2.2.11}$$

within an accuracy of 0.4 [microPa] [55], [66]. In the temperature range above 20 K the formula

$$\mu := \mu_0 \sqrt{T} \quad \text{with} \quad \mu_0 := 1.05 \times 10^{-6}.$$

can be used, which is about10% accurate. See Figure 2.15. The viscosity does not depend on the pressure.
In the set-up for the three-stage PTR in the low-temperature group (LT) of the Applied Physics Department of TU Eindhoven, the materials in the various stages of the regenerators are stainless steel, lead and ErNi. The thermal conductivity of stainless steel can be approximated by [55], [66]

$$k_{SS} := -0.357255 + 0.132163T - 0.000392T^2 + 4.067913 \times 10^{-7}T^3. \tag{2.2.12}$$
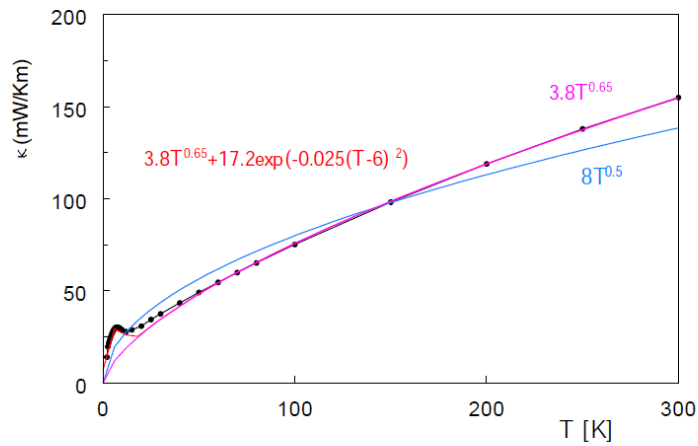
Figure 2.14: Thermal conductivity of ^{4}He as a function of temperature at 15 bar; Dots are measured values [55], [66].
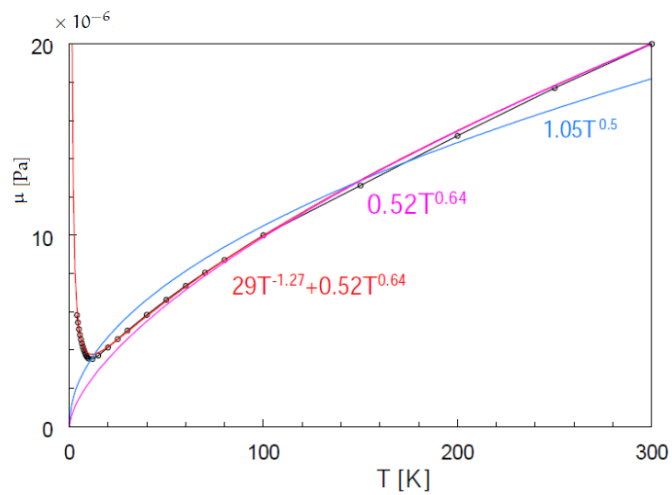
Figure 2.15: Dynamic viscosity of ^{4}He with various approximations; Dots are measured values [55], [66].

The specific heat capacity of stainless steel using the functions (2.2.1), (2.2.2) is

$$c_{SS} := 60 \left(\frac{T}{45} \right)^{1.5} f_L(1,40) + (-745 + 215\ln T) f_H(1, 39.5). \tag{2.2.13}$$

The thermal conductivity of stainless steel can be approximated by

$$\kappa_{Pb} = -34.3 + 24.8T - 2.59T^2 + 0.12T^3 - 0.0031T^4 + 0.00004T^5 - 1.94e^{-7}T^6. \tag{2.2.14}$$

The specific heat capacity of lead has a temperature-dependent behaviour given by

$$c_{Pb} := \frac{0.003T^4}{1 + 0.001T^3} f_L(1,20) + \left(135 - \frac{1650}{T} \right) f_H(1,20). \tag{2.2.15}$$

The thermal conductivity of Erbium-Nickel (ErNi) is given by

$$k_{ErNi} := 1.4T^{0.43}. \tag{2.2.16}$$

The specific heat capacity of ErNi is

$$c_{ErNi} = 1.6T + \frac{175.5}{2.5 + (T - 9.7)^2}. \tag{2.2.17}$$

2.3   Conclusion

In this chapter we have described the physical modeling of the pulse-tube refrigerator. The thermodynamic behaviour of the gas inside the pulse tube in terms of the temperature versus the pressure variation of a gas parcel initially inside the regenerator, but moving into and and out of the pulse tube, has been explained.
New in this chapter is the explanation of the general operation and design of multi-stage PTRs. The physical benefit of the double-inlet in PTRs was described. In addition, the temperature and pressure dependent material properties of helium and the regenerator solid are formulated for the average driving pressure in the system used in Chapter 6, 15 bar. Of course, these properties have been taken from helium property libraries available via commercial software. However, these are black boxes, whereas the formulas prescribed in Section 2.2 give insight, derivatives can be taken and they lead to faster codes.

Chapter 3

Mathematical modelling

In this chapter we derive the mathematical model for the fluid flow and heat transfer inside the pulse-tube refrigerator. We assume the fluid to be a continuum and Newtonian, and the flow to be laminar, compressible and unsteady. External forces like gravity are neglected. The heat exchangers are assumed to operate ideally, which means that the gas flowing out of the heat exchanger takes the heat exchanger's temperature, there is no resistance and the heat capacity of the matrix is much larger than of the gas within the heat exchangers. The basic equations are the three laws of conservation and the equation of state. The four unknowns are the density ρ, the velocity vector $\mathbf{u}$, the thermodynamic pressure p, and the absolute temperature T. Other thermodynamic parameters are: the transport properties μ (dynamic viscosity) and k (thermal conductivity) and the specific heat capacity c_p. These parameters are usually temperature and pressure-dependent as already explained in Chapter 2. In the following we derive the equations governing the fluid flow inside the PTR. One-dimensional formulations for the pulse-tube and the regenerator with connecting interface conditions are given. An axisymmetrical two-dimensional formulation is considered for the pulse-tube so that wall effects due to heat transfer and friction can be investigated. A one-dimensional formulation for the pulse tube and the regeneartor with non-ideal gas is derived so that more realistic behaviour of the gas at extremely low temperatures is modelled. Proper junction conditions are formulated for multi-stage pulse-tube refrigerators based on the local conservation of mass, momentum and energy.

3.1   Basic equations

The basic equations are the three laws of conservation and an equation of state [77]. In the *Eulerian system* description of fluid flow, the three conservation laws utilise the

material derivative defined by

$$\frac{D}{Dt} = \frac{\partial}{\partial t} + (\mathbf{u} \cdot \nabla), \tag{3.1.1}$$

where ρ is the density, $\mathbf{u}$ is the velocity vector and ∇ is the gradient operator.

Conservation of mass: Since the flow is compressible the density is not constant. Therefore, the conservation of mass reads

$$\frac{D\rho}{Dt} + \rho\nabla \cdot \mathbf{u} = 0, \tag{3.1.2}$$

where $(\nabla\cdot)$ is the divergence operator.

Conservation of momentum:
This relation is commonly known as Newton's second law and expresses a proportionality between applied force and the resulting acceleration of a particle of mass m as ($\mathbf{F} = m\mathbf{a}$). For fluid flow it reads

$$\rho\frac{D\mathbf{u}}{Dt} = \rho\mathbf{g} - \nabla p + \nabla \cdot \tau_{ij}, \tag{3.1.3}$$

where $\mathbf{g}$ is the gravitational acceleration, p is the pressure and τ is the viscous stress tensor. This tensor for a Newtonian(linear) fluid is defined by

$$\tau_{ij} = \mu\left(\frac{\partial u_i}{\partial x_j} + \frac{\partial u_j}{\partial x_i}\right) + \delta_{ij}\lambda\nabla \cdot \mathbf{u}, \tag{3.1.4}$$

where δ is the Kronecker delta function ($\delta_{ij} = 1$ if $i = j$ and $\delta_{ij} = 0$ if $i \neq j$), μ is the *dynamic viscosity* and λ, the so-called *bulk viscosity coefficient*, can be found from the *Stokes hypothesis*

$$\lambda + \frac{2}{3}\mu = 0. \tag{3.1.5}$$

Conservation of energy:
The first law of thermodynamics states that the sum of the work applied to and the heat added to a system will result in an increase of the energy of the system. The conservation of energy reads

$$\rho\frac{Dh}{Dt} = \frac{Dp}{Dt} - \nabla \cdot \mathbf{q} + \Phi, \tag{3.1.6}$$

where h is the fluid *enthalpy*, $\mathbf{q}$ is the heat flow per unit area given by *Fourier's law*

$$\mathbf{q} = -k\nabla T, \tag{3.1.7}$$

with T is the temperature, and Φ is the so-called *dissipation function* defined by

$$\Phi = \tau_{ij}\frac{\partial u_i}{\partial x_j}. \tag{3.1.8}$$

The enthalpy for a *non-ideal gas* is defined by

$$Dh = c_p DT + \frac{1}{M}H_p Dp, \tag{3.1.9}$$

where D denotes total derivative, c_p is the specific heat capacity of the gas, and M is the molar mass

$$H_p = V_m - T(\frac{\partial V_m}{\partial T})_p \tag{3.1.10}$$

with V_m the molar volume of the gas. The second term of H_p is the temperature-derivative of the molar volume at constant pressure. For an *ideal gas* the fluid enthalpy h is given by

$$h = c_p T, \tag{3.1.11}$$

Equation of state:
The equation of state for a *non-ideal gas* may be based on various model choices. The *Van der Waals* equation is well known and reads

$$(p + \frac{a}{V_m^2})(V_m - b) = RT, \tag{3.1.12}$$

where R is the gas constant, and a and b are the *Van der Waals coefficients* specified in Appendix B.5. The equation of state for a perfect gas is

$$p = \rho R_m T, \tag{3.1.13}$$

where R_m is the specific gas constant.

3.2 One-dimensional model of a single-stage PTR with ideal gas

The regenerator and the pulse-tube are modelled through partial differential equations. The other parts of the system including the buffer, the orifice, the ideal heat exchangers and the compressor are included in the model as boundary conditions. See Figure 3.1. Finally, the pulse tube and the regenerator are coupled through interface conditions [64], [48].

3.2.1 Pulse-Tube

A one-dimensional model for a tube of length L_t is formulated. In the one-dimensional case the viscous stress tensor has one component, namely

$$\tau_{zz} = 2\mu\frac{\partial u}{\partial z} - \frac{2}{3}\mu(\nabla \cdot u) = \frac{4}{3}\mu\frac{\partial u}{\partial z}. \tag{3.2.1}$$

The one-dimensional heat flux is given by

$$q_z = -k_g\frac{\partial T_g}{\partial z}, \tag{3.2.2}$$
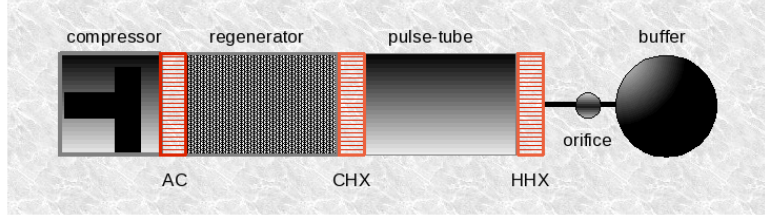
Figure 3.1: Single-stage pulse-tube refrigerator.

where T_g is the gas temperature. To include wall effects in the one-dimensional formulation, we take into account the *skin friction force* in the momentum equation and the wall *heat transfer* in the energy equation. Since there is not an easy way to describe the friction force and heat transfer correlation for 1D oscillating flows, we take the correlations derived from steady laminar flow. Such assumptions are very poor for an unsteady flow problem. However, the 2D model in Section 3.3 automatically includes correct unsteady representations. The friction force at the wall for steady laminar flow is

$$f_{\text{friction}} = -C_f u, \tag{3.2.3}$$

where C_f is the *friction factor* defined by [69]

$$C_f = \frac{32\mu}{D^2}, \tag{3.2.4}$$

with D is the tube diameter. The heat exchanging surface per unit of volume is denoted by *F*, which for a circular tube is 4/D. Then the heat transfer (heat flow) term is defined by

$$E_{\text{heat transfer}} = \alpha F(T_w - T_g), \tag{3.2.5}$$

where α is the heat transfer coefficient, and T_w is the wall temperature. The heat transfer coefficient is given by [38]

$$\alpha := \frac{N_{u_D} k_g}{D} \quad \text{with} \quad N_{u_D} = 3.66, \quad \text{if} \quad T_w = \text{constant.} \tag{3.2.6}$$

The equations for mass, momentum and energy conservation and the equation of state for an ideal gas now take the following form

$$\frac{\partial \rho_g}{\partial t} + \frac{\partial}{\partial z}(\rho_g u) = 0 \quad , \tag{3.2.7}$$

$$\rho_g \left(\frac{\partial u}{\partial t} + u \frac{\partial u}{\partial z} \right) = -\frac{\partial p}{\partial z} + \frac{4}{3} \frac{\partial}{\partial z}\left(\mu \frac{\partial u}{\partial z} \right) - C_f u \quad , \tag{3.2.8}$$

$$\rho_g c_p \left(\frac{\partial T_g}{\partial t} + u \frac{\partial T_g}{\partial z} \right) = \frac{\partial p}{\partial t} + u \frac{\partial p}{\partial z} + \frac{\partial}{\partial z}\left(k_g \frac{\partial T_g}{\partial z} \right) + \frac{4}{3} \mu \left(\frac{\partial u}{\partial z} \right)^2 - \frac{4\alpha}{D}(T_w - T_g) \quad , \tag{3.2.9}$$

$$p = \rho_g R_m T_g, \tag{3.2.10}$$

where $0 \leq z \leq L_t$, CHX is at $z = 0$ and HHX at $z = L_t$. See Figure 3.1. The subscript 'g' represents the gas. Since our basic flow equations are difficult to analyse, we concentrate on casting them into an accessible form. This is accomplished by non-dimensionalising the equations and the boundary conditions, which not only yields a minimum number of flow parameters but also places them in the right context. To make the equations non-dimensional, there are many ways to choose the scaling values. The scaling parameters (indicated by a bar) have typical values for the PTR under consideration. Since we are not interested in acoustic analysis we scale the time by choosing $1/\omega$ (the time for one pressure oscillation divided by 2π, which is the dominant physical time-scale), where ω is the angular frequency of the piston oscillation. Let $\bar{u}$ be the amplitude of the axial velocity variation. The length is then scaled by $\bar{u}/\omega$ (which is a measure for the distance traveled by the fluid in one pressure cycle). The dimensionless variables and parameters (indicated by a hat) are now

$$\rho_g = \bar{\rho}_g \hat{\rho}_g, \quad T_g = T_a \hat{T}_g, \quad , \quad p = p_{av} \hat{p}, \quad u = \bar{u} \hat{u}, \quad t = \hat{t}/\omega, \quad z = (\bar{u}/\omega)\hat{z},$$
$$\mu = \bar{\mu} \hat{\mu}, \quad k_g = \bar{k}_g \hat{k}_g, \quad c_g = \bar{c}_g \hat{c}_g. \tag{3.2.11}$$

where T_a is the ambient temperature, p_{av} is the average pressure in the system, and $\bar{\rho}_g$, $\bar{\mu}$, $\bar{k}_g$ and $\bar{c}_g$ are the density, viscosity, conductivity and specific heat capacity for helium at temperature T_a. It is useful to mention that in [48] the dimensionless variable for the pressure is defined by $p = p_{av} + \bar{p}\hat{p}$,where p_{av} is the average pressure and $\bar{p}$ is the pressure amplitude. The reason mentioned for that is to avoid cancellation caused by subtracting two nearly equal pressures in the numerical approximation of the pressure gradient. However, in here such problem has been overcome with a better CFL condition in the numerical computations. Consequently, Mach number Ma is defined in a more meaningful manner as in [64].

Omitting the hats for notational convenience, the equations (3.2.7)- (3.2.10) become in non-dimensional form

$$\frac{\partial \rho_g}{\partial t} + \frac{\partial}{\partial z}(\rho_g u) = 0, \tag{3.2.12}$$

$$\rho_g \left(\frac{\partial u}{\partial t} + u \frac{\partial u}{\partial z} \right) = -\frac{1}{Ma^2} \frac{\partial p}{\partial z} + \frac{4}{3Re} \frac{\partial}{\partial z} \left(\mu \frac{\partial u}{\partial z} \right) - C_{ff}\mu u, \tag{3.2.13}$$

$$\rho_g c_p \left(\frac{\partial T_g}{\partial t} + u \frac{\partial T_g}{\partial z} \right) = \frac{\mathcal{B}(\gamma - 1)}{\gamma}\left(\frac{\partial p}{\partial t} + u \frac{\partial p}{\partial z} \right) + \frac{1}{Pe_g} \frac{\partial}{\partial z} \left(k_g \frac{\partial T_g}{\partial z} \right) \tag{3.2.14}$$

$$+ \frac{4}{3} \frac{\mathcal{B}(\gamma - 1)}{\gamma} \frac{Ma^2}{Re} \mu(\frac{\partial u}{\partial z})^2 - \mathcal{A}k_g(T_w - T_g),$$

$$p\mathcal{B} = \rho_g T_g. \tag{3.2.15}$$

The dimensionless numbers are (using $\bar{c}_p - \bar{c}_v = R_m$, where $\bar{c}_v$ is the specific heat capacity at constant volume at room temperature)

$$Re = \frac{\bar{\rho}_g \bar{u}^2}{\bar{\mu}\omega}, \qquad \textit{(Oscillatory Reynolds number)},$$
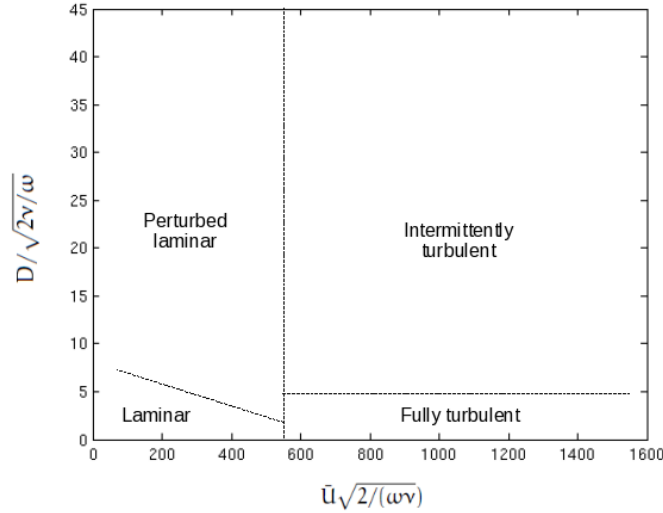
Figure 3.2: Division of reciprocating flow regimes based on observations of turbulence. [22]

$$\text{Pe}_g = \frac{\bar{\rho}_g \bar{u}^2 \bar{c}_p}{\bar{k}_g \omega}, \qquad (\textit{Peclet number}),$$

$$\text{Ma} = \frac{\bar{u}}{\sqrt{p_{av}/\bar{\rho}_g}}, \qquad (\textit{Mach number}),$$

$$\gamma = \frac{\bar{c}_p}{\bar{c}_v}, \qquad (\textit{Specific heat ratio}),$$

$$\frac{\gamma - 1}{\gamma} = \frac{R_m}{\bar{c}_p}, \qquad (\textit{Adiabatic expansion factor}),$$

$$\mathcal{B} = \frac{p_{av}}{\bar{\rho}_g R_m T_a}, \qquad C_{ff} = \frac{32\bar{\mu}}{\bar{\rho}_g \omega D^2}, \qquad \mathcal{A} = \frac{4 N_{u_D} \bar{k}_g}{\bar{\rho}_g \bar{c}_p \omega D^2}.$$

The data for the single-stage and three-stage pulse tube refrigerators and the relevant dimensionless numbers studied herein are given in the Appendixes B1 and B2.

The roles of these dimensionless numbers in the analysis of fluid flow are of great importance [48]. The Reynolds number usually is a reliable criterion to distinguish between laminar flow and the onset of turbulence. Reciprocating flows, or unsteady flows with zero mean, have been the subject of several recent experimental investigations [1], [7], [22], [34], [56]. The experimental results can be summarised to define the stability plane for oscillatory pipe flow, declared in [22], in two-parameter space $\bar{U}\sqrt{2/(\omega \nu)}$ vs *Womersely parameter* $(D/\sqrt{2\nu/\omega})$, which is based on the Stokes layer thickness $\delta = \sqrt{2\nu/\omega}$, where $\bar{U}$ is the the peak velocity, D is the pipe diameter, ω is

the angular frequency and ν is the kinematic viscosity [60]. The outcome of these investigations divides the space into regions of *i) fully laminar flow*; *ii) perturbed laminar flow*; *iii) intermittently turbulent flow*; and *iv) fully turbulent flow*. Figure 3.2 shows the approximate division of this two-parameter space. The PTRs analysed herein operate at frequencies around 20 Hz. With the other dimensionless numbers listed in the Appendixes B and C for the single-stage and three-stage PTR respectively, it is concluded that the flow regimes inside the pulse-tubes and the regenerators are either in the laminar region or in the perturbed laminar region, but not in the turbulent regions. The perturbed laminar flow can be described as appearance of small perturbations in the velocity profile. This perturbation of the velocity amplitude occurs either close to the tube's wall or near the tube's central axis. We assume ideal flow straighteners inside the tube, after CHX and HHX, and inside the regenerator, adjacent to CHX and AC, guaranteeing uniform inflow and outflow. Therefore the governing equations are for laminar flow.

Applying asymptotic analysis, all variables are expanded in terms with the square of the Mach number as parameter, which is assumed to be very small [45]. The expansion takes the form

$$p(z, t) = p_0(z, t) + Ma^2 p_1(z, t) + o(Ma^4), \tag{3.2.16}$$

$$u(z, t) = u_0(z, t) + Ma^2 u_1(z, t) + o(Ma^4), \tag{3.2.17}$$

$$\rho_g(z, t) = \rho_{0_g}(z, t) + Ma^2 \rho_{1_g}(z, t) + o(Ma^4), \tag{3.2.18}$$

$$T_g(z, t) = T_{g_0}(z, t) + Ma^2 T_{g_1}(z, t) + o(Ma^4). \tag{3.2.19}$$

If we substitute these expansions into (3.2.12)-(3.2.15) we obtain the following *leading-order system*

$$\frac{\partial \rho_{g_0}}{\partial t} + \frac{\partial}{\partial z}(\rho_{g_0} u_0) = 0, \tag{3.2.20}$$

$$\frac{\partial p_0}{\partial z} = 0, \tag{3.2.21}$$

$$\rho_{g_0} c_p \left(\frac{\partial T_{g_0}}{\partial t} + u_0 \frac{\partial T_{g_0}}{\partial z} \right) = \frac{\mathcal{B}(\gamma - 1)}{\gamma} \frac{\partial p_0}{\partial t} + \frac{1}{Pe_g} \frac{\partial}{\partial z} \left(k_g \frac{\partial T_{g_0}}{\partial z} \right), \tag{3.2.22}$$

$$p_0 \mathcal{B} = \rho_{g_0} T_{g_0}. \tag{3.2.23}$$

The *first-order system*, not used herein, but given for completeness, reads

$$\frac{\partial \rho_{g_1}}{\partial t} + \frac{\partial}{\partial z}(\rho_{g_0} u_1) + \frac{\partial}{\partial z}(\rho_{g_1} u_0) = 0, \tag{3.2.24}$$

$$\rho_{g_0}(\frac{\partial u_0}{\partial t} + u_0 \frac{\partial u_0}{\partial z}) = -\frac{\partial p_1}{\partial z} + \frac{4}{3Re} \frac{\partial}{\partial z}(\mu \frac{\partial u_0}{\partial z}), \tag{3.2.25}$$

$$\rho_{g_0} c_p \left(\frac{\partial T_{g_1}}{\partial t} + u_0 \frac{\partial T_{g_1}}{\partial z} + u_1 \frac{\partial T_{g_0}}{\partial z} \right) + \rho_{g_1} \left(\frac{\partial T_{g_0}}{\partial t} + u_0 \frac{\partial T_{g_0}}{\partial z} \right) =$$
$$\frac{\mathcal{B}(\gamma - 1)}{\gamma} \left(\frac{\partial p_1}{\partial t} + u_0 \frac{\partial p_1}{\partial t} \right) + \frac{1}{Pe_g} \frac{\partial}{\partial z} \left(k_g \frac{\partial T_{g_1}}{\partial z} \right) + \frac{4}{3} \frac{\mathcal{B}(\gamma - 1)}{\gamma} \mu(\frac{\partial u_0}{\partial z})^2, \tag{3.2.26}$$

$$p_1 \mathcal{B} = \rho_{g_0} T_{g_1} + \rho_{g_1} T_{g_0}. \tag{3.2.27}$$

The dimensionless numbers C_{ff} and $\mathcal{A}$ for the PTRs are in the range of 2.1×10^{-4} to 2.6×10^{-3} and 1.5×10^{-4} to 1.8×10^{-3}, respectively. These values are approximations of the coefficients for friction force and heat transfer with the wall representing 2D corrections to 1D formulations. However, in the two-dimensional model the wall effects caused by friction and heat transfer are automatically included. Therefore, we ignore the small corrections in the 1D equations.

Equation (3.2.21) shows that the pressure is uniform in space. The pressure inside the tube, p_0, is only a function of time which is denoted by $P(t)$ from now on. The leading-order and the first-order terms in the pressure expansion are called the *thermodynamic pressure* and the *hydrodynamic pressure* respectively. The thermodynamic pressure is the global pressure driving the gas inside the pulse-tube. The acoustic pressure - which would be Ma $p_1(z,t)$ - does not play a role. The hydrodynamic pressure is a result of flow acceleration and viscosity.

Combining the equations (3.2.20) and (3.2.22) and omitting the subscripts '0', we obtain

$$\frac{\partial(\rho_g T_g)}{\partial t} + \frac{\partial(\rho_g u T_g)}{\partial z} = \frac{\mathcal{B}(\gamma-1)}{\gamma c_p} \frac{dP}{dt} + \frac{1}{c_p Pe_g} \frac{\partial}{\partial z}\left(k_g \frac{\partial T_g}{\partial z}\right). \tag{3.2.28}$$

Using the equation of state (3.2.23) we eliminate ρ_g to find

$$\mathcal{B}\frac{dP}{dt} + \mathcal{B}\frac{\partial(Pu)}{\partial z} = \frac{\mathcal{B}(\gamma-1)}{\gamma c_p} \frac{dP}{dt} + \frac{1}{c_p Pe_g} \frac{\partial}{\partial z}\left(k_g \frac{\partial T_g}{\partial z}\right). \tag{3.2.29}$$

If we assume that the heat capacity is constant, i.e. $\hat{c}_g = 1$, then rearranging the above equation gives the velocity gradient

$$\frac{\partial u}{\partial z} = -\frac{1}{\gamma P}\frac{dP}{dt} + \frac{1}{P\mathcal{B}Pe_g}\frac{\partial}{\partial z}\left(k_g \frac{\partial T_g}{\partial z}\right). \tag{3.2.30}$$

The energy equation (3.2.22) can be rewritten by eliminating the density via (3.2.23) and using $\hat{c}_g = 1$ as

$$\frac{\partial T_g}{\partial t} + u\frac{\partial T_g}{\partial z} = \frac{(\gamma-1)T_g}{\gamma P}\frac{dP}{dt} + \frac{T_g}{\mathcal{B}Pe_g P}\frac{\partial}{\partial z}\left(k_g \frac{\partial T_g}{\partial z}\right). \tag{3.2.31}$$

If we substitute the pressure time-derivative in equation (3.2.31) using equation (3.2.30) we get the following simplified equations

$$\frac{\partial u}{\partial z} = \frac{b_1}{P}\frac{\partial}{\partial z}(k_g \frac{\partial T_g}{\partial z}) - \frac{1}{\gamma P}\frac{dP}{dt}, \tag{3.2.32}$$

$$\frac{\partial T_g}{\partial t} = b_2\frac{T_g}{P}\frac{\partial}{\partial z}(k_g \frac{\partial T_g}{\partial z}) - u\frac{\partial T_g}{\partial z} + (1-\gamma)T_g\frac{\partial u}{\partial z}, \tag{3.2.33}$$

where

$$b_1 = \frac{1}{\mathcal{B}Pe_g}, \quad b_2 = \frac{\gamma}{\mathcal{B}Pe_g}. \tag{3.2.34}$$

The temperature equation (3.2.33) is a *convection-diffusion* equation with an additional nonlinear term. Note that the coefficients $b_{1,2} \ll 1$, so that equation (3.2.33) is dominated by convection. Equation (3.2.32) shows that the velocity gradient is practically proportional to the pressure time-derivative. Finally, the density is computed from equation (3.2.23) and $P(t)$ is a given function of time.

3.2.2 Regenerator

The equations for mass, momentum, energy transfer, together with the equation of state for an ideal gas, in the regenerator located at $0 \leq z \leq L_r$, where AC is at $z = 0$ and CHX at $z = L_r$ (see Figure 3.1), are

$$\frac{\partial(\rho_g \phi)}{\partial t} + \frac{\partial}{\partial z}(\rho_g \phi u) = 0 \quad , \tag{3.2.35}$$

$$\phi \rho_g \left(\frac{\partial u}{\partial t} + u \frac{\partial u}{\partial z} \right) = -\phi \frac{\partial p}{\partial z} + \frac{4}{3} \frac{\partial}{\partial z}(\phi \mu \frac{\partial u}{\partial z}) - \frac{\mu}{\kappa} u, \tag{3.2.36}$$

$$\rho_g c_p \phi \left(\frac{\partial T_g}{\partial t} + u \frac{\partial T_g}{\partial z} \right) = \beta(T_r - T_g) + \phi \left(\frac{\partial p}{\partial t} + u \frac{\partial p}{\partial z} \right) + \frac{\partial}{\partial z}(\phi k_g \frac{\partial T_g}{\partial z}) + \frac{4}{3} \phi \mu (\frac{\partial u}{\partial z})^2 \quad , \tag{3.2.37}$$

$$(1 - \phi)\rho_r c_r \frac{\partial T_r}{\partial t} = \beta(T_g - T_r) + \frac{\partial}{\partial z}\left((1 - \phi)k_r \frac{\partial T_r}{\partial z} \right) \quad , \tag{3.2.38}$$

$$p = \rho_g R_m T_g, \tag{3.2.39}$$

where T_r is the regenerator material temperature, T_g is the gas temperature, β is the heat transfer coefficient, c_r is the regenerator material heat capacity and ϕ is the *porosity*, which is the ratio of the void volume to the total volume of the porous medium. The equations (3.2.37) and (3.2.38) are the energy equations. *Darcy's law* has been included in the momentum equation (3.2.36) where κ is the *permeability*. In a homogeneous porous material the porosity, ϕ, permeability κ and material density ρ_r are constant. Non-dimensionalising the variables as we did for the gas inside the tube (3.2.11) and defining the following new scaling parameters

$$T_r = T_a \hat{T}_r, \quad k_r = \bar{k}_r \hat{k}_r, \quad c_r = \bar{c}_r \hat{c}_r, \tag{3.2.40}$$

the system of equations (3.2.35) - (3.2.39) becomes (omitting the hats)

$$\frac{\partial \rho_g}{\partial t} + \frac{\partial}{\partial z}(\rho_g u) = 0, \tag{3.2.41}$$

$$\frac{\partial p}{\partial z} = \frac{4 Ma^2}{3 Re} \frac{\partial}{\partial z}(\mu \frac{\partial u}{\partial z}) - Ma^2 \rho_g \left(\frac{\partial u}{\partial t} + u \frac{\partial u}{\partial z} \right) - \mathcal{D}\mu u, \tag{3.2.42}$$

$$c_p \rho_g \left(\frac{\partial T_g}{\partial t} + u \frac{\partial T_g}{\partial z} \right) = \beta_g^*(T_r - T_g) + \frac{\mathcal{B}(\gamma - 1)}{\gamma} \left(\frac{\partial p}{\partial t} + u \frac{\partial p}{\partial z} \right) + \frac{1}{Pe_g} \frac{\partial}{\partial z}(k_g \frac{\partial T_g}{\partial z})$$
$$+ \frac{4}{3} \frac{\mathcal{B}(\gamma - 1)}{\gamma} \frac{Ma^2}{Re} \mu (\frac{\partial u}{\partial z})^2, \tag{3.2.43}$$

$$c_r \frac{\partial T_r}{\partial t} = \beta_r^*(T_g - T_r) + \frac{1}{Pe_r} \frac{\partial}{\partial z}(k_r \frac{\partial T_r}{\partial z}), \tag{3.2.44}$$

$$p\mathcal{B} = \rho_g T_g, \tag{3.2.45}$$

where

$$\mathcal{D} = \frac{\bar{\mu}\bar{u}^2}{\phi p_{av} \omega k}, \quad \beta_g^* = \frac{\beta}{\bar{\rho}_g \bar{c}_g \phi \omega}, \quad \beta_r^* = \frac{\beta}{(1 - \phi)\rho_r \bar{c}_r \omega}, \quad \frac{\rho_r \bar{c}_r \bar{u}^2}{\bar{k}_r \omega}.$$

The values of the dimensionless numbers are listed in Table B.2 of Appendix B for the PTR studied herein. The values of Ma^2/Re and Ma^2 are about 10^{-9} and 10^{-6}, respec-

tively, so that we can neglect the first two terms of (3.2.42) and the last term of (3.2.43) on the right-hand sides. This leaves

$$\frac{\partial \rho_g}{\partial t} + \frac{\partial}{\partial z}(\rho_g u) = 0, \tag{3.2.46}$$

$$\frac{\partial p}{\partial z} = -\mathcal{D}\mu u. \tag{3.2.47}$$

$$c_p \rho_g \left(\frac{\partial T_g}{\partial t} + u \frac{\partial T_g}{\partial z} \right) = \beta_g^*(T_r - T_g) + \frac{\mathcal{B}(\gamma - 1)}{\gamma} \left(\frac{\partial p}{\partial t} + u \frac{\partial p}{\partial z} \right) + \frac{1}{Pe_g} \frac{\partial}{\partial z}(k_g \frac{\partial T_g}{\partial z}), \tag{3.2.48}$$

$$c_r \frac{\partial T_r}{\partial t} = \beta_r^*(T_g - T_r) + \frac{1}{Pe_r} \frac{\partial}{\partial z}(k_r \frac{\partial T_r}{\partial z}), \tag{3.2.49}$$

$$p\mathcal{B} = \rho_g T_g. \tag{3.2.50}$$

Combining the equations (3.2.46) and (3.2.48) and using ($\hat{c}_g = 1$) we obtain

$$\frac{\partial(\rho_g T_g)}{\partial t} + \frac{\partial(\rho_g u T_g)}{\partial z} = \mathcal{E}(T_r - T_g) + \frac{\mathcal{B}(\gamma - 1)}{\gamma} \left(\frac{\partial p}{\partial t} + u \frac{\partial p}{\partial z} \right) + \frac{1}{Pe_g} \frac{\partial}{\partial z} \left(k_g \frac{\partial T_g}{\partial z} \right). \tag{3.2.51}$$

Using equation (3.2.50) to eliminate ρ_g yields

$$\mathcal{B} \frac{\partial p}{\partial t} + \mathcal{B} \frac{\partial(pu)}{\partial z} = \beta_g^*(T_r - T_g) + \frac{\mathcal{B}(\gamma - 1)}{\gamma} \left(\frac{\partial p}{\partial t} + u \frac{\partial p}{\partial z} \right) + \frac{1}{Pe_g} \frac{\partial}{\partial z} \left(k_g \frac{\partial T_g}{\partial z} \right). \tag{3.2.52}$$

After rearranging the equation above we get the following velocity gradient equation

$$\frac{\partial u}{\partial z} = \frac{b_1}{p} \frac{\partial}{\partial z}(k_g \frac{\partial T_g}{\partial z}) + \frac{\beta_g^*}{\mathcal{B}p}(T_r - T_g) - \frac{1}{\gamma p}(\frac{\partial p}{\partial t} + u \frac{\partial p}{\partial z}). \tag{3.2.53}$$

Combining the equations (3.2.48) and (3.2.53) to eliminate the pressure time-derivative we obtain the following equation for the gas temperature

$$\frac{\partial T_g}{\partial t} = b_2 \frac{T_g}{p} \frac{\partial}{\partial z}(k_g \frac{\partial T_g}{\partial z}) + \frac{\gamma \beta_g^*}{\mathcal{B}} \frac{T_g}{p}(T_r - T_g) + (1 - \gamma)T_g \frac{\partial u}{\partial z} - u \frac{\partial T_g}{\partial z}. \tag{3.2.54}$$

We eliminate the time-derivative of the pressure in the evolution equation for the temperature and it only appears in the velocity gradient equation. The model governing the regenerator is the set of equations (3.2.47), (3.2.49), (3.2.53) and (3.2.54) for the four variables including u, p, T_g and T_r. The density follows from (3.2.50).

3.2.3   Boundary and initial conditions for tube and regenerator

To complete the system of equations (3.2.32), (3.2.33) for the tube, we need boundary and initial conditions.
From [16] we find that the volume flow in the orifice connecting tube and buffer in a linear approximation is given by (see Figure 3.1)

$$\dot{V}_H(t) = C_{or}\left(p_t(t) - p_b(t)\right), \tag{3.2.55}$$

This volume flow in the case of a double-inlet PTR is (see Figure 2.5)

$$\dot{V}_H(t) = C_{or_1}\left(p_t(t) - p_b(t)\right) - C_{or_{d1}}\left(p_c(t) - p_t(t)\right), \tag{3.2.56}$$

where $P_t(t)$ is the tube pressure which is identical to the pressure at the interface with the regenerator (tube pressure is uniform in space), $p_b(t)$ is the buffer pressure, $p_c(t)$ is the compressor pressure, C_{or} or C_{or_1} is the flow conductance of the main orifice and $C_{or_{d1}}$ is the double-inlet flow conductance. The flow velocity in the case of single-orifice PTR is then given by (see [16])

$$u(L_t, t) = u_H(t) = \frac{C_{or}}{A_t}\left(p_t(t) - p_b(t)\right), \tag{3.2.57}$$

and for the double-inlet PTR is

$$u(L_t, t) = u_H(t) = \frac{1}{A_t}\left[C_{or_1}\left(p_t(t) - p_b(t)\right) - C_{or_{d1}}\left(p_c(t) - p_t(t)\right)\right], \tag{3.2.58}$$

where u_H is the velocity at the hot end of the tube and A_t is the tube cross-sectional area. Let $\bar{p}_b$ be the average pressure in the buffer, then the *boundary condition for the velocity* in non-dimensional form for a single-orifice PTR reads (with hats omitted)

$$u_H(t) = \frac{C_{or}}{A_t}\frac{p_{av}}{\bar{u}}\left(p_t(t) - \frac{\bar{p}_b}{p_{av}}p_b(t)\right), \tag{3.2.59}$$

or

$$u_H(t) = \mathcal{C}(p_t(t) - \mathcal{E}_0 p_b(t)), \tag{3.2.60}$$

and for the double-inlet PTR is

$$u_H(t) = \frac{C_{or_1}}{A_t}\frac{p_{av}}{\bar{u}}\left(p_t(t) - \frac{\bar{p}_b}{p_{av}}p_b(t) - c_1\left(p_c(t) - p_t(t)\right)\right), \tag{3.2.61}$$

or

$$u_H(t) = \mathcal{C}\left[p_t(t) - \mathcal{E}_0 p_b(t) - c_1\left(p_c(t) - p_t(t)\right)\right], \tag{3.2.62}$$

where

$$\mathcal{C} = \frac{C_{or_1}}{A_t}\frac{p_{av}}{\bar{u}}, \quad \mathcal{E}_0 = \frac{\bar{p}_b}{p_{av}}, \quad c_1 = \frac{C_{or_1}}{C_{or_{d1}}}. \tag{3.2.63}$$

The pressure in the buffer, $p_b(t)$, is a time-dependent function that makes the cycle-averaged mass flow through the hot end becomes automatically zero. The volume flow through the orifice causes adiabatic compression and expansion in the buffer according to the thermodynamic Poisson law which reads

$$\dot{V}_H(t) = \frac{c_v}{c_p}\frac{V_b}{p_b(t)}\frac{dp_b(t)}{dt}, \tag{3.2.64}$$

where V_b is the buffer volume. Combining the equations (3.2.55) and (3.2.64) we obtain an ODE for the buffer pressure

$$\frac{dp_b(t)}{dt} = \frac{c_p C_{or}}{c_v V_b}p_b(t)(p_t(t) - p_b(t)). \tag{3.2.65}$$

If we make this equation non-dimensional it reads (omitting the hats)

$$\frac{dp_b(t)}{dt} = \mathcal{K}p_b(t)(p_t(t) - \mathcal{E}p_b(t)), \tag{3.2.66}$$

where

$$\mathcal{K} = \frac{c_p C_{or} p_{av}}{c_v V_b \omega}. \tag{3.2.67}$$

This dimensionless ODE can be solved numerically there by taking the initial condition as $\hat{p}_b(0) = 1$.

The upwind *boundary conditions for the temperature* equation (3.2.33) ignore the local conduction and the corresponding boundary layer and read in dimensionless form

$$\begin{cases} T_g(0,t) = T_C & \text{if} \quad u(0,t) \geq 0, \\ \frac{\partial T_g}{\partial z}(0,t) = \left((1-\gamma)T_g(0,t)\frac{\partial u}{\partial z}(0,t) - \frac{\partial T_g}{\partial t}(0,t)\right)/u(0,t) & \text{if} \quad u(0,t) < 0. \end{cases} \tag{3.2.68}$$

$$\begin{cases} T_g(L,t) = T_H & \text{if} \quad u(L,t) \leq 0, \\ \frac{\partial T_g}{\partial z}(L,t) = \left((1-\gamma)T_g(0,t)\frac{\partial u}{\partial z}(0,t) - \frac{\partial T_g}{\partial t}(L,t)\right)/u(L,t) & \text{if} \quad u(L,t) > 0. \end{cases} \tag{3.2.69}$$

The hot-end boundary condition (3.2.69) shows that when the gas flows towards the HHX, a Neumann boundary condition derived from the energy equation (3.2.33), without the conduction term is applied. Otherwise, when the gas flows from the buffer through the orifice and HHX into the tube, it takes the same temperature as the HHX (ideal heat exchanger).

Any temperature distribution connecting the CHX and HHX can be the initial condition for the gas temperature inside the tube. However, it will be shown in Chapter 5 that the initial condition should be chosen in a smart way such that a net flow (DC flow) is not created in the simulation. The initial condition for the velocity inside the tube is determined by $P(0)$ and the *initial temperature* through (3.2.32) thereby ignoring the conductivity term. For a linear temperature distribution it is

$$u(x,0) = -\left(\frac{1}{\gamma P(0)}\frac{\partial P}{\partial t}(0)\right)z. \tag{3.2.70}$$

To complete the system of equations (3.2.47), (3.2.49), (3.2.53) and (3.2.54) for the regenerator, we need boundary and initial conditions. See Figure 3.1. In particular we prescribe the pressure, $p_c(t)$, at the compressor side as the boundary condition for (3.2.47). All variations in pressure and temperature are neglected at the interface/junction. This means the uniform pressure in the tube is

$$P(t) = p(L_r, t). \tag{3.2.71}$$

The boundary condition for the velocity at the interface with the tube $u_C(t)$ for (3.2.53) in the case of a single-stage PTR is derived from the mass conservation relation

$$\dot{m}_r = \dot{m}_t \tag{3.2.72}$$

where $\dot{m}$ is the mass flow rate. The velocity in the regenerator at CHX (which is in fact a small distance from it, after straightener, inside the regenerator), using $\dot{m} = \rho u A$ and pressure continuity $p_t = p_r$ and (3.2.50), is

$$u_r(t, L_r) = \frac{u_t(t, 0) A_t}{A_r \phi} \frac{T_g(t, L_r)}{T_t(t, 0)}. \tag{3.2.73}$$

where A is the cross-section. The tube velocity $u_t(t, 0)$ at the interface in 1D is the velocity immediately after the thermal boundary layer existing at the CHX when the flow is towards it. For the regenerator material temperature (3.2.49) we can simply define two Dirichlet boundary conditions as

$$\begin{cases} T_r(0, t) = T_H, \\ T_r(L_r, t) = T_C. \end{cases} \tag{3.2.74}$$

For the gas temperature equation (3.2.54) we introduce two boundary conditions similar to the tube's as follows

$$\begin{cases} T_g(0, t) = T_H \quad \text{if} \quad u(0, t) \geq 0, \\[6pt] \dfrac{\partial T_g}{\partial z}(0, t) = [-\dfrac{\partial T_g}{\partial t}(0, t) + \dfrac{\gamma \beta_g^*}{\mathcal{B}} \dfrac{T_g(0, t)}{p_c(t)}(T_H - T_g(0, t)) + \\[6pt] (1 - \gamma) T_g(0, t) \dfrac{\partial u}{\partial z}(0, t)] / u(0, t) \quad \text{if} \quad u(0, t) < 0. \end{cases} \tag{3.2.75}$$

$$\begin{cases} T_g(L_r, t) = T_C \quad \text{if} \quad u(L_r, t) \leq 0, \\[6pt] \dfrac{\partial T_g}{\partial z}(L_r, t) = [-\dfrac{\partial T_g}{\partial t}(L_r, t) + \dfrac{\gamma \beta_g^*}{\mathcal{B}} \dfrac{T_g(L_r, t)}{p(L_r, t)}(T_C - T_g(L_r, t)) + \\[6pt] (1 - \gamma) T_g(L_r, t) \dfrac{\partial u}{\partial z}(L_r, t)] / u(L_r, t) \quad \text{if} \quad u(L_r, t) > 0. \end{cases} \tag{3.2.76}$$

Finally, since the heat capacity of the regenerator material is high, the temperature of the gas and the solid material will not change too much during the oscillation of the gas. Therefore we simply define the same linear functions as the initial conditions for the gas and regenerator material temperature connecting the cold and the hot ends of the regenerator, where the cold end temperature should be approximately close to estimated equilibrium temperature at CHX.

3.3 Two-dimensional model of the tube

An axisymmetrical two-dimensional formulation is given so that more accurate numerical studies of the PTR, including the wall effects due to friction and heat transfer, can
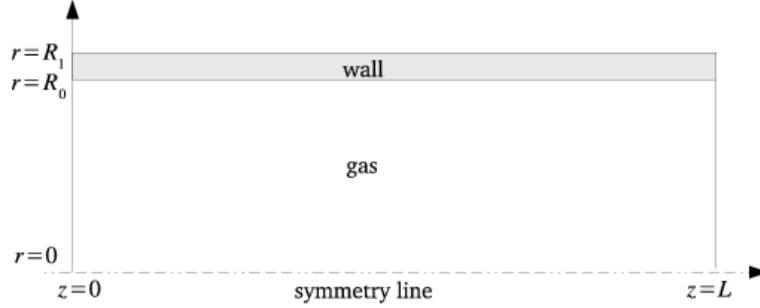
Figure 3.3: Axisymmetrical domain for the pulse-tube including wall.

be performed.

3.3.1 Tube

We consider an axisymmetrical domain including the gas and the wall surrounding the cylinder as sketched in Fig. 3.3. The conservation laws and the equation of state for an ideal gas in cylindrical coordinates are

$$\frac{\partial \rho}{\partial t} + \frac{\partial}{\partial z}(\rho u) + \frac{1}{r}\frac{\partial}{\partial r}(r\rho v) = 0, \tag{3.3.1}$$

$$\rho\left(\frac{\partial u}{\partial t} + u\frac{\partial u}{\partial z} + v\frac{\partial u}{\partial r}\right) = -\frac{\partial p}{\partial z} - \left[\frac{1}{r}\frac{\partial}{\partial r}(r\tau_{rz}) + \frac{\partial \tau_{zz}}{\partial z}\right], \tag{3.3.2}$$

$$\rho\left(\frac{\partial v}{\partial t} + u\frac{\partial v}{\partial z} + v\frac{\partial v}{\partial r}\right) = -\frac{\partial p}{\partial r} - \left[\frac{1}{r}\frac{\partial}{\partial r}(r\tau_{rr}) + \frac{\partial \tau_{rz}}{\partial z}\right], \tag{3.3.3}$$

$$\rho c_g\left(\frac{\partial T}{\partial t} + u\frac{\partial T}{\partial z} + v\frac{\partial T}{\partial r}\right) = \frac{\partial p}{\partial t} + u\frac{\partial p}{\partial z} + v\frac{\partial p}{\partial r} + \frac{1}{r}\frac{\partial}{\partial r}\left(rk_g\frac{\partial T}{\partial r}\right) + \frac{\partial}{\partial z}\left(k_g\frac{\partial T}{\partial z}\right) + \Phi, \tag{3.3.4}$$

$$p = \rho R_m T, \tag{3.3.5}$$

where the axial coordinate is z, the radial coordinate is r, and u, v are the horizontal and radial velocities, respectively, τ is the stress tensor and Φ is the viscous dissipation function. The components of the viscous stress tensor (τ) are

$$\tau_{zz} = -2\mu\frac{\partial u}{\partial z} + \frac{2}{3}\mu(\nabla \cdot \mathbf{u}) = -\mu\left[\frac{4}{3}\frac{\partial u}{\partial z} - \frac{2}{3}\frac{v}{r} - \frac{2}{3}\frac{\partial v}{\partial r}\right], \tag{3.3.6}$$

$$\tau_{rr} = -2\mu\frac{\partial v}{\partial r} + \frac{2}{3}\mu(\nabla \cdot \mathbf{u}) = -\mu\left[\frac{4}{3}\frac{\partial v}{\partial r} - \frac{2}{3}\frac{v}{r} - \frac{2}{3}\frac{\partial u}{\partial z}\right], \tag{3.3.7}$$

$$\tau_{rz} = -\mu \left(\frac{\partial u}{\partial r} + \frac{\partial v}{\partial z} \right), \tag{3.3.8}$$

where **u** is the velocity vector (u, v). The viscous dissipation function Φ in the energy equation (3.3.4) is derived from (3.1.8) as

$$\Phi = \tau_{ij} \frac{\partial u_i}{\partial x_j} = \tau_{zz} \frac{\partial u}{\partial z} + \tau_{rr} \frac{\partial v}{\partial r} + \tau_{rz} \left(\frac{\partial u}{\partial r} + \frac{\partial v}{\partial z} \right), \tag{3.3.9}$$

which is a positive quantity. The system of equations is made non-dimensional using

$$\rho = \bar{\rho}\hat{\rho}, \ T = T_a \hat{T}, \ p = p_{av}\hat{p}, \ t = \hat{t}/\omega, \ k_g = \bar{k}_g \hat{k}_g, \ \mu = \bar{\mu}\hat{\mu}, \ c_g = \bar{c}_g \hat{c}_g$$

$$u = \bar{u}\hat{u}, \ v = \bar{u}\hat{v}, \ z = (\bar{u}/\omega)\hat{z}, \ r = (\bar{u}/\omega)\hat{r}. \tag{3.3.10}$$

After non-dimensionalisation and substituting the stress tensors (3.3.6)-(3.3.9), the governing equations (3.3.1) - (3.3.5) become (omitting the hats)

$$\frac{\partial \rho}{\partial t} + \frac{\partial}{\partial z}(\rho u) + \frac{1}{r} \frac{\partial}{\partial r}(r\rho v) = 0, \tag{3.3.11}$$

$$\rho \left(\frac{\partial u}{\partial t} + u\frac{\partial u}{\partial z} + v\frac{\partial u}{\partial r} \right) = -\frac{1}{Ma^2}\frac{\partial p}{\partial z} + \frac{1}{Re}\left[\frac{1}{r}\frac{\partial}{\partial r}\left(r\mu(\frac{\partial u}{\partial r}) \right) + \frac{4}{3}\frac{\partial}{\partial z}\left(\mu\frac{\partial u}{\partial z} \right) \right]$$

$$+ \frac{1}{Re}\left[\frac{1}{r}\frac{\partial}{\partial r}\left(r\mu(\frac{\partial v}{\partial z}) \right) - \frac{2}{3}\frac{\partial}{\partial z}\left(\mu(\frac{v}{r} + \frac{\partial v}{\partial r}) \right) \right], \tag{3.3.12}$$

$$\rho \left(\frac{\partial v}{\partial t} + u\frac{\partial v}{\partial z} + v\frac{\partial v}{\partial r} \right) = -\frac{1}{Ma^2}\frac{\partial p}{\partial r}$$

$$+ \frac{1}{Re}\left[\frac{4}{3}\frac{\partial}{\partial r}\left(\mu(\frac{\partial v}{\partial r}) \right) + \frac{4}{3}\frac{\mu}{r}\left(\frac{\partial v}{\partial r} \right) - \frac{2}{3}\frac{\partial}{\partial r}\left(\mu\frac{v}{r} \right) - \frac{2}{3}\frac{\mu v}{r^2} + \frac{\partial}{\partial z}\left(\mu\frac{\partial v}{\partial z} \right) \right] \tag{3.3.13}$$

$$+ \frac{1}{Re}\left[-\frac{2}{3}\frac{\mu}{r}\left(\frac{\partial u}{\partial z} \right) - \frac{2}{3}\frac{\partial}{\partial r}\left(\mu\frac{\partial u}{\partial z} \right) + \frac{\partial}{\partial z}\left(\mu\frac{\partial u}{\partial r} \right) \right],$$

$$\rho \left(\frac{\partial T}{\partial t} + u\frac{\partial T}{\partial z} + v\frac{\partial T}{\partial r} \right) = \frac{\mathcal{B}(\gamma-1)}{\gamma} \left(\frac{\partial p}{\partial t} + u\frac{\partial p}{\partial z} + v\frac{\partial p}{\partial r} \right) + \frac{1}{Pe_g}\frac{1}{r}\frac{\partial}{\partial r}\left(rk_g\frac{\partial T}{\partial r} \right) +$$

$$\frac{1}{Pe_g}\frac{\partial}{\partial z}\left(k_g\frac{\partial T}{\partial z} \right) + \frac{\gamma-1}{\gamma}\mathcal{B}\frac{Ma^2}{Re}\Phi, \tag{3.3.14}$$

$$p\mathcal{B} = \rho T. \tag{3.3.15}$$

We employ an asymptotic analysis like in the one-dimensional case in Section 3.2.1 assuming the expansion

$$f(z, r, t) = f_0(z, r, t) + Ma^2 f_1(z, r, t) + o(Ma^4),$$

for all variables including pressure p, axial velocity u, radial velocity v, gas temperature T and density ρ. This low Mach-number approximation transforms the system of equations (3.3.11)-(3.3.15) into the following leading-order system

$$\frac{\partial \rho_0}{\partial t} + \frac{\partial}{\partial z}(\rho_0 u_0) + \frac{1}{r} \frac{\partial}{\partial r}(r\rho_0 v_0) = 0, \tag{3.3.16}$$

$$\frac{\partial p_0}{\partial z} = 0, \tag{3.3.17}$$

$$\frac{\partial p_0}{\partial r} = 0, \tag{3.3.18}$$

$$\rho_0 \left(\frac{\partial T_0}{\partial t} + u_0 \frac{\partial T_0}{\partial z} + v_0 \frac{\partial T_0}{\partial r} \right) = \frac{\mathcal{B}(\gamma - 1)}{\gamma} \frac{dp_0}{dt} + \frac{1}{Pe_g} \left[\frac{1}{r} \frac{\partial}{\partial r} \left(r k_g \frac{\partial T_0}{\partial r} \right) + \frac{\partial}{\partial z} \left(k_g \frac{\partial T_0}{\partial z} \right) \right], \tag{3.3.19}$$

$$p_0 \mathcal{B} = \rho_0 T_0. \tag{3.3.20}$$

The momentum equations (3.3.17), (3.3.18) reveal a spatially uniform leading-order pressure. This is the thermodynamic pressure denoted by $P(t)$. The system (3.3.16)-(3.3.20) is not sufficient for describing a two-dimensional velocity field. For example, if the flow is isothermal, T_0, p_0 and ρ_0 are constant, and the remaining equation (3.3.16) is not sufficient to determine the flow velocities u_0 and v_0. To overcome this problem the following first-order momentum equations are taken instead,

$$\rho_0 \left(\frac{\partial u_0}{\partial t} + u_0 \frac{\partial u_0}{\partial z} + v_0 \frac{\partial u_0}{\partial r} \right) = -\frac{\partial p_1}{\partial z} + \frac{1}{Re} \left[\frac{1}{r} \frac{\partial}{\partial r} \left(r \mu (\frac{\partial u_0}{\partial r}) \right) + \frac{4}{3} \frac{\partial}{\partial z} \left(\mu \frac{\partial u_0}{\partial z} \right) \right]$$
$$+ \frac{1}{Re} \left[\frac{1}{r} \frac{\partial}{\partial r} \left(r \mu (\frac{\partial v_0}{\partial z}) \right) - \frac{2}{3} \frac{\partial}{\partial z} \left(\mu (\frac{v_0}{r} + \frac{\partial v_0}{\partial r}) \right) \right], \tag{3.3.21}$$

$$\rho_0 \left(\frac{\partial v_0}{\partial t} + u_0 \frac{\partial v_0}{\partial z} + v_0 \frac{\partial v_0}{\partial r} \right) = -\frac{\partial p_1}{\partial r}$$
$$+ \frac{1}{Re} \left[\frac{4}{3} \frac{\partial}{\partial r} \left(\mu (\frac{\partial v_0}{\partial r}) \right) + \frac{4}{3} \frac{\mu}{r} \left(\frac{\partial v_0}{\partial r} \right) - \frac{2}{3} \frac{\partial}{\partial r} \left(\mu \frac{v_0}{r} \right) - \frac{2}{3} \frac{\mu v_0}{r^2} + \frac{\partial}{\partial z} \left(\mu \frac{\partial v_0}{\partial z} \right) \right] \tag{3.3.22}$$
$$+ \frac{1}{Re} \left[-\frac{2}{3} \frac{\mu}{r} \left(\frac{\partial u_0}{\partial z} \right) - \frac{2}{3} \frac{\partial}{\partial r} \left(\mu \frac{\partial u_0}{\partial z} \right) + \frac{\partial}{\partial z} \left(\mu \frac{\partial u_0}{\partial r} \right) \right],$$

where p_1 is the first-order pressure. From here on we call the leading-order pressure "thermodynamic", i.e. $P_0 = P(t)$, and the first-order pressure "hydrodynamic", i.e. $p_1 = p(z, r, t)$. A velocity divergence constraint is derived by first combining the continuity equation (3.3.16) and the energy equation (3.3.19). Omitting the subscripts, the combination reads as follows

$$\frac{\partial (\rho T)}{\partial t} + \frac{\partial (\rho T u)}{\partial z} + \frac{\partial (\rho T v)}{\partial r} + \rho T \frac{v}{r} = \frac{\mathcal{B}(\gamma - 1)}{\gamma} \frac{dP}{dt} + \frac{1}{Pe_g} \left[\frac{1}{r} \frac{\partial}{\partial r} \left(r k_g \frac{\partial T}{\partial r} \right) + \frac{\partial}{\partial z} \left(k_g \frac{\partial T}{\partial z} \right) \right]. \tag{3.3.23}$$

Substituting the equation of state (3.3.20) gives

$$\mathcal{B} \frac{dP}{dt} + P\mathcal{B} \left(\frac{\partial u}{\partial z} + \frac{\partial v}{\partial r} + \frac{v}{r} \right) = \frac{\mathcal{B}(\gamma - 1)}{\gamma} \frac{dP}{dt} \tag{3.3.24}$$
$$+ \frac{1}{Pe_g} \left[\frac{1}{r} \frac{\partial}{\partial r} \left(r k_g \frac{\partial T}{\partial r} \right) + \frac{\partial}{\partial z} \left(k_g \frac{\partial T}{\partial z} \right) \right],$$

which simplifies to

$$\frac{\partial u}{\partial z} + \frac{\partial v}{\partial r} + \frac{v}{r} = -\frac{1}{\gamma P(t)} \frac{dP}{dt} + \frac{1}{Pe_g} \frac{1}{\mathcal{B}P} \left[\frac{1}{r} \frac{\partial}{\partial r} \left(r k_g \frac{\partial T}{\partial r} \right) + \frac{\partial}{\partial z} \left(k_g \frac{\partial T}{\partial z} \right) \right]. \tag{3.3.25}$$

An evolution equation for the temperature is derived by substituting the density from equation (3.3.20) into the energy equation (3.3.19)

$$\frac{\partial T}{\partial t} + u\frac{\partial T}{\partial z} + v\frac{\partial T}{\partial r} = \frac{T}{\mathcal{B}PPe_g}\left[\frac{1}{r}\frac{\partial}{\partial r}\left(rk_g\frac{\partial T}{\partial r}\right) + \frac{\partial}{\partial z}\left(k_g\frac{\partial T}{\partial z}\right)\right] + \frac{\gamma-1}{\gamma}\frac{T}{P}\frac{dP}{dt}. \quad (3.3.26)$$

Finally we are left with four equations (3.3.21), (3.3.22), (3.3.25), (3.3.26) and four unknowns u, v, T, p.

3.3.2 Tube wall

The wall effect consisting of the skin friction force and the fluid-solid heat exchange is taken into account automatically in the two-dimensional analysis. The friction force is represented by the viscous stress tensor component τ_{rz} in the momentum equations. Assuming continuity of temperature and heat flux at the interface between the gas and the wall is close to the physical reality. The heat flux at the outer boundary of the tube is assumed to be zero, because there is a vacuum chamber surrounding the whole system and radiation is disregarded herein. Energy conservation for the wall is governed by (assuming constant wall thermal conductivity)

$$\rho_w c_w \frac{\partial T_w}{\partial t} = k_w\left(\frac{\partial^2 T_w}{\partial r^2} + \frac{1}{r}\frac{\partial T_w}{\partial r} + \frac{\partial^2 T_w}{\partial z^2}\right), \quad (3.3.27)$$

where T_w, ρ_w, c_w and k_w are temperature, density, heat capacity and thermal conductivity of the solid wall material. We non-dimensionalise equation (3.3.27) with the same quantities as defined for the gas (3.2.11), which gives (omitting hats)

$$\frac{\partial T_w}{\partial t} = Fo\left(\frac{\partial^2 T_w}{\partial r^2} + \frac{1}{r}\frac{\partial T_w}{\partial r} + \frac{\partial^2 T_w}{\partial z^2}\right), \quad (3.3.28)$$

with

$$Fo = \frac{\bar{k}_w \omega}{\bar{\rho}_w \bar{c}_w \bar{u}^2}. \quad (3.3.29)$$

Here Fo is the dimensionless *thermal diffusivity* coefficient called *Fourier number*.

3.3.3 Boundary and initial conditions

The physical boundary conditions for the hydrodynamic pressure (p), horizontal velocity (u), radial velocity (v), gas temperature (T) and wall temperature (T_w) are shown in Table 3.1. The boundary conditions for the temperature equation (3.3.26) at the hot and cold ends are similar to those in the one-dimensional case (3.2.68)-(3.2.69)

$$\begin{cases} T(L, r, t) = T_H \;\; \text{if} \;\; u(L, r, t) \leq 0 \\ \\ \frac{\partial T}{\partial z}(L, r, t) = f_1(r, t) \;\; \text{if} \;\; u(L, r, t) > 0 \end{cases}, \quad (3.3.30)$$

Position	$u(z,r,t)$	$v(z,r,t)$	$p(z,r,t)$	$T(z,r,t)$	$T_w(z,r,t)$
hot end $(z = L_t)$	$u = u_H$	$v = 0$		$\begin{cases} T = T_H, \ u \leq 0 \\ \dfrac{\partial T}{\partial z} = f_1(r,t), \ u > 0 \end{cases}$	$T_w = T_H$
cold end $(z = 0)$		$v = 0$	$p = 0$	$\begin{cases} T = T_c, \ u \geq 0 \\ \dfrac{\partial T}{\partial z} = f_2(r,t), \ u < 0 \end{cases}$	$T_w = T_c$
center line $(r = 0)$	$\dfrac{\partial u}{\partial r} = 0$	$v = 0$		$\dfrac{\partial T}{\partial r} = 0$	
interface $(r = r_0)$	$u = 0$	$v = 0$	$\dfrac{\partial T}{\partial r} = 0$	$T = T_w$	$\dfrac{\partial T}{\partial r} = \beta_w \dfrac{\partial T_w}{\partial r}$
outer wall $(r = r_1)$					$\dfrac{\partial T_w}{\partial r} = 0$

Table 3.1: Boundary conditions for the two-dimensional tube.

$$f_1(r,t) = \left(\frac{\gamma - 1}{\gamma P(t)} \frac{dP}{dt}(t) T(L,r,t) - \frac{\partial T}{\partial t}(L,r,t) \right) / u(L,r,t), \qquad (3.3.31)$$

$$\begin{cases} T(0,r,t) = T_C \ \text{ if } \ u(0,r,t) \geq 0 \\[2mm] \dfrac{\partial T}{\partial z}(0,r,t) = f_2(r,t) \ \text{ if } \ u(0,r,t) < 0 \end{cases}, \qquad (3.3.32)$$

$$f_2(r,t) = \left(\frac{\gamma - 1}{\gamma P(t)} \frac{dP}{dt}(t) T(0,r,t) - \frac{\partial T}{\partial t}(0,r,t) \right) / u(0,r,t). \qquad (3.3.33)$$

In 2D the cross-sectional averaging velocity after the boundary layer by the CHX in the tube is

$$u_t(t,0) = \bar{u}_t(t,0) = \frac{1}{A_t} \int_0^{r0} u_t \, dA_t. \qquad (3.3.34)$$

which is used for coupling of the 1D regenerator and 2D tube interface condition. The heat flux continuity gives a coupling between the gas and wall temperatures at the interface through

$$\frac{\partial T}{\partial r} = \beta_w \frac{\partial T_w}{\partial r} \text{ where } \beta_w = \frac{k_w}{k_g}. \qquad (3.3.35)$$

1D results for the axial velocity and the temperature can be defined as good initial conditions in 2D. No-flow steady state can be a good initial guess for the radial velocity.

3.4 One-dimensional model with non-ideal gas

The enthalpy of a real gas is not only a function of temperature, but also of pressure. Here we show the final equations governing the system including the tube and the regenerator, where the equation of state for the gas is different from the ideal case.

3.4.1 Tube

To derive the equations governing the tube with non-ideal gas we make the following steps. The one-dimensional equations for mass, momentum, energy transfer and the equation of state in the tube part ($0 < x < L_t$) are

$$\frac{\partial \rho_g}{\partial t} + \frac{\partial}{\partial x}(\rho_g u) = 0, \tag{3.4.1}$$

$$\frac{\partial p}{\partial x} = 0, \tag{3.4.2}$$

$$\rho_g \frac{Dh}{Dt} = \frac{Dp}{Dt} + \frac{\partial}{\partial x}(k_g \frac{\partial T_g}{\partial x}), \tag{3.4.3}$$

$$(p + \frac{a}{V_m^2})(V_m - b) = RT_g, \tag{3.4.4}$$

where x is the axial coordinate and small terms have been neglected. (see Section 3.2.1). Here h is the enthalpy of the gas defined by (3.1.9) and V_m is the molar volume. The equation of state (3.4.4) is the Van der Waals equation. The pressure is uniform in space. It is the thermodynamic pressure P which is only a function of time. A symbolic expression for the second term in the real gas enthalpy H_p defined by (3.1.10), follows from the equation of state (3.4.4) which is rewritten as

$$RT_g = PV_m + \frac{a}{V_m} - \frac{ab}{V_m^2} - bP.$$

Taking the molar-volume derivative at constant pressure gives

$$R\left(\frac{\partial T_g}{\partial V_m}\right)_p = P - \frac{a}{V_m^2} + 2\frac{ab}{V_m^3},$$

so that

$$\begin{aligned} H_p &= V_m - T_g\left(\frac{\partial V_m}{\partial T_g}\right) = V_m - \frac{RT_g}{R\left(\frac{\partial T_g}{\partial V_m}\right)_p}, \\ &= V_m - \frac{PV_m + \frac{a}{V_m} - \frac{ab}{V_m^2} - bP}{P - \frac{a}{V_m^2} + 2\frac{ab}{V_m^3}}, \\ &= \frac{bPV_m^3 - 2aV_m^2 + 3abV_m}{PV_m^3 - aV_m + 2ab}. \end{aligned} \tag{3.4.5}$$

In the high-temperature limit, i.e. $T_g \to \infty$ at constant pressure, we see that $V_m \to \infty$ and $H_p \to b$. Substituting

$$V_m = M/\rho_g, \tag{3.4.6}$$

in (3.4.5) we obtain

$$H_p = \frac{bPM^3 - 2aM^2\rho_g + 3abM\rho_g^2}{PM^2 - aM\rho_g^2 + 2ab\rho_g^3}. \tag{3.4.7}$$

This is then used in (3.1.9) to calculate the enthalpy. It is necessary to mention that H_p derived from Van der Waals formula is a quite good approximation of the experimental results for temperatures higher than 10 K, but not for temperatures less than 10 K.
We simplify the energy equation for the gas inside the tube (3.4.3) using the enthalpy relation (3.1.9) as follows

$$\rho_g c_p \frac{DT_g}{Dt} = (1 - \frac{\rho_g H_p}{M})\frac{DP}{Dt} + \frac{\partial}{\partial x}(k_g \frac{\partial T_g}{\partial x}). \tag{3.4.8}$$

The equation of state (3.4.4) in terms of density using (3.4.6) reads

$$(P + \frac{a}{M^2}\rho_g^2)(\frac{M}{\rho_g} - b) = RT_g.$$

After rearrangement, the pressure satisfies

$$P = \frac{R_m \rho_g T_g}{1 - b_m \rho_g} - a_m \rho_g^2, \tag{3.4.9}$$

where $R_m = R/M$ is the specific gas constant, $a_m = a/M^2$ and $b_m = b/M$.

By using already defined dimensionless variables, the equations (3.4.1), (3.4.8) and (3.4.9) now turn into dimensionless form as follows

$$\bar{\rho}\frac{\partial \hat{\rho}_g}{\partial \hat{t}} + \bar{\rho}\frac{\partial}{\partial \hat{x}}(\hat{\rho}_g \hat{u}) = 0, \tag{3.4.10}$$

$$\bar{\rho}_g \bar{c}_p T_a \omega \hat{\rho}_g \hat{c}_p \frac{D\hat{T}_g}{D\hat{t}} = p_{av}\omega(1 - \frac{\hat{\rho}_g \hat{H}_p}{M})\frac{D\hat{P}}{D\hat{t}} + \bar{k}_g T_a \frac{\omega^2}{\bar{u}^2}\frac{\partial}{\partial \hat{x}}(\hat{k}_g \frac{\partial \hat{T}_g}{\partial \hat{x}}), \tag{3.4.11}$$

$$p_{av}\hat{P} = R_m \bar{\rho}_g T_a \frac{\hat{\rho}_g \hat{T}}{1 - b_m \bar{\rho}_g \hat{\rho}_g} - a_m \bar{\rho}_g^2 \hat{\rho}_g^2. \tag{3.4.12}$$

Dropping the hats we obtain

$$\frac{D\rho_g}{Dt} = -\rho_g \frac{\partial u}{\partial x}, \tag{3.4.13}$$

$$\rho_g c_p \frac{DT_g}{Dt} = \frac{\mathcal{B}(\gamma - 1)}{\gamma}(1 - \rho_g H_p)\frac{DP}{Dt} + \frac{1}{Pe_g}\frac{\partial}{\partial x}(k_g \frac{\partial T_g}{\partial x}), \tag{3.4.14}$$

$$P = \frac{\rho_g T_g}{\mathcal{B}(1 - \mathcal{N}\rho_g)} - \mathcal{M}\rho_g^2, \tag{3.4.15}$$

where

$$\mathcal{M} = a_m \bar{\rho}^2/p_{av}, \quad \mathcal{N} = b_m \bar{\rho}. \tag{3.4.16}$$

Where (3.4.13), (3.4.14) are PDEs, the relation (3.4.15) is algebraic. In order to derive a differential equation for the velocity we proceed as follows.
If we take the material derivative of both sides of the equation of state (3.4.15) we get

$$\frac{DP}{Dt} = \frac{1}{\mathcal{B}(1-N\rho_g)^2}[(1-N\rho_g)(T_g\frac{D\rho_g}{Dt} + \rho_g\frac{DT_g}{Dt}) + N\rho_g T_g\frac{D\rho_g}{Dt}] - 2\mathcal{M}\rho_g\frac{D\rho_g}{Dt},$$

and after reordering

$$\frac{DP}{Dt} = [\frac{T_g}{\mathcal{B}(1-N\rho_g)^2} - 2\mathcal{M}\rho_g]\frac{D\rho_g}{Dt} + \frac{\rho_g}{\mathcal{B}(1-N\rho_g)}\frac{DT_g}{Dt}. \qquad (3.4.17)$$

If we substitute the material derivative of the density and the gas temperature by equations (3.4.13) and (3.4.14) respectively into (3.4.17) and reorder it, we obtain velocity gradient

$$\begin{aligned}\frac{\partial u}{\partial z} &= \frac{1}{(\frac{T_g}{B(1-\mathcal{N}\rho_g)^2} - 2\mathcal{M}\rho_g)\mathcal{B}c_p\rho_g(1-\mathcal{N}\rho_g)}\left(\frac{1}{Pe_g}\frac{\partial}{\partial z}(k_g\frac{\partial T_g}{\partial z})\right) \\ &\quad -\frac{1}{\rho_g(\frac{T_g}{B(1-\mathcal{N}\rho_g)^2} - 2\mathcal{M}\rho_g)}\left(1 - \frac{(\gamma-1)(1-\rho_g H_p)}{\gamma c_p(1-\mathcal{N}\rho_g)}\right)\frac{DP}{Dt}.\end{aligned} \qquad (3.4.18)$$

This is an equation for the velocity gradient in the tube. If we substitute the pressure material derivative from (3.4.17) into the energy equation (3.4.14) we get the following evolution equation for the gas temperature which is excluded the pressure material derivative.

$$\begin{aligned}\frac{DT_g}{Dt} &= \frac{1}{\rho_g}\left[\frac{\gamma(1-\mathcal{N}\rho_g)}{\gamma c_p(1-\mathcal{N}\rho_g) - (\gamma-1)(1-\rho_g H_p)}\right]\left(\frac{1}{Pe_g}\frac{\partial}{\partial x}(k_g\frac{\partial T_g}{\partial x})\right) \\ &\quad -\left(\frac{(\gamma-1)(1-\rho_g H_p)[T_g - 2\mathcal{M}\mathcal{B}\rho_g(1-\mathcal{N}\rho_g)^2]}{(1-\mathcal{N}\rho_g)[\gamma c_p(1-\mathcal{N}\rho_g) - (\gamma-1)(1-\rho_g H_p)]}\right)\frac{\partial u}{\partial x}.\end{aligned} \qquad (3.4.19)$$

Therefore the final equations governing the tube velocity, temperature and density are (3.4.15), (3.4.18) and (3.4.19).

3.4.2 Regenerator

The regenerator material by definition has a high heat capacity, so the temperature variation in a cross section of the regenerator is small. The non-ideal properties both for the gas and the regenerator material as well as the real enthalpy and a real gas are now considered. The dimensional equations for mass, momentum, energy transfer and the

equation of state in the regenerator ($0 < x < L_r$) are

$$\frac{\partial \rho_g}{\partial t} + \frac{\partial}{\partial x}(\rho_g u) = 0, \tag{3.4.20}$$

$$\frac{\partial p}{\partial x} = -\frac{\mu}{\phi k} u, \tag{3.4.21}$$

$$\rho_r c_r \frac{\partial T_r}{\partial t} = \frac{\beta}{(1-\phi)}(T_g - T_r) + \frac{\partial}{\partial x}(k_r \frac{\partial T_r}{\partial x}), \tag{3.4.22}$$

$$\rho_g \phi \frac{Dh}{Dt} = \beta(T_r - T_g) + \phi \frac{Dp}{Dt} + \phi \frac{\partial}{\partial x}(k_g \frac{\partial T_g}{\partial x}), \tag{3.4.23}$$

$$(p + \frac{a}{V_m^2})(V_m - b) = RT_g, \tag{3.4.24}$$

where the porosity ϕ is constant. The enthalpy h is defined by (3.1.9) and H_p by (3.4.7). The energy equation for real gas inside the regenerator (3.4.23) reads

$$\rho_g \phi c_p \frac{DT_g}{Dt} = \beta(T_r - T_g) + \phi(1 - \frac{\rho_g H_p}{M})\frac{Dp}{Dt} + \phi \frac{\partial}{\partial x}(k_g \frac{\partial T_g}{\partial x}). \tag{3.4.25}$$

The equations (3.4.9), (3.4.20), (3.4.21), (3.4.22) and (3.4.25) are now turned into dimensionless form as follows

$$\frac{\partial \hat{\rho}_g}{\partial \hat{t}} + \frac{\partial}{\partial \hat{x}}(\hat{\rho}_g \hat{u}) = 0, \tag{3.4.26}$$

$$\frac{p_{av}\omega}{\bar{u}} \frac{\partial \hat{p}}{\partial \hat{x}} = -\frac{\bar{\mu}}{\phi \bar{k}} \bar{u} \hat{\mu} \hat{u}, \tag{3.4.27}$$

$$\rho_r(1-\phi)\bar{c}_r \hat{c}_r T_a \omega \frac{\partial \hat{T}_r}{\partial \hat{t}} = \beta T_a(\hat{T}_g - \hat{T}_r) + (1-\phi)\bar{k}_r T_a \frac{\omega^2}{\bar{u}^2}\frac{\partial}{\partial \hat{x}}(\hat{k}_r \frac{\partial \hat{T}_r}{\partial \hat{x}}), \tag{3.4.28}$$

$$(\bar{\rho}_g \phi \bar{c}_p T_a \omega)\hat{\rho}_g \hat{c}_p \frac{D\hat{T}_g}{D\hat{t}} = \beta T_a(\hat{T}_r - \hat{T}_g) + \phi p_{av}\omega(1 - \hat{\rho}_g \hat{H}_p)\frac{D\hat{p}}{D\hat{t}} \tag{3.4.29}$$

$$+\phi \bar{k}_g T_a \frac{\omega^2}{\bar{u}^2}\frac{\partial}{\partial \hat{x}}(\hat{k}_g \frac{\partial \hat{T}_g}{\partial \hat{x}}),$$

$$p_{av}\hat{p} = R_m \bar{\rho}_g T_a \frac{\hat{\rho}_g \hat{T}}{1 - b_m \bar{\rho}_g \hat{\rho}_g} - a_m \bar{\rho}_g^2 \hat{\rho}_g^2, \tag{3.4.30}$$

where the permeability is assumed to be constant. By dropping the hats we get

$$\frac{D\rho_g}{Dt} = -\rho_g \frac{\partial u}{\partial x}, \tag{3.4.31}$$

$$\frac{\partial p}{\partial x} = -D\mu u, \tag{3.4.32}$$

$$c_r \frac{\partial T_r}{\partial t} = \mathcal{E}\mathcal{F}(T_g - T_r) + \frac{1}{Pe_r}\frac{\partial}{\partial x}(k_r \frac{\partial T_r}{\partial x}), \tag{3.4.33}$$

$$\rho_g c_p \frac{DT_g}{Dt} = \mathcal{E}(T_r - T_g) + \frac{\mathcal{B}(\gamma - 1)}{\gamma}(1 - \rho_g H_p)\frac{Dp}{Dt} + \frac{1}{Pe_g}\frac{\partial}{\partial x}(k_g \frac{\partial T_g}{\partial x}), \tag{3.4.34}$$

$$p = \frac{\rho_g T_g}{\mathcal{B}(1 - \mathcal{N}\rho_g)} - \mathcal{M}\rho_g^2, \tag{3.4.35}$$

where $\mathcal{M}, \mathcal{N}$ are defined by (3.4.16). Substituting the density and gas temperature material derivative from the equations (3.4.31) and (3.4.34) into the pressure material derivative (3.4.17), we obtain the following velocity gradient equation

$$
\frac{\partial u}{\partial x} = \frac{1}{\left(\frac{T_g}{B(1-\mathcal{N}\rho_g)^2} - 2\mathcal{M}\rho_g \right)\mathcal{B}c_p\rho_g(1-\mathcal{N}\rho_g)} \left(\mathcal{E}(T_r - T_g) + \frac{1}{Pe_g}\frac{\partial}{\partial x}(k_g \frac{\partial T_g}{\partial x}) \right)
$$
$$
- \frac{1}{\rho_g \left(\frac{T_g}{B(1-\mathcal{N}\rho_g)^2} - 2\mathcal{M}\rho_g \right)} \left(1 - \frac{(\gamma-1)(1-\rho_g H_p)}{\gamma c_p(1-\mathcal{N}\rho_g)} \right) \frac{Dp}{Dt}.
$$

(3.4.36)

Replacing the density material derivative from (3.4.31) into the pressure material derivative (3.4.17) and substituting it into the energy equation (3.4.34) gives the following evolution equation for the gas temperature in the regenerator

$$
\frac{DT_g}{Dt} = \frac{1}{\rho_g} \left[\frac{\gamma(1-\mathcal{N}\rho_g)}{\gamma c_p(1-\mathcal{N}\rho_g) - (\gamma-1)(1-\rho_g H_p/M)} \right] \left(\mathcal{E}(T_r - T_g) + \frac{1}{Pe_g}\frac{\partial}{\partial x}(k_g \frac{\partial T_g}{\partial x}) \right)
$$
$$
- \left(\frac{(\gamma-1)(1-\rho_g H_p)[T_g - 2\mathcal{M}\mathcal{B}\rho_g(1-\mathcal{N}\rho_g)^2]}{(1-\mathcal{N}\rho_g)[\gamma c_p(1-\mathcal{N}\rho_g) - (\gamma-1)(1-\rho_g H_p/M)]} \right) \frac{\partial u}{\partial x}.
$$

(3.4.37)

Then the final equations governing the regenerator variables are the density relation (3.4.35), the pressure gradient equation (3.4.32), the regenerator material temperature equation (3.4.33), the velocity gradient equation (3.4.36) and the gas temperature equation (3.4.37).

3.4.3 Boundary and initial conditions

To complete the system of equations (3.4.15), (3.4.18) and (3.4.19) for the tube, we need boundary and initial conditions. The boundary condition for the gas velocity in the tube in the case of real gas is the same as ideal gas, because it is applied at the hot end. The assumption of ideal gas at room temperature is not far from reality. The boundary condition for the velocity at the buffer side as the resistance law over the orifice (3.2.60) is described already in Section 3.2.3.
The boundary condition for the real gas temperature in the tube is similar to the one in the ideal case (3.2.68)-(3.2.69). This means that the boundary condition for equation (3.4.19) depends on flow direction according to

$$
\begin{cases}
T_g(0,t) = T_C & \text{if} \quad u(0,t) \geq 0, \\
\quad \frac{\partial T_g}{\partial x}(0,t) = -\frac{\partial T_g}{\partial t}(0,t)/u(0,t) \\
- \left(\frac{(\gamma-1)(1-\rho_g(0,t)H_p(0,t))[T_g(0,t) - 2\mathcal{M}\mathcal{B}\rho_g(0,t)(1-\mathcal{N}\rho_g(0,t))^2]}{(1-\mathcal{N}\rho_g(0,t))[\gamma c_p(0,t)(1-\mathcal{N}\rho_g(0,t)) - (\gamma-1)(1-\rho_g(0,t)H_p(0,t))]} \right) \frac{\partial u}{\partial x}(0,t)/u(0,t) \\
\hfill \text{if} \quad u(0,t) < 0,
\end{cases}
$$

(3.4.38)

$$
\left\{
\begin{array}{l}
T_g(L,t) = T_H \quad \text{if} \quad u(L,t) \leq 0, \\[2mm]
\dfrac{\partial T_g}{\partial x}(L,t) = -\dfrac{\partial T_g}{\partial t}(L,t)/u(L,t) \\[3mm]
\quad -\left(\dfrac{(\gamma-1)(1-\rho_g(L,t)H_p(L,t))[T_g(L,t) - 2\mathcal{MB}\rho_g(L,t)(1-\mathcal{N}\rho_g(L,t))^2]}{(1-\mathcal{N}\rho_g(L,t))[\gamma c_p(L,t)(1-\mathcal{N}\rho_g(L,t)) - (\gamma-1)(1-\rho_g(L,t)H_p(L,t))]} \right) \dfrac{\partial u}{\partial x}(L,t)/u(L,t) \\[4mm]
\hfill \text{if} \quad u(L,t) > 0,
\end{array}
\right.
\tag{3.4.39}
$$

where the conductivity terms have been ignored. The initial conditions for the velocity and the gas temperature in the tube are taken the same as in the case of ideal gas. See Section 3.2.3.

To complete the system of equations (3.4.32), (3.4.33), (3.4.35), (3.4.36), (3.4.37) for the regenerator, we need boundary and initial conditions.

The prescribed pressure, $p_c(t)$, at the compressor side is the boundary condition for (3.4.32), which is the same as in the ideal case. The thermodynamic pressure in the tube is then defined by (3.2.71).

The boundary condition for the gas velocity equation (3.4.36) is prescribed at the interface with the tube, at CHX, defined as $u_C(t)$ in the case of a single-stage PTR. This boundary condition is derived from the mass conservation relation (3.2.72). The velocity in the regenerator, using $\dot{m} = \rho u A \phi$ and $p_t = p_r$ at CHX (away from the boundary layer close to CHX) is

$$
u_r(L_r,t) = \left(\frac{\rho_{g_t} A_t}{\rho_{g_r} A_r \phi} \right) u_t(0,t),
\tag{3.4.40}
$$

where A_t and A_r are the cross-sectional areas of the tube and the regenerator, respectively.

For the regenerator material temperature equation (3.4.33) in the case of a single-stage PTR we prescribe two Dirichlet boundary conditions as in (3.2.74).

For the gas temperature equation (3.4.37) in the regenerator we introduce two boundary conditions neglecting the conductivity k_g at the boundaries, similar to the ones in the ideal case, as follows

$$
\left\{
\begin{array}{l}
T_g(0,t) = T_H \quad \text{if} \quad u(0,t) \geq 0, \\[2mm]
\dfrac{\partial T_g}{\partial x}(0,t) = -\dfrac{\partial T_g}{\partial t}(0,t)/u(0,t) \\[3mm]
\quad +\dfrac{1}{\rho_g(0,t)} \left[\dfrac{\gamma(1-\mathcal{N}\rho_g(0,t))}{\gamma c_p(0,t)(1-\mathcal{N}\rho_g(0,t)) - (\gamma-1)(1-\rho_g(0,t)H_p(0,t))} \right] (\mathcal{E}[T_r(0,t) - T_g(0,t)])/u(0,t) \\[4mm]
\quad -\left(\dfrac{(\gamma-1)(1-\rho_g(0,t)H_p(0,t))[T_g(0,t) - 2\mathcal{MB}\rho_g(0,t)[1-\mathcal{N}\rho_g(0,t)]^2]}{(1-\mathcal{N}\rho_g(0,t))[\gamma c_p(0,t)(1-\mathcal{N}\rho_g(0,t)) - (\gamma-1)(1-\rho_g(0,t)H_p(0,t))]} \right) \dfrac{\partial u}{\partial x}(0,t)/u(0,t), \\[4mm]
\hfill \text{if} \quad u(0,t) < 0,
\end{array}
\right.
\tag{3.4.41}
$$

$$
\left\{
\begin{array}{l}
T_g(L_r,t) = T_C \quad \text{if} \quad u(L_r,t) \leq 0, \\[2mm]
\dfrac{\partial T_g}{\partial x}(L_r,t) = -\dfrac{\partial T_g}{\partial t}(L_r,t)/u(L_r,t) \\[3mm]
\quad +\dfrac{1}{\rho_g(L_r,t)} \left[\dfrac{\gamma(1-\mathcal{N}\rho_g(L_r,t))}{\gamma c_p(L_r,t)(1-\mathcal{N}\rho_g(L_r,t)) - (\gamma-1)(1-\rho_g(L_r,t)H_p(L_r,t))} \right] (\mathcal{E}[T_r(L_r,t) - T_g(L_r,t)])/u(L_r,t) \\[4mm]
\quad -\left(\dfrac{(\gamma-1)(1-\rho_g(L_r,t)H_p(L_r,t))[T_g(L_r,t) - 2\mathcal{MB}\rho_g(L_r,t)[1-\mathcal{N}\rho_g(L_r,t)]^2]}{(1-\mathcal{N}\rho_g(L_r,t))[\gamma c_p(L_r,t)(1-\mathcal{N}\rho_g(L_r,t)) - (\gamma-1)(1-\rho_g(L_r,t)H_p(L_r,t))]} \right) \dfrac{\partial u}{\partial x}(L_r,t)/u(L_r,t), \\[4mm]
\hfill \text{if} \quad u(L_r,t) > 0.
\end{array}
\right.
\tag{3.4.42}
$$
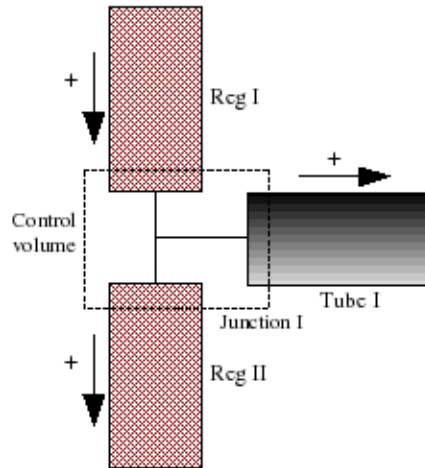
Figure 3.4: Schematic picture of regenerator I, regenerator II and tube I at the junction I showing the control volume and the chosen positive flow direction.

We finally define two similar linear functions similar to the case of ideal gas as the initial conditions for the gas and regenerator material temperatures connecting the cold and the hot ends of the regenerator where the cold end temperature should be approximately close to the equilibrium temperature in the case of pre-assigned temperature at CHX.

3.5 Multi-stage PTR

As an example of multi-staging we model a three-stage PTR. See Figure 2.7. The regenerator material temperatures are considered to be decoupled. This is based on the existence of the gaps in between the stages. This means we compute them at each regenerator locally. The local energy, momentum and mass conservation provide the coupling conditions for the gas velocities, pressures, densities and temperatures at the junctions.

3.5.1 Multi-stage PTR with ideal gas

At the junction connecting the first regenerator, the second regenerator and the first tube we have the following relations in the case of ideal gas and ideal junction. See Figure

3.4. The pressures are the same. This means

$$p_{r_1} = p_{r_2} = p_{t_1} = P. \tag{3.5.1}$$

where P is the uniform thermodynamic pressure in the tube. This means that momentum losses at the junction are ignored. Mass conservation requires

$$\dot{m}_{r_1} = \dot{m}_{r_2} + \dot{m}_{t_1}, \tag{3.5.2}$$

which gives for an ideal gas (using $\dot{m} = \rho u A$)

$$\frac{uA\phi}{T_g}\Big|_{r_1} = \frac{uA\phi}{T_g}\Big|_{r_2} + \frac{uA}{T_g}\Big|_{t_1}. \tag{3.5.3}$$

Energy conservation in terms of enthalpy is given by (heat conductivity is neglected)

$$h^{\star}_{r_1} = h^{\star}_{r_2} + h^{\star}_{t_1}, \tag{3.5.4}$$

where the enthalpy flow $h^{\star}$ is defined by

$$h^{\star} = \dot{m}h. \tag{3.5.5}$$

We now use the ideal gas law (3.1.13) to replace the density in the mass flow, then apply ideal enthalpy relation (3.1.11), assuming constant heat capacity and pressure continuity (3.5.1), and substitute all into (3.5.4) to obtain

$$u\phi A|_{r_1} = u\phi A|_{r_2} + uA|_{t_1}. \tag{3.5.6}$$

This is a simple relation for the velocities at the junction.

3.5.2   Multi-stage PTR with non-ideal gas

In the case of non-ideal gas the junction conditions coupling pressures, velocities, gas and regenerator material temperatures may use similar formula as for the ideal gas but they result differently. The pressure continuity is the same as for ideal gas (3.5.1). Mass conservation in the case of a non-ideal gas is given by (3.5.2)

$$\rho u A \phi|_{r_1} = \rho u A \phi|_{r_2} + \rho u A|_{t_1}. \tag{3.5.7}$$

The energy conservation in the case of a non-ideal gas is the same as for ideal gas (3.5.4). Using the real enthalpy relation (3.1.9) gives

$$\left[\rho_g u \phi A (c_p T_g + \frac{1}{M} H_p P)\right]_{r_1} = \left[\rho_g u \phi A (c_p T_g + \frac{1}{M} H_p P)\right]_{r_2} + \left[\rho_g u A (c_p T_g + \frac{1}{M} H_p P)\right]_{t_1}. \tag{3.5.8}$$

where the pressures, P, are the same according to (3.5.1).
We have defined three conditions valid for ideal and non-ideal gas, so far. In the parts connected to the junction, i.e. regenerator I, regenerator II and tube I (see Figure 3.4), we have the locally governing partial differential equations including two PDEs for the
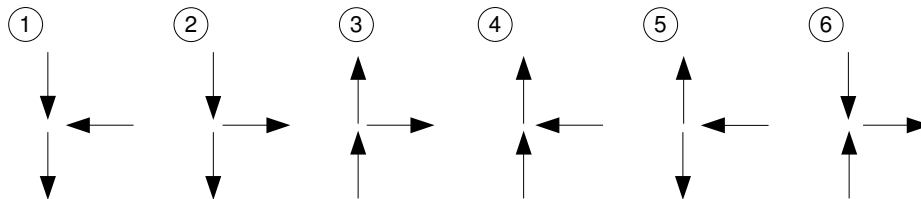
Figure 3.5: The fluid flow possibilities at the junctions I or II connecting two regenerators and one tube.

gas and the material temperatures, and two ODEs for the velocity and pressure for two regenerators, one PDE for the gas temperature and one ODE for the velocity in the tube. The boundary conditions available are one for the velocity in the tube (3.2.60), pressure continuity (3.5.1), mass conservation (3.5.3) or (3.5.7), and energy conservation (3.5.6) or (3.5.8) in the case of ideal or non-ideal gas. The number of boundary conditions, local conservation of mass, momentum and energy, are not sufficient to supply all PDEs and ODEs at the junction. It is explained as follows. The pressure continuity is the pressure boundary condition for each domain. Equation (3.2.60) is the velocity boundary condition for the tubes. The relation (3.5.3) or (3.5.7) is the boundary condition for the regenerator velocities in the case of ideal or non-ideal gas. However, the relation (3.5.6) or (3.5.8) is not sufficient for the gas temperature boundary conditions of the two regenerators and the tube connected to the junction. We thus consider the flow possibilities at the junction to distinguish the proper boundary condition for the gas temperatures at the right flow direction for each domain.

3.5.3   Flow possibilities at the junction

In Figure 3.5 six flow possibilities are depicted. The vertical arrows show the flow at two consecutive regenerators and the horizontal arrow displays the flow to and from the tube at the junction I. See Figure 3.4. These different flows are explained below.

State I: The inflows are from the upper regenerator and the tube. We apply Neumann boundary conditions for both of them at the junction. Mass outflow (3.5.3) or (3.5.8) is used as the boundary condition for the lower regenerator.

State II: In this case there is inflow from the upper regenerator and outflow to the lower regenerator and the tube. We apply a Neumann boundary condition for the upper regenerator. We take the gas temperature of the tube equal to the gas temperature of the upper regenerator. Mass outflow (3.5.3) or (3.5.8) is applied to the junction as the boundary condition for the lower regenerator.

State III: In this case there is inflow from the lower regenerator and outflow to the upper regenerator and the tube. We apply Neumann boundary condition for the lower regenerator. The gas temperature of the tube is take to be equal to the gas temperature of the lower regenerator. Mass conservation (3.5.3) or (3.5.8) is applied to the junction as the boundary condition for the upper regenerator.

State IV: There are inflows from the lower regenerator and the tube. We apply Neumann boundary conditions for both of them. Mass conservation (3.5.3) or (3.5.8) is applied to the junction and this is the boundary condition for the upper regenerator.

State V: Here we have flow distribution from the pulse-tube into the regenerators. In this state, which lasts a very short time during the pressure cycle, a Neumann boundary condition is applied to the pulse-tube. The temperature of the gas entering the regenerators is equal to the temperature of the gas leaving the tube.

State VI: In this flow situation, which lasts for a very short time too, the flow from both regenerators enters the tube. Two Neumann boundary conditions for the gas temperatures are applied to the regenerators. The total mass flow leaving the regenerators is the mass inflow at the tube using (3.5.3) or (3.5.8) as the boundary condition for the tube.

All states representing different boundary conditions for the gas temperatures at the regenerators and the tube at junction I are displayed in Table 3.2. These conditions have the same form at junction II, but for the junction III there is only one regenerator and one tube where the relations will be changed accordingly.

3.6   Conclusion

We derived the mathematical model for the fluid flow and heat transfer inside the pulse-tube refrigerator. The fluid is assumed to be a continuum and Newtonian, compressible and unsteady. The flow is shown to be laminar for the systems considered in Chapters 5 and 6. The heat exchangers are assumed to operate ideally, which means that the gas flowing out of the heat exchanger takes the heat exchanger's temperature, there is no resistance and the heat capacity within the heat exchangers is much larger than

State	Regenerator I	Regenerator II	Tube I
State I	Neumann	(3.5.3) or (3.5.8)	Neumann
State II	Neumann	(3.5.3) or (3.5.8)	$T_{g_{r1}}$
State III	(3.5.3) or (3.5.8)	Neumann	$T_{g_{r2}}$
State IV	(3.5.3) or (3.5.8)	Neumann	Neumann
State V	$T_{g_{t1}}$	$T_{g_{t1}}$	Neumann
State VI	Neumann	Neumann	(3.5.3) or (3.5.8)

Table 3.2: Boundary conditions for the gas temperatures of regenerator I, regenerator II, and tube I at the junction I regarding to different flow possibilities.

of the gas. The basic equations are the three laws of conservation and the equation of state. The four unknowns are the density ρ, the velocity vector **u**, the thermodynamic pressure p, and the absolute temperature T. Other thermodynamic parameters are: the transport properties μ (dynamic viscosity) and k (thermal conductivity) and the specific heat capacity c_p. These parameters are usually temperature and pressure-dependent as already explained in Chapter 2. The equations governing the fluid flow inside the PTR are derived. One-dimensional formulations for the pulse-tube and the regenerator with connecting interface conditions are given. The regenerator formulation and the interface/junction conditions derived in this chapter are new compared to previous work at TUe. An axisymmetrical two-dimensional formulation is considered for the pulse-tube so that wall effects due to heat transfer and friction can be investigated.

One new item in one-dimensionally modelling of multi-stage PTRs is the use of non-ideal gas and non-constant material properties so that a more realistic behaviour of gas and solid, particularly at extremely low temperatures, is obtained. The equation of state is that of Van der Waals. However, it could equally well have been an improved Van der Waals equation of state.

One new addition is that proper junction conditions are formulated for multi-stage pulse-tube refrigerators based on the local conservation of mass, momentum and energy. We consider all the flow possibilities at the junction to define the proper upwind boundary condition for the gas temperatures. This is specially important when the tube

flow enters the junction and is splitted into two flows with opposite directions (or vice versa). Such situation occurs in a very short period of time occurs, but it may lead to numerical instability if not special care is taken.

Chapter 4

Numerical methods

Having constructed the mathematical model, we need to solve the governing equations by proper numerical methods. The first step in obtaining a numerical solution is to discretise the geometric domain, i.e. a numerical grid must be defined. Since the domain of computation in 1D and 2D is simply shaped, a finite difference (FD) method is an appropriate method to discretise the equations. Besides, a domain-decomposition method is applied in the two-dimensional computations for the pulse-tube so that an accurate solution is obtained in an efficient way. The regenerator is still modelled as a 1D body where the effects of friction and heat transfer with the solid are automatically taken into account using the Darcy's law. The ideal gas assumption is not valid for extremely low temperatures. Therefore, in the case of multi-stage PTR, where the last stage is in such a temperature range, we consider real gas as well. The numerical methods are illustrated and tested in a number of incompressible laminar flow problems.

The implementation has been done in MATLAB for the one-dimensional model and in C++ for the two-dimensional model. The two-dimensional simulation has been done in the PETSc (Portable, Extensible Toolkit for Scientific Computation) environment, which is a suite of data structures and routines for the scalable (parallel) solution of partial differential equations.

4.1   Pulse-tube computation

The 1D and 2D energy equations for the pulse-tube describe the convection and the diffusion. We apply an explicit numerical method for the convection term and an implicit method for the diffusion term. A pressure-correction algorithm is used in the two-dimensional computation. The rest of the equations in 1D and 2D are discretised implicitly using a θ-method [39].

4.1.1   One-dimensional tube discretisation

The equations (3.2.32)-(3.2.33) describe the flow and heat transfer in the tube. We introduce computational grids $\{z_j = j\triangle z_j, j = 0, ..., N_z, h = \hat{L}_t/N_z\}$ and $\{t^n = n\triangle t^n, n = 0, ..., N_f\}$ where $\triangle z_j$ is the adaptive space step and $\hat{L}_t$ is the dimensionless length, $L_t\omega/\bar{u}$. Denote by u_j^n the gas velocity and by $T_{g_j}^n$ the gas temperature at the grid point (z_j, t^n). To solve the temperature equation (3.2.33) we chose the following approach [48]:

(i) *Convection* (one-sided difference). Sharp resolution of discontinuities and jumps without excessive smearing and without wiggles require explicit time discretisation and a second-order high-resolution scheme based on flux limiters.

(ii) *Diffusion* (central difference) Explicit schemes lead to stability restrictions of the type $\triangle t = O(\triangle x)$ for the convection term and $\triangle t = O(\triangle x^2)$ for the diffusion term. This last condition is too severe. One of the possibilities to avoid this restriction is to discretise the diffusion term implicitly and for that purpose we use the θ-method with $\theta = 0.5 + \triangle t$ to have second-order accuracy.

(iii) *Velocity gradient*. An explicit central difference is employed.

The unknown velocity in (3.2.33) is taken from the old time-step (n) so that the temperature equation is decoupled from the velocity equation (3.2.32). The old value of the velocity is updated in an iteration step. If $u_j^n \geqslant 0$, we use the following scheme for the temperature equation (3.2.33)

$$T_{g,j}^{n+1} - \triangle t^n\theta\left(b_2(\frac{T_{g,j}^n}{P^n})\frac{T_{g,j+1}^{n+1} - 2T_{g,j}^{n+1} + T_{g,j-1}^{n+1}}{h^2} + (1-\gamma)T_{g,j}^{n+1}\frac{u_{j+1}^n - u_{j-1}^n}{2h}\right) =$$

$$T_{g,j}^n + (1-\theta)\triangle t^n\left(b_2(\frac{T_{g,j}^n}{P^n})\frac{T_{g,j+1}^n - 2T_{g,j}^n + T_{g,j-1}^n}{h^2} + (1-\gamma)T_{g,j}^n\frac{u_{j+1}^n - u_{j-1}^n}{2h}\right)$$

$$-c_j^n\left(1 + \frac{1}{2}(1-c_j^n)\left(\frac{\Phi_{j+\frac{1}{2}}^n}{\mathcal{R}_{j+\frac{1}{2}}^n} - \Phi_{j-\frac{1}{2}}^n\right)\right)(T_{g,j}^n - T_{g,j-1}^n),$$

$$j = 2, ..., N_z - 2, \quad n = 0, ..., N_f - 1.$$

$$(4.1.1)$$

where h is the spatial grid size. If $u_j^n < 0$, then

$$T_{g,j}^{n+1} - \triangle t^n\theta\left(b_2(\frac{T_{g,j}^n}{P^n})\frac{T_{g,j+1}^{n+1} - 2T_{g,j}^{n+1} + T_{g,j-1}^{n+1}}{h^2} + (1-\gamma)T_{g,j}^{n+1}\frac{u_{j+1}^n - u_{j-1}^n}{2h}\right) =$$

$$T_{g,j}^n + (1-\theta)\triangle t^n\left(b_2(\frac{T_{g,j}^n}{P^n})\frac{T_{g,j+1}^n - 2T_{g,j}^n + T_{g,j-1}^n}{h^2} + (1-\gamma)T_{g,j}^n\frac{u_{j+1}^n - u_{j-1}^n}{2h}\right)$$

$$-c_j^n\left(1 - \frac{1}{2}(1+c_j^n)\left(\Phi_{j+\frac{1}{2}}^n - \frac{\Phi_{j-\frac{1}{2}}^n}{\mathcal{R}_{j-\frac{1}{2}}^n}\right)\right)(T_{g,j+1}^n - T_{g,j}^n)$$

$$j = 2, ..., N_z - 2, \quad n = 0, ..., N_f - 1,$$

$$(4.1.2)$$

where c_j^n is the *Courant number*, $c_j^n = \triangle t^n u_j^n / \triangle z$, and $\triangle t^n$ is the adaptive time step. If the CFL (Courant-Friedrichs-Lewy) *stability condition* $|c_j^n| \leq 1$ or, equivalently,

$$\triangle t^n \leq \triangle z / \max_j |u_j^n| \qquad (4.1.3)$$

is satisfied, both schemes are second-order accurate in space away from discontinuities and jumps, and second-order accurate in time, see [51]. The axial space step is denoted as h and the radial space step is denoted as k. The convection term discretisation, $u \partial T_g / \partial x$ is discretised with an upwind scheme of first-order accuracy. The ratio $\mathcal{R}_{j+\frac{1}{2}}^n$ is defined by

$$\mathcal{R}_{j+\frac{1}{2}}^n = \begin{cases} \dfrac{T_j^n - T_{j-1}^n}{T_{j+1}^n - T_{j`}^n} & \text{if} \quad u_j^n > 0, \\[3mm] \dfrac{T_{j+2}^n - T_{j+1}^n}{T_{j+1}^n - T_j^n} & \text{if} \quad u_j^n < 0. \end{cases} \qquad (4.1.4)$$

$\Phi_{j+\frac{1}{2}}^n := \Phi(\mathcal{R}_{j+\frac{1}{2}}^n)$ is the flux limiter. We choose the Van Leer flux limiter [71]

$$\Phi(\mathcal{R}) = \frac{\mathcal{R} + |\mathcal{R}|}{1 + |\mathcal{R}|}. \qquad (4.1.5)$$

For $\mathcal{R} \leq 0$, the limiter function $\Phi(\mathcal{R}) = 0$. This means that only in the vicinity of peaks (jumps), where $\mathcal{R}_{j+\frac{1}{2}}^n < 0$, the high resolution schemes (4.1.1) and (4.1.2) reduce to upwind schemes, which are of first-order accuracy. The boundary conditions (3.2.68) and (3.2.69) are discretised by

$$\begin{cases} T_{g,0} = T_C \quad \text{if} \quad u_0^n \geq 0, \\[2mm] T_{g,0}^{n+1} - \triangle t^n \theta \left((1-\gamma) T_{g,0}^{n+1} (\dfrac{-3u_0^n + 4u_1^n - u_2^n}{2h}) \right) = \\[4mm] T_{g,0}^n + (1-\theta)\triangle t^n \left((1-\gamma) T_{g,0}^n (\dfrac{-3u_0^n + 4u_1^n - u_2^n}{2h}) \right) - c_0^n (T_{g,1}^n - T_{g,0}^n), \quad \text{if} \quad u_0^n < 0, \end{cases} \qquad (4.1.6)$$

$$\begin{cases} T_{g,N_z} = T_H \quad \text{if} \quad u_{N_z}^n \leq 0, \\[2mm] T_{g_{N_z}}^{n+1} - \triangle t^n \theta \left((1-\gamma) T_{g,N_z}^{n+1} (\dfrac{3u_{N_z}^n - 4u_{N_z-1}^n + u_{N_z-2}^n}{2h}) \right) = T_{g,N_z}^n \\[4mm] \quad + (1-\theta)\triangle t^n \left((1-\gamma) T_{g,N_z}^n (\dfrac{3u_{N_z}^n - 4u_{N_z-1}^n + u_{N_z-2}^n}{2h}) \right) - c_{N_z}^n (T_{g,N_z}^n - T_{g,N_z-1}^n), \\[4mm] \hspace{8cm} \text{if} \quad u_{N_z}^n > 0. \end{cases} \qquad (4.1.7)$$

The velocity equation (3.2.32) is discretised using a one-sided second-order formulation for the velocity gradient, a second-order central difference for the temperature conduction term and a one-sided second-order formulation for the pressure time-derivative

as

$$u_{N_z}^{n+1} = u_H^{n+1}, \qquad\qquad\qquad\qquad j = N_z,$$

$$u_{N_z-1}^{n+1} - 4u_{N_z-2}^{n+1} + 3u_{N_z-3}^{n+1} = \frac{2b_1}{hP^n}(T_{g_{N_z}}^{n+1} - 2T_{g_{N_z-1}}^{n+1} + T_{g_{N_z-2}}^{n+1}) - \frac{h}{\gamma P^n}\left(\frac{3P^{n+1} - 4P^n + P^{n-1}}{2\Delta t^n}\right),$$

$$j = N_z - 1,$$

$$-3u_j^{n+1} + 4u_{j+1}^{n+1} - u_{j+2}^{n+1} = \frac{2b_1}{hP^n}(T_{g_{j+1}}^{n+1} - 2T_{g_j}^{n+1} + T_{g_{j-1}}^{n+1}) - \frac{h}{\gamma P^n}\left(\frac{3P^{n+1} - 4P^n + P^{n-1}}{\Delta t^n}\right),$$

$$j = 0, ..., N_z - 2,$$

$$(4.1.8)$$

for every time level $n = 0, 1, 2, 3, ...$ with u_H given by (3.2.60).

Therefore the algorithm to solve the governing equations for the tube (3.2.32), (3.2.33) is as follows:

Algorithm 4.1
Step 0.
Imposing the initial condition
Step 1.
Solve the temperature equations (3.2.33) using (4.1.1) or (4.1.2), taking upwind values at $j = 1, N_z - 1$ for the convection term in combination with the boundary discretisations (4.1.6) and (4.1.7).
Step 2.
Solve the velocity equation (3.2.32) using (4.1.8) to discretise it.
Step 3.
Update and solve the temperature equation using the new velocity at time t^{n+1} only once. ∎

4.1.2 Two-dimensional tube discretisation

We discretise the domain $\Omega = (0 \le z \le L_t) \times (0 \le r \le R_1)$, where L_t is the tube length and R_1 is the external radius of the tube (Figure 3.3), into $(N_z \times (N_R + N_w))$ points where N_z is the number of discretised points in z-direction, N_R is the number of discretised points in radial direction in the fluid and N_w is the number of radial discretised points in the solid wall. The space step in the axial direction is $h = L_t/N_z$, in the radial direction it is $k = R_0/N_R$ in the fluid, and $k_w = (R_1 - R_0)/N_w$ in the wall. A typical grid point is (z_i, r_j) where $i = 0, 1, ..., N_z$ and $j = 0, 1, ..., N_R, N_R + 1, ..., N_R + N_w$. Gas temperature, solid temperature, axial velocity, radial velocity, density and hydrodynamic pressure at discretised point (z_i, r_j) are denoted by T_{ij}, $T_{w,ij}$, u_{ij}, v_{ij}, ρ_{ij} and p_{ij}, respectively.

The non-linear convection-diffusion equation for the temperature, (3.3.26), is discretised in space by central differences and an appropriate flux limiter and the θ-method ($\theta = 0.5 + \Delta t^n$) in time, giving second-order accuracy [51]. For positive velocities $u_{ij}^n > 0$, $v_{ij}^n > 0$ reads

$$T_{ij}^{n+1} - \frac{\Delta t^n}{Pe_g} \frac{\theta}{P(t^{n+1})B} T_j^n$$

$$\left(\frac{1}{r_j} \frac{T_{ij+1}^{n+1} - T_{ij-1}^{n+1}}{2k} + \frac{T_{ij+1}^{n+1} - 2T_{ij}^{n+1} + T_{ij-1}^{n+1}}{k^2} + \frac{T_{i-1j}^{n+1} - 2T_{ij}^{n+1} + T_{i+1j}^{n+1}}{h^2} \right)$$

$$-\Delta t^n \theta \frac{\gamma - 1}{\gamma P(t^{n+1})} \frac{dP}{dt}(t^{n+1}) T_{ij}^{n+1} = T_{ij}^n +$$

$$\frac{\Delta t^n}{Pe_g} \frac{(1-\theta)}{P(t^n)B} T_{ij}^n \left(\frac{1}{r_j} \frac{T_{ij+1}^n - T_{ij-1}^n}{2k} + \frac{T_{ij+1}^n - 2T_{ij}^n + T_{ij-1}^n}{k^2} + \frac{T_{i-1j}^n - 2T_{ij}^n + T_{i+1j}^n}{h^2} \right)$$

$$+\Delta t^n (1-\theta) \frac{\gamma - 1}{\gamma P(t^n)} \frac{dP}{dt}(t^n) T_{ij}^n - c_{ij}^n \left(1 + \frac{1}{2}(1 - c_{ij}^n) \left(\frac{\Phi_{i+\frac{1}{2}j}^n}{\mathcal{R}_{i+\frac{1}{2}j}^n} - \Phi_{i-\frac{1}{2}j}^n \right) \right) (T_{ij}^n - T_{i-1j}^n)$$

$$-d_{ij}^n \left(1 + \frac{1}{2}(1 - d_{ij}^n) \left(\frac{\Phi_{ij+\frac{1}{2}}^n}{\theta_{ij+\frac{1}{2}}^n} - \Phi_{ij-\frac{1}{2}}^n \right) \right) (T_{ij}^n - T_{ij-1}^n),$$

$$i = 2, ..., N_z - 2, \quad j = 2, ..., N_r - 2, \tag{4.1.9}$$

and for negative velocities $u_{ij}^n < 0$, $v_{ij}^n < 0$ we have

$$T_{ij}^{n+1} - \frac{\Delta t^n}{Pe_g} \frac{\theta}{P(t^{n+1})B} T_j^n$$

$$\left(\frac{1}{r_j} \frac{T_{ij+1}^{n+1} - T_{ij-1}^{n+1}}{2k} + \frac{T_{ij+1}^{n+1} - 2T_{ij}^{n+1} + T_{ij-1}^{n+1}}{k^2} + \frac{T_{i-1j}^{n+1} - 2T_{ij}^{n+1} + T_{i+1j}^{n+1}}{h^2} \right)$$

$$-\Delta t^n \theta \frac{\gamma - 1}{\gamma P(t^{n+1})} \frac{dP}{dt}(t^{n+1}) T_{ij}^{n+1} = T_{ij}^n +$$

$$\frac{\Delta t^n}{Pe_g} \frac{(1-\theta)}{P(t^n)B} T_{ij}^n \left(\frac{1}{r_j} \frac{T_{ij+1}^n - T_{ij-1}^n}{2k} + \frac{T_{ij+1}^n - 2T_{ij}^n + T_{ij-1}^n}{k^2} + \frac{T_{i-1j}^n - 2T_{ij}^n + T_{i+1j}^n}{h^2} \right)$$

$$+\Delta t^n (1-\theta) \frac{\gamma - 1}{\gamma P(t^n)} \frac{dP}{dt}(t^n) T_{ij}^n - c_{ij}^n \left(1 - \frac{1}{2}(1 + c_{ij}^n) \left(\frac{\Phi_{i+\frac{1}{2}j}^n}{\mathcal{R}_{i+\frac{1}{2}j}^n} - \Phi_{i-\frac{1}{2}j}^n \right) \right) (T_{i+1j}^n - T_{ij}^n)$$

$$-d_{ij}^n \left(1 - \frac{1}{2}(1 + d_{ij}^n) \left(\frac{\Phi_{ij+\frac{1}{2}}^n}{\theta_{ij+\frac{1}{2}}^n} - \Phi_{ij-\frac{1}{2}}^n \right) \right) (T_{ij+1}^n - T_{ij}^n),$$

$$i = 2, ..., N_z - 2, \quad j = 2, ..., N_r - 2. \tag{4.1.10}$$

Here c_{ij}^n and d_{ij}^n are the Courant numbers $c_{ij}^n := \Delta t^n u_{ij}^n / h$ and $d_{ij}^n := \Delta t^n v_{ij}^n / k$. $\Phi_{j+\frac{1}{2}}^n := \Phi(\mathcal{R}_{j+\frac{1}{2}}^n)$ is the flux limiter. We choose the Van Leer flux limiter

$$\Phi(\mathcal{R}) = \frac{\mathcal{R} + |\mathcal{R}|}{1 + |\mathcal{R}|}. \tag{4.1.11}$$

For different signs of the velocities similar formulas can be derived. The ratio $\mathcal{R}_{ij}$, which can be thought of as a measure of the smoothness of the temperature, is defined as

$$\mathcal{R}_{i+\frac{1}{2}j}^n := \begin{cases} \dfrac{T_{ij}^n - T_{i-1j}^n}{T_{i+1j}^n - T_{ij}^n} & \text{if } u_{ij}^n > 0 \\[3mm] \dfrac{T_{i+2j}^n - T_{i+1j}^n}{T_{i+1j}^n - T_{ij}^n} & \text{if } u_{ij}^n < 0 \end{cases}, \tag{4.1.12}$$

$$\mathcal{R}_{ij+\frac{1}{2}}^n := \begin{cases} \dfrac{T_{ij}^n - T_{ij-1}^n}{T_{ij+1}^n - T_{ij}^n} & \text{if } v_{ij}^n > 0 \\[3mm] \dfrac{T_{ij+2}^n - T_{ij+1}^n}{T_{ij+1}^n - T_{ij}^n} & \text{if } v_{ij}^n < 0 \end{cases}. \tag{4.1.13}$$

The solid wall equation (3.3.28) is discretised by using a uniform grid and second-order schemes in space and θ-method in time as follows

$$\frac{T_{w,ij}^{n+1} - T_{w,ij}^n}{\Delta t^n} =$$

$$\theta Fo \left(\frac{1}{r_j} \frac{T_{w,ij+1}^{n+1} - T_{w,ij-1}^{n+1}}{2k_w} + \frac{T_{w,ij+1}^{n+1} - 2T_{w,ij}^{n+1} + T_{w,ij-1}^{n+1}}{k_w^2} + \frac{T_{w,i-1j}^{n+1} - 2T_{w,ij}^{n+1} + T_{w,i+1j}^{n+1}}{h^2} \right)$$

$$+(1-\theta)Fo \left(\frac{1}{r_j} \frac{T_{w,ij+1}^n - T_{w,ij-1}^n}{2k_w} + \frac{T_{w,ij+1}^n - 2T_{w,ij}^n + T_{w,ij-1}^n}{k_w^2} + \frac{T_{i-1j}^n - 2T_{w,ij}^n + T_{w,i+1j}^n}{h^2} \right),$$

$$i = 1, ..., N_z - 1, \quad j = N_r + 1, ..., N_w - 1. \tag{4.1.14}$$

At the interface ($j = N_r$) we use the following approximation of (3.3.35)

$$\frac{T_{ij}^{n+1} - T_{ij-1}^{n+1}}{k} = \beta_w \frac{T_{w,ij+1}^{n+1} - T_{w,ij}^{n+1}}{k_w}, \; i = 1, ..., N_z - 1. \tag{4.1.15}$$

We choose a time step satisfying the CFL condition $|c_{ij}^n| \le 1$, $|d_{ij}^n| \le 1$, i.e.

$$\Delta t^n \le \min_j \{ h / \max_{ij} |u_{ij}^n|, k_j / \max_{ij} |v_{ij}^n| \}. \tag{4.1.16}$$

The density in an ideal gas is then obtained from (3.2.15) as

$$\rho_{ij}^{n+1} = \frac{P\mathcal{B}}{T_{ij}^{n+1}}. \tag{4.1.17}$$

4.1.3 Pressure correction algorithm for the 2D velocity field

Having calculated the temperature T^{n+1} from (4.1.9) or (4.1.10), T_w^{n+1} from (4.1.14) and the density ρ^{n+1} from (4.1.17), we compute the velocities u^{n+1}, v^{n+1} and the hydrodynamic pressure p^{n+1} via the momentum equations (3.3.21), (3.3.22) and the velocity constraint (3.3.25). We apply a previously tested pressure-correction algorithm [48] which was shown to have good performance and the present study confirms the achievement of this previous work. All pressure-correction algorithms consist of three steps. First, we guess the velocities from old data as a predictor step. Second, we modify these old values in a corrector step, because they do not meet the velocity constraint equation (3.3.25). Substitution of the modified velocities into the velocity constraint equation leads us to a Poisson equation for the pressure correction. Third, by solving this Poisson equation and thus computing the corrected pressure we modify the velocity field again. The predictor horizontal and vertical velocities, the first-order pressure and the pressure corrector at the grid point (z_i, r_j) at the time level t^n are denoted by u_{ij}^*, v_{ij}^*, p_{ij}^n and q_{ij}, respectively. In the following we describe the algorithm that is applied in our computations.

(i) prediction step:

We discretise the equations (3.3.21) and (3.3.22) to calculate the predictor velocities u_{ij}^*, v_{ij}^* with the pressure as the old time level t^n as follows

$$\frac{u_{ij}^* - u_{ij}^n}{\Delta t^n} = M(u_{ij}^*) - \frac{1}{\rho_{ij}^{n+1}} \frac{p_{i+1j}^n - p_{ij}^n}{h}, \tag{4.1.18}$$

$$\frac{v_{ij}^* - v_{ij}^n}{\Delta t^n} = N(v_{ij}^*) - \frac{1}{\rho_{ij}^{n+1}} \frac{p_{ij+1}^n - p_{ij}^n}{k}, \tag{4.1.19}$$

$$i = 1, 2, ..., N_z - 1, \quad j = 1, 2, ..., N_R - 1,$$

where

$$M(u_{ij}^*) = -u_{ij+}^n \frac{u_{ij}^* - u_{i-1j}^*}{h} - u_{ij-}^n \frac{u_{i+1j}^* - u_{ij}^*}{h} - v_{ij+}^n \frac{u_{ij}^* - u_{ij-1}^*}{k} - v_{ij-}^n \frac{u_{ij+1}^* - u_{ij}^*}{k} +$$
$$+ \frac{1}{\text{Re}} \frac{1}{\rho_{ij}^{n+1}} \left[\frac{u_{ij+1}^* - 2u_{ij}^* + u_{ij-1}^*}{k^2} + \frac{1}{r_j} \frac{u_{ij+1}^* - u_{ij-1}^*}{2k} + \frac{4}{3} \frac{u_{i+1j}^* - 2u_{ij}^* + u_{i-1j}^*}{h^2} \right] +$$
$$+ \frac{1}{\text{Re}} \frac{1}{\rho_{ij}^{n+1}} \left[\frac{1}{3} \frac{1}{r_j} \frac{v_{i+1j}^n - v_{i-1j}^n}{2h} + \frac{1}{3} \frac{v_{i+1j+1}^n - v_{i-1j+1}^n - v_{i+1j-1}^n + v_{i-1j-1}^n}{4hk} \right], \tag{4.1.20}$$

$$N(v_{ij}^*) = -u_{ij+}^n \frac{v_{ij}^* - v_{i-1j}^*}{h} - u_{ij-}^n \frac{v_{i+1j}^* - v_{ij}^*}{h} - v_{ij+}^n \frac{v_{ij}^* - v_{ij-1}^*}{k} - v_{ij-}^n \frac{v_{ij+1}^* - v_{ij}^*}{k} +$$

$$+ \frac{1}{Re} \frac{1}{\rho_{ij}^{n+1}} \left[\frac{4}{3} \frac{v_{ij+1}^* - 2v_{ij}^* + v_{ij-1}^*}{k^2} + \frac{2}{3} \frac{1}{r_j} \frac{v_{ij+1}^* - v_{ij-1}^*}{2k} + \frac{v_{i+1j}^* - 2v_{ij}^* + v_{i-1j}^*}{h^2} \right] +$$

$$+ \frac{1}{Re} \frac{1}{\rho_{ij}^{n+1}} \left[-\frac{2}{3} \frac{1}{r_j} \frac{u_{i+1j}^n - u_{i-1j}^n}{2h} + \frac{1}{3} \frac{u_{i+1j+1}^n - u_{i-1j+1}^n - u_{i+1j-1}^n + u_{i-1j-1}^n}{4hk} \right],$$

$$\tag{4.1.21}$$

$$u_{ij+}^n = \max(u_i^n, 0), \tag{4.1.22}$$

$$u_{ij-}^n = \min(u_i^n, 0), \tag{4.1.23}$$

$$v_{ij+}^n = \max(v_i^n, 0), \tag{4.1.24}$$

$$v_{ij-}^n = \min(v_i^n, 0). \tag{4.1.25}$$

(ii) correction step:

Here we express the velocity field correctors u_{ij}, v_{ij} with the pressure p_{ij} at the new time level t^{n+1} by the same discretisation formulas as in the prediction step as follows

$$\frac{u_{ij}^{n+1} - u_{ij}^n}{\Delta t^n} = M(u_{ij}^{n+1}) - \frac{1}{\rho_{ij}^{n+1}} \frac{p_{i+1j}^{n+1} - p_{ij}^{n+1}}{h}, \tag{4.1.26}$$

$$\frac{v_{ij}^{n+1} - v_{ij}^n}{\Delta t^n} = N(v_{ij}^{n+1}) - \frac{1}{\rho_{ij}^{n+1}} \frac{p_{ij+1}^{n+1} - p_{ij}^{n+1}}{k}. \tag{4.1.27}$$

$$i = 1, 2, ..., N_z - 1, \quad j = 1, 2, ..., N_R - 1.$$

If we decompose the operators $M(u_{ij}^*)$ and $N(v_{ij}^*)$ into the following

$$M(u_{ij}^*) = M'(u_{ij}^*) + A_{ij}^n u_{ij}^*, \tag{4.1.28}$$

$$N(v_{ij}^*) = N'(v_{ij}^*) + B_{ij}^n v_{ij}^*, \tag{4.1.29}$$

$$M(u_{ij}^{n+1}) = M'(u_{ij}^*) + A_{ij}^n u_{ij}^{n+1}, \tag{4.1.30}$$

$$N(v_{ij}^{n+1}) = N'(v_{ij}^*) + B_{ij}^n v_{ij}^{n+1}, \tag{4.1.31}$$

where A_{ij}^n, B_{ij}^n are the diagonal components, and $M'(u_{ij}^*)$, $N'(v_{ij}^*)$ are the off-diagonal components of $M(u_{ij}^*)$ and $N(v_{ij}^*)$, respectively. Relations (4.1.30) and (4.1.31) use the off-diagonals $M(u_{ij}^*)$ and $N(v_{ij}^*)$ instead of $M(u_{ij}^{n+1})$ and $N(v_{ij}^{n+1})$. Subtracting the predictor and the corrector velocity fields, i.e. (4.1.18) and (4.1.19) from (4.1.26) and (4.1.27), respectively, eliminates $M(u_{ij}^*)$ and $N(v_{ij}^*)$, and gives

$$u_{ij}^{n+1} = u_{ij}^* - \frac{\Delta t^n}{h} \frac{1}{\rho_{ij}^{n+1}} \frac{1}{C_{ij}^n} [q_{i+1j}^{n+1} - q_{ij}^{n+1}], \tag{4.1.32}$$

$$v_{ij}^{n+1} = v_{ij}^* - \frac{\Delta t^n}{k} \frac{1}{\rho_{ij}^{n+1}} \frac{1}{D_{ij}^n} [q_{ij+1}^{n+1} - q_{ij}^{n+1}], \tag{4.1.33}$$

where the pressure corrector q_{ij} is

$$q_{ij}^{n+1} := p_{ij}^{n+1} - p_{ij}^n. \tag{4.1.34}$$

and

$$C_{ij}^n := 1 - \Delta t^n A_{ij}^n \text{ with } A_{ij}^n = -\frac{1}{h} \left| u_{ij}^n \right| - \frac{1}{k} \left| v_{ij}^n \right| - \frac{1}{Re} \frac{1}{\rho_{ij}^{n+1}} \left(\frac{2}{k^2} + \frac{4}{3} \frac{2}{h^2} \right),$$

$$D_{ij}^n := 1 - \Delta t^n B_{ij}^n \text{ with } B_{ij}^n = -\frac{1}{h} \left| u_{ij}^n \right| - \frac{1}{k} \left| v_{ij}^n \right| - \frac{1}{Re} \frac{1}{\rho_{ij}^{n+1}} \left(\frac{4}{3} \frac{2}{k^2} + \frac{2}{h^2} \right).$$

(iii) pressure correction equation (using the Poisson equation):

We discretise the velocity constraint equation (3.3.25) as follows

$$\frac{u_{ij}^{n+1} - u_{i-1j}^{n+1}}{h} + \frac{v_{ij}^{n+1} - v_{ij-1}^{n+1}}{k} + \frac{v_{ij}^{n+1}}{r_j} = F_{ij}^{n+1}, \tag{4.1.35}$$

where

$$F_{ij}^{n+1} = -\frac{1}{\gamma P(t^{n+1})} \frac{dP}{dt}(t^{n+1}) +$$

$$\frac{1}{BPe} \frac{1}{P(t^{n+1})} \left[\frac{1}{r_j} \frac{T_{ij+1}^{n+1} - T_{ij-1}^{n+1}}{2k} + \frac{T_{ij+1}^{n+1} - 2T_{ij}^{n+1} + T_{ij-1}^{n+1}}{k^2} + \frac{T_{i+1j}^{n+1} - 2T_{ij}^{n+1} + T_{i-1j}^{n+1}}{h^2} \right].$$

Substitution of (4.1.32) and (4.1.33) into (4.1.35) gives the following *Poisson equation*

$$-\frac{\Delta t^n}{h^2} \frac{1}{C_{ij}^n} \frac{1}{\rho_{ij}^{n+1}} \left[q_{i+1j}^{n+1} - q_{ij}^{n+1} \right] + \frac{\Delta t^n}{h^2} \frac{1}{C_{i-1j}^n} \frac{1}{\rho_{i-1j}^{n+1}} \left[q_{ij}^{n+1} - q_{i-1j}^{n+1} \right] -$$

$$\frac{\Delta t^n}{k^2} \frac{1}{D_{ij}^n} \frac{1}{\rho_{ij}^{n+1}} \left[q_{ij+1}^{n+1} - q_{ij}^{n+1} \right] + \frac{\Delta t^n}{k^2} \frac{1}{D_{ij-1}^n} \frac{1}{\rho_{ij-1}^{n+1}} \left[q_{ij}^{n+1} - q_{ij-1}^{n+1} \right] -$$

$$\frac{\Delta t^n}{k} \frac{1}{D_{ij}^n} \frac{1}{\rho_{ij}^{n+1}} \frac{1}{r_j} \left[q_{ij+1}^{n+1} - q_{ij}^{n+1} \right] = F_{ij}^{n+1} - \frac{u_{ij}^* - u_{i-1j}^*}{h} - \frac{v_i^* - v_{ij-1}^*}{k} - \frac{v_{ij}^*}{r_j}. \tag{4.1.36}$$

Equation (4.1.36) is solved for q_{ij}^{n+1}, then u_{ij}^{n+1} and v_{ij}^{n+1} are calculated by (4.1.32) and (4.1.33). The hydrodynamic pressure p_{ij}^{n+1} follows from (4.1.34).
The equations (4.1.18) - (4.1.36) are valid in the interior points of the computational domain. Boundary points are considered separately below.

(iv) Cold end boundary (z = 0), $i = 0$, $j = 0, ..., N_r - 1$:

According to Table 3.1 the radial velocity, v, and the pressure, p, and thus the pressure correction, q, are zero at this boundary, therefore we can use the discretised constraint equation (4.1.35) for the axial velocity and correct it by (4.1.32) as follows

$$\frac{u_{1j}^* - u_{0j}^*}{h} = F_{1j}^{n+1} \tag{4.1.37}$$

and

$$u_{0j}^{n+1} = u_{0j}^* - \frac{\Delta t^n}{h} \frac{1}{\rho_{0j}^{n+1}} \frac{1}{C_{0j}^n} [q_{1j} - q_{0j}], \ v_{0j}^{n+1} = 0, \ q_{0j} = 0. \tag{4.1.38}$$

(v) Hot end boundary (z = L_t), i = N_z, j = 0, ..., N_r - 1:

At this boundary the radial velocity is zero and the axial velocity is given by

$$u_{N_z j}^{n+1} = u_{N_z j}^* = u_H \text{ (given)}, \ v_{N_z j}^{n+1} = v_{N_z j}^* = 0. \tag{4.1.39}$$

So the pressure correction $q_{N_z j}$ can be imposed by the discretised constraint equation (4.1.35) and using it in the Poisson equation (4.1.36) for this boundary as follows

$$\frac{u_H^{n+1} - u_{N_z-1 j}^{n+1}}{h} = F_{N_z j}^{n+1}, \ u_{N_z-1 j}^{n+1} = u_{N_z-1 j}^* - \frac{\Delta t^n}{h} \frac{1}{\rho_{N_z-1 j}^{n+1}} \frac{1}{C_{N_z-1 j}^n} [q_{N_z j} - q_{N_z-1 j}],$$
$$\tag{4.1.40}$$

$$\frac{\Delta t^n}{h^2} \frac{1}{\rho_{N_z-1 j}^{n+1}} \frac{1}{C_{N_z-1 j}^n} [q_{N_z j} - q_{N_z-1 j}] = F_{N_z j}^{n+1} + \frac{u_{N_z-1 j}^* - u_H^{n+1}}{h}. \tag{4.1.41}$$

(vi) Wall boundary (r = R_0): i = 0, ..., N_z, j = N_r:

$$u_{iN_r}^{n+1} = 0, \ v_{iN_r}^{n+1} = 0, \ q_{iN_r}^{n+1} = 0. \tag{4.1.42}$$

(vii) Symmetry boundary (r = 0): i = 1, ..., N_z - 1, j = 0

Because of the singularity of the $1/r$ term in the governing equations, we proceed as follows. A Dirichlet boundary condition for the radial velocity ($v = 0$), and Neumann boundary conditions for the axial velocity and the temperature ($\partial u / \partial r = 0$, $\partial T / \partial r = 0$) hold because of the radial symmetry. We use *L'Hopital's rule*, at $r = 0$ to eliminate singularities present in the equations and replace them by computable quantities as follows:

$$\frac{1}{r} \frac{\partial u}{\partial r} \to \frac{\partial^2 u}{\partial r^2}, \ \frac{v}{r} \to \frac{\partial v}{\partial r}, \ \frac{1}{r} \frac{\partial T}{\partial r} \to \frac{\partial^2 T}{\partial r^2}. \tag{4.1.43}$$

This turns (3.3.21) and (3.3.25) into

$$\rho \left(\frac{\partial u}{\partial t} + u \frac{\partial u}{\partial z} \right) = -\frac{\partial p}{\partial z} + \frac{1}{Re} \left[2 \frac{\partial^2 u}{\partial r^2} + \frac{4}{3} \frac{\partial^2 u}{\partial z^2} + \frac{1}{3} \frac{\partial}{\partial r} (\frac{\partial v}{\partial z}) + \frac{1}{3} \frac{\partial}{\partial z} \left(\frac{\partial v}{\partial r} \right) \right], \tag{4.1.44}$$

$$\frac{\partial u}{\partial z} + 2 \frac{\partial v}{\partial r} = -\frac{1}{\gamma P(t)} \frac{dP}{dt}(t) + \frac{1}{\mathcal{B} P(t)} \left(2 \frac{\partial^2 T}{\partial r^2} + \frac{\partial^2 T}{\partial z^2} \right), \tag{4.1.45}$$

respectively. The following steps give the corresponding pressure correction formulation at the boundary $r = 0$

$$\frac{u_{i0}^* - u_{i0}^n}{\Delta t^n} = M(u_{i0}^*) - \frac{1}{\rho_{i0}^{n+1}} \frac{p_{i+1,0}^n - p_{i,0}^n}{h}, \tag{4.1.46}$$

$$M(u_{i,0}^*) = -u_{i,0+}^n \frac{u_{i,0}^* - u_{i-1,0}^*}{h} - u_{i,0-}^n \frac{u_{i+1,0}^* - u_{i,0}^*}{h}$$
$$+\frac{1}{Re}\frac{1}{\rho_{i0}^{n+1}}\left(4\frac{u_{i,1}^* - u_{i,0}^*}{k^2} + \frac{4}{3}\frac{u_{i+1,0}^* - 2u_{i,0}^* + u_{i-1,0}^*}{h^2} + \frac{2}{3}\frac{v_{i+1,1}^n - v_{i-1,1}^n}{hk}\right). \quad (4.1.47)$$

Using

$$\frac{u_{i,0}^{n+1} - u_{i-1,0}^{n+1}}{h} + \frac{2v_{i,1}^{n+1}}{k} = F_{i,0}^{n+1} \quad (4.1.48)$$

to approximate (4.1.45) leads to

$$-\frac{\Delta t}{h^2}\frac{1}{\rho_{i,0}^{n+1}C_{i,0}^n}(q_{i+1,0}^{n+1} - q_{i,0}^{n+1}) + \frac{\Delta t}{h^2}\frac{1}{\rho_{i-1,0}^{n+1}C_{i-1,0}^n}(q_{i,0}^{n+1} - q_{i-1,0}^{n+1})$$
$$+2\frac{\Delta t}{k^2}\frac{1}{\rho_{i,1}^{n+1}D_{i,1}^n}(q_{i,2}^{n+1} - q_{i,1}^{n+1}) = F_{i,0}^{n+1} - \frac{u_{i,0}^* - u_{i-1,0}^*}{h} - \frac{2v_{i,1}^*}{k}, \quad (4.1.49)$$

with

$$F_{i,0}^{n+1} = -\frac{1}{\gamma P(t)}\frac{dP}{dt}(t) + \frac{1}{\mathcal{B}P(t)}\left[4\frac{T_{i,1}^{n+1} - T_{i,0}^{n+1}}{k^2} + \frac{T_{i-1,0}^{n+1} - 2T_{i,0}^{n+1} + T_{i+1,0}^{n+1}}{h^2}\right].$$

Using the interior and boundary conditions discretised formulations, we summarise the three steps to find the three unknowns u^{n+1}, v^{n+1} and p^{n+1}

Algorithm 4.2
Step 0:
Imposing the initial conditions. *Step 1*:
Solve (4.1.18) and (4.1.19) to find u^* and v^* with corresponding boundary conditions.
Step 2:
Substitute u^* and v^* into (4.1.36) to find the pressure corrector q.
Step 3:
Compute u^{n+1}, v^{n+1} and p^{n+1} through (4.1.32), (4.1.33) and (4.1.34), respectively, with corresponding boundary conditions. ■

4.1.4 One-dimensional tube discretisation with real gas

For real gas the equation of state is not linear in density and we need to solve it to find the density at each time step. We rearrange the dimensionless form of the equation of state (3.4.15) to obtain a third-degree equation for ρ_g

$$\mathcal{MBN}\rho_g^3 - \mathcal{MB}\rho_g^2 + (P\mathcal{BN} + T_g)\rho_g - P\mathcal{B} = 0. \quad (4.1.50)$$

We apply Newton's method, which will be explained later on, to find the density at each discretised point. Having computed the density we solve the equation for the gas temperature T_g in the tube (3.4.19) using the computed values for the density at time step $n + 1$ and old data for the velocity, gas conductivity k_g, heat capacity c_g, and second term of enthalpy H_p, as follows (for $u_j^n > 0$)

$$T_{g,j}^{n+1} - \triangle t^n \theta \frac{1}{\rho_{g,j}^{n+1}} \frac{\gamma(1 - \mathcal{N}\rho_{g,j}^{n+1})}{c_{g,j}^n(1 - \mathcal{N}\rho_{g,j}^{n+1}) - (\gamma - 1)(1 - \rho_{g,j}^{n+1}H_{p,j}^n)} \left(\frac{k_{g,j}^n}{Pe_g} \frac{T_{g,j+1}^{n+1} - 2T_{g,j}^{n+1} + T_{g,j-1}^{n+1}}{h^2} \right)$$

$$= T_{g,j}^n + (1 - \theta)\triangle t^n \frac{1}{\rho_{g,j}^{n+1}} \frac{\gamma(1 - \mathcal{N}\rho_{g,j}^{n+1})}{c_{g,j}^n(1 - \mathcal{N}\rho_{g,j}^{n+1}) - (1 - \gamma)(1 - \rho_{g,j}^{n+1}H_{p,j}^n)} \left(\frac{k_{g,j}^n}{Pe_g} \frac{T_{g,j-1}^n - 2T_{g,j}^n + T_{g,j+1}^n}{h^2} \right)$$

$$- \frac{(\gamma - 1)(1 - \rho_{g,j}^{n+1}H_{p,j}^n)[T_{gj}^n - 2\mathcal{M}\mathcal{B}\rho_{g,j}^{n+1}(1 - \mathcal{N}\rho_{g,j}^{n+1})^2]}{(1 - \mathcal{N}\rho_{g,j}^{n+1})[\gamma c_{g,j}^n(1 - \mathcal{N}\rho_{g,j}^{n+1}) - (\gamma - 1)(1 - \rho_{g,j}^{n+1}H_{p,j}^n)]} (\frac{u_{j+1}^n - u_{j-1}^n}{h^2})$$

$$- c_j^n \left(1 + \frac{1}{2}(1 - c_j^n) \left(\frac{\Phi_{j+\frac{1}{2}}^n}{r_{j+\frac{1}{2}}^n} - \Phi_{j-\frac{1}{2}}^n \right) \right) (T_{g,j}^n - T_{g,j-1}^n)$$

$$j = 2, ..., N_x - 2, \qquad n = 0, ..., N_f - 1. \tag{4.1.51}$$

for $j = 1, N_x - 1$ we apply the upwind flux limiters for the convection term. The boundary conditions, i.e. $j = 0, N_x$ are discretised the same way as for the ideal case with corresponding non-ideal terms.

The velocity equation (3.4.18) is discretised using a one-sided second-order formulation for the velocity gradient, the second-order central difference scheme for the diffusion term and a one-sided second-order formulation for the pressure time-derivative. The dimensionless boundary condition for the tube velocity u_H at the hot end is given by (3.2.60). This results in

$$u_{N_z}^{n+1} = u_H^{n+1}, \qquad\qquad\qquad j = N_z,$$

$$u_{N_z-1}^{n+1} - 4u_{N_z-2}^{n+1} + 3u_{N_z-3}^{n+1} =$$

$$\frac{2hk_{g,N_z-1}^n}{(\frac{T_{g,N_z-1}^n}{B(1 - \mathcal{N}\rho_{g,N_z-1}^n)^2} - 2\mathcal{M}\rho_{g,N_z-1}^n)\mathcal{B}c_{g,N_z-1}^n\rho_{g,N_z-1}^n(1 - \mathcal{N}\rho_{g,N_z-1}^n)} \left(\frac{1}{Pe_g} \frac{T_{g,N_z}^{n+1} - 2T_{g,N_z-1}^{n+1} + T_{g,N_z-2}^{n+1}}{h^2} \right)$$

$$- \frac{2h}{\rho_{g,N_z-1}^n(\frac{T_{g,N_z-1}^n}{B(1 - \mathcal{N}\rho_{g,N_z-1}^n)^2} - 2\mathcal{M}\rho_{g,N_z-1}^n)} \left(1 - \frac{(\gamma - 1)(1 - \rho_{g,N_z-1}^nH_{p,N_z-1}^n)}{\gamma c_{g,N_z-1}^n(1 - \mathcal{N}\rho_{g,N_z-1}^n)} \right) \frac{3P^{n+1} - 4P^n + P^{n-1}}{2\Delta t}.$$

$$j = N_z - 1,$$

$$-3u_j^{n+1} + 4u_{j+1}^{n+1} - u_{j+2}^{n+1} =$$

$$\frac{2hk_{g,j}^n}{(\frac{T_{g,j}^n}{B(1 - \mathcal{N}\rho_{g,j}^n)^2} - 2\mathcal{M}\rho_{g,j}^n)\mathcal{B}c_{g,j}^n\rho_{g,j}^n(1 - \mathcal{N}\rho_{g,j}^n)} \left(\frac{1}{Pe_g} \frac{T_{g,j+1}^{n+1} - 2T_{g,j}^{n+1} + T_{g,j-1}^{n+1}}{h^2} \right)$$

$$- \frac{2h}{\rho_{g,j}^n(\frac{T_{g,j}^n}{B(1 - \mathcal{N}\rho_{g,j}^n)^2} - 2\mathcal{M}\rho_{g,j}^n)} \left(1 - \frac{(\gamma - 1)(1 - \rho_{g,j}^nH_{p,j}^n)}{\gamma c_{g,j}^n(1 - \mathcal{N}\rho_{g,j}^n)} \right) \frac{3P^{n+1} - 4P^n + P^{n-1}}{2\Delta t}.$$

$$j = 0, ..., N_z - 2, \tag{4.1.52}$$

The discretised equations use old data, e.g. for the velocity and density. An iteration method is applied to update the old values during computation. We are left with the three equations (4.1.50), (4.1.51) and (4.1.52) for the three variables ρ_g, u and T_g. To solve these equations we apply the following algorithm.

Algorithm 4.3 (*Prediction-correction algorithm*)

Step 1: (Prediction)
Solve the density equation (4.1.50) using Newton's method with old values for the density as the initial guess and old data for the gas temperature and pressure in the equation. Thus the predicted values for the density satisfy

$$\mathcal{MBN}\tilde{\rho}_g^3 - \mathcal{MB}\tilde{\rho}_g^2 + (P^n\mathcal{BN} + T_g^n)\tilde{\rho}_g - P^n\mathcal{B} = 0.$$

Step 2.
Solve (3.4.19) via (4.1.51) and (3.4.18) via (4.1.52) to find T_g and u with density replaced by $\tilde{\rho}_g$ calculated in Step 1

$$\frac{D\tilde{T}_g}{Dt} = \frac{1}{\tilde{\rho}_g}\left[\frac{\gamma(1 - \mathcal{N}\tilde{\rho}_g)}{\gamma c_g^n(1 - \mathcal{N}\tilde{\rho}_g) - (\gamma - 1)(1 - \tilde{\rho}_g H_p^n)}\right]\left(\frac{1}{Pe_g}\frac{\partial}{\partial x}(k_g^n \frac{\partial \tilde{T}_g}{\partial x})\right)$$
$$- \left(\frac{(\gamma - 1)(1 - \tilde{\rho}_g H_p^n)[T_g^n - 2\mathcal{MB}\tilde{\rho}_g(1 - \mathcal{N}\tilde{\rho}_g)^2]}{(1 - \mathcal{N}\tilde{\rho}_g)[\gamma c_g^n(1 - \mathcal{N}\tilde{\rho}_g) - (\gamma - 1)(1 - \tilde{\rho}_g H_p^n)]}\right)\frac{\partial u^n}{\partial x}.$$

$$\frac{\partial \tilde{u}}{\partial x} = \frac{1}{(\frac{\tilde{T}_g}{B(1 - \mathcal{N}\tilde{\rho}_g)^2} - 2\mathcal{M}\tilde{\rho}_g)\mathcal{B}c_g^n\tilde{\rho}_g(1 - \mathcal{N}\tilde{\rho}_g)}\left(\frac{1}{Pe_g}\frac{\partial}{\partial x}(k_g^n \frac{\partial \tilde{T}_g}{\partial x})\right)$$
$$- \frac{1}{\tilde{\rho}_g(\frac{\tilde{T}_g}{B(1 - \mathcal{N}\tilde{\rho}_g)^2} - 2\mathcal{M}\tilde{\rho}_g)}\left(1 - \frac{(\gamma - 1)(1 - \tilde{\rho}_g H_p^n)}{\gamma c_g^n(1 - \mathcal{N}\tilde{\rho}_g)}\right)\frac{D\tilde{P}}{Dt}.$$

Step 3: (Correction)
Solve the density equation with predicted data $\tilde{T}_g$ and $\tilde{P}$ in the equation and $\tilde{\rho}_g$ as initial guess from

$$\mathcal{MBN}(\rho_g^{n+1})^3 - \mathcal{MB}(\rho_g^{n+1})^2 + (\tilde{P}\mathcal{BN} + \tilde{T}_g)\rho_g^{n+1} - \tilde{P}\mathcal{B} = 0.$$

Step 4.
Solve (4.1.51) and (4.1.52) to obtain the corrected solution. This gives

$$\frac{DT_g^{n+1}}{Dt} = \frac{1}{\rho_g^{n+1}}\left[\frac{\gamma(1 - \mathcal{N}\rho_g^{n+1})}{\gamma\tilde{c}_g(1 - \mathcal{N}\rho_g^{n+1}) - (\gamma - 1)(1 - \rho_g^{n+1}\tilde{H}_p)}\right]\left(\frac{1}{Pe_g}\frac{\partial}{\partial x}(\tilde{k}_g \frac{\partial T_g^{n+1}}{\partial x})\right)$$
$$- \left(\frac{(\gamma - 1)(1 - \rho_g^{n+1}\tilde{H}_p)[\tilde{T}_g - 2\mathcal{MB}\rho_g^{n+1}(1 - \mathcal{N}\rho_g^{n+1})^2]}{(1 - \mathcal{N}\rho_g^{n+1})[\gamma\tilde{c}_g(1 - \mathcal{N}\rho_g^{n+1}) - (\gamma - 1)(1 - \rho_g^{n+1}\tilde{H}_p)]}\right)\frac{\partial \tilde{u}}{\partial x}.$$

$$\frac{\partial u^{n+1}}{\partial x} = \frac{1}{(\frac{T_g^{n+1}}{B(1 - \mathcal{N}\rho_g^{n+1})^2} - 2\mathcal{M}\rho_g^{n+1})\mathcal{B}\tilde{c}_g\rho_g^{n+1}(1 - \mathcal{N}\rho_g^{n+1})}\left(\frac{1}{Pe_g}\frac{\partial}{\partial x}(\tilde{k}_g \frac{\partial T_g^{n+1}}{\partial x})\right)$$
$$- \frac{1}{\rho_g^{n+1}(\frac{T_g^{n+1}}{B(1 - \mathcal{N}\rho_g^{n+1})^2} - 2\mathcal{M}\rho_g^{n+1})}\left(1 - \frac{(\gamma - 1)(1 - \rho_g^{n+1}\tilde{H}_p)}{\gamma\tilde{c}_g(1 - \mathcal{N}\rho_g^{n+1})}\right)\frac{DP^{n+1}}{Dt}.$$

∎

4.2   Regenerator computation

The governing equations for the regenerator filled with ideal gas are (3.2.47), (3.2.53), (3.2.49) and (3.2.54). The first two equations are quasi-stationary relations, i.e. time-independent, for the pressure and the velocity. The last two are time-evolution equations for the temperature of the solid and the gas. We apply the same discretisation method as we did for the tube in Section 4.1. The governing equations for the regenerator with non-ideal gas are (3.4.32), (3.4.33), (3.4.35), (3.4.36) and (3.4.37). The first four equations are discretised in the same way as in the ideal gas case, but because of the non-linearity of the non-dimensional Van der Waals equation (3.4.35), we employ a predictor-corrector method to solve the system of equations iteratively.

4.2.1   One-dimensional regenerator discretisation with ideal gas

We introduce computational grids $\{z_j = j\triangle h, j = 0, ..., N_z, h = \hat{L}_r/N_z\}$ and $\{t^n = n\triangle t^n, n = 0, ..., N_t\}$ where $\hat{L}_r$ is the dimensionless length of the regenerator. Denote by u_j^n the gas velocity, by p_j^n the pressure, by $T_{g,j}^n$ the gas temperature and by $T_{r,j}^n$ the material temperature at the grid point (z_j, t^n). We assume that the conductivity and heat capacity for the regenerator material are constant, i.e. $(\hat{k}_r = 1)$ and $(\hat{c}_r = 1)$ in this section; in Section 4.2.2 they depend on temperature. We use the θ-method for the discretisation of the time derivative in (3.2.49) governing T_r. The result for the interior points is

$$T_{r,0}^{n+1} = T_H, \qquad T_{r,N_x}^{n+1} = T_C$$

$$T_{r_j}^{n+1} - \triangle t^n \theta \left(\beta_r^*(T_{g,j}^{n+1} - T_{r,j}^{n+1}) + \frac{1}{Pe_r} \frac{T_{r,j-1}^{n+1} - 2T_{r,j}^{n+1} + T_{r,j+1}^{n+1}}{h^2} \right) =$$

$$T_{r_j}^n + (1-\theta)\triangle t^n \left(\beta_r^*(T_{g_j}^n - T_{r_j}^n) + \frac{1}{Pe_r} \frac{T_{r_{j-1}}^n - 2T_{r_j}^n + T_{r_{j+1}}^n}{h^2} \right)$$

$$\text{for} \quad j = 1, ..., N_z - 1, \quad n = 0, ..., N_t - 1. \tag{4.2.1}$$

The discretisation of (3.2.54) for T_g is explained now. If $u_j^n > 0$, we use the following scheme for the temperature equation

$$T_{g,j}^{n+1} - \triangle t^n \theta \left(b_2 \frac{T_{g,j}^n}{p_j^n} \frac{T_{g,j-1}^{n+1} - 2T_{g,j}^{n+1} + T_{g,j+1}^{n+1}}{h^2} + \frac{\gamma \beta_g^*}{\mathcal{B}} \frac{T_{g,j}^n}{p_j^n}(T_{r,j}^{n+1} - T_{g,j}^{n+1}) + (1-\gamma)T_{g,j}^{n+1} \frac{u_{j+1}^n - u_{j-1}^n}{2h} \right)$$

$$= T_{g,j}^n + (1-\theta)\triangle t^n \left(b_2 \frac{T_{g,j}^n}{p_j^n} \frac{T_{g,j-1}^n - 2T_{g,j}^n + T_{g,j+1}^n}{h^2} + \frac{\gamma \beta_g^*}{\mathcal{B}} \frac{T_{g,j}^n}{p_j^n}(T_{r,j}^n - T_{g,j}^n) + (1-\gamma)T_{g,j}^n \frac{u_{j+1}^n - u_{j-1}^n}{2h} \right)$$

$$- c_j^n \left(1 + \frac{1}{2}(1 - c_j^n) \left(\frac{\Phi_{j+\frac{1}{2}}^n}{r_{j+\frac{1}{2}}^n} - \Phi_{j-\frac{1}{2}}^n \right) \right) (T_{g_j}^n - T_{g_{j-1}}^n),$$

$$j = 2, ..., N_z - 2, \quad n = 0, ..., N_t - 1. \tag{4.2.2}$$

If $u_j^n < 0$, then

$$T_{g,j}^{n+1} - \triangle t^n \theta \left(b_2 \frac{T_{g,j}^n}{p_j^n} \frac{T_{g,j-1}^{n+1} - 2T_{g,j}^{n+1} + T_{g,j+1}^{n+1}}{h^2} + \frac{\gamma \beta_g^*}{\mathcal{B}} \frac{T_{g,j}^n}{p_j^n} (T_{r,j}^{n+1} - T_{g,j}^{n+1}) + (1-\gamma) T_{g,j}^{n+1} \frac{u_{j+1}^n - u_{j-1}^n}{2h} \right)$$

$$= T_{g,j}^n + (1-\theta)\triangle t^n \left(b_2 \frac{T_{g,j}^n}{p_j^n} \frac{T_{g,j-1}^n - 2T_{g,j}^n + T_{g,j+1}^n}{h^2} + \frac{\gamma \beta_g^*}{\mathcal{B}} \frac{T_{g,j}^n}{p_j^n} (T_{r,j}^n - T_{g,j}^n) + (1-\gamma) T_{g,j}^n \frac{u_{j+1}^n - u_{j-1}^n}{2h} \right)$$

$$-c_j^n \left(1 - \frac{1}{2}(1+c_j^n) \left(\Phi_{j+\frac{1}{2}}^n - \frac{\Phi_{j-\frac{1}{2}}^n}{r_{j-\frac{1}{2}}^n} \right) \right) (T_{g_{j+1}}^n - T_{g_j}^n)$$

$$j = 2, ..., N_z - 2, \qquad n = 0, ..., N_t - 1,$$

(4.2.3)

where c_j^n is the Courant number, $c_j^n := \triangle t^n u_j^n / \triangle z$, and $\triangle t^n$ is the adaptive time step. For $j = 1, N_z - 1$ the convection term (the last term in (3.2.54)) discretisation is taken to be upwind, which is of first-order accuracy ($\Phi^n = 0$). The ratio $r_{j+\frac{1}{2}}^n$ and the Van Leer flux limiter are defined by the relations (4.1.4) and (4.1.5), respectively. The boundary conditions (3.2.75) and (3.2.76) are discretised by (with $T_{r,0}^{n+1} = T_{AC}$ and $T_{r,N_z}^{n+1} = T_C$)

$$T_{g,0}^{n+1} - \triangle t^n \theta \left(\frac{\gamma \beta_g^*}{\mathcal{B}} \frac{T_{g,0}^n}{p_0^n} (T_H - T_{g,0}^{n+1}) + (1-\gamma) T_{g,0}^{n+1} (\frac{-3u_0^n + 4u_1^n - u_2^n}{2h}) \right) =$$

$$T_{g,0}^n + (1-\theta)\triangle t^n \left(\frac{\gamma \beta_g^*}{\mathcal{B}} \frac{T_{g,0}^n}{p_0^n} (T_H - T_{g,0}^n) + (1-\gamma) T_{g,0}^n (\frac{-3u_0^n + 4u_1^n - u_2^n}{2h}) \right) - c_0^n (T_{g,1}^n - T_{g,0}^n),$$

(4.2.4)

$$T_{g,N_z}^{n+1} - \triangle t^n \theta \left(\frac{\gamma \beta_g^*}{\mathcal{B}} \frac{T_{g,N_z}^n}{p_{N_z}^n} (T_C - T_{g,N_z}^{n+1}) + (1-\gamma) T_{g,N_z}^{n+1} (\frac{3u_{N_z}^n - 4u_{N_z-1}^n + u_{N_z-2}^n}{2h}) \right) =$$

$$T_{g,N_z}^n + (1-\theta)\triangle t^n \left(\frac{\gamma \beta_g^*}{\mathcal{B}} \frac{T_{g,N_z}^n}{p_{N_z}^n} (T_C - T_{g,N_z}^n) + (1-\gamma) T_{g,N_z}^n (\frac{3u_{N_z}^n - 4u_{N_z-1}^n + u_{N_z-2}^n}{2h}) \right)$$

$$-c_{N_z}^n (T_{g,N_z}^n - T_{g,N_z-1}^n).$$

(4.2.5)

The velocity equation (3.2.53) is discretised using a one-sided second-order formulation for the velocity gradient, a second-order central difference for the temperature term and a one-sided second-order formulation for the pressure time-derivative with boundary condition at $j = N_z$ defined by (3.2.73), as (conductivity is assumed to be constant $\hat{k}_g = 1$)

$$u_{r,N_z}^{n+1} = \left(\frac{A_t}{A_r \phi} \frac{T_{g,r_{N_z}}^{n+1}}{T_{g,t_0}^{n+1}} \right) u_{t,0}^{n+1}, \qquad\qquad j = N_z,$$

$$u_{N_z-1}^{n+1} - 4u_{N_z-2}^{n+1} + 3u_{N_z-3}^{n+1} = \frac{2b_1}{hp_{N_x-1}^n} (T_{g,N_z}^{n+1} - 2T_{g,N_z-1}^{n+1} + T_{g,N_z-2}^{n+1})$$

$$+ \frac{\beta_g^*}{\mathcal{B}p_{N_x-1}^{n+1}} (T_{r,N_z-1}^{n+1} - T_{g,N_z-1}^{n+1}) - \frac{h}{\gamma p_{N_x-1}^n} (\frac{3p_{N_z-1}^{n+1} - 4p_{N_z-1}^n + p_{N_z-1}^{n-1}}{2\triangle t^n}), \qquad j = N_z - 1,$$

$$-3u_j^{n+1} + 4u_{j+1}^{n+1} - u_{j+2}^{n+1} = \frac{2b_1}{hp_j^n} (T_{g,j+1}^{n+1} - 2T_{g,j}^{n+1} + T_{g,j-1}^{n+1})$$

$$+ \frac{\beta_g^*}{\mathcal{B}p_j^{n+1}} (T_{r,j}^{n+1} - T_{g,j}^{n+1}) - \frac{h}{\gamma p_j^n} (\frac{3p_j^{n+1} - 4p_j^n + p_j^{n-1}}{\triangle t^n}), \qquad j = 0, ..., N_z - 2,$$

(4.2.6)

for every time level $n = 0, 1, 2, 3, ... N_t - 1$. The pressure equation (3.2.47) is discretised by a one-sided second-order formulation as (viscosity is assumed to be constant $\hat{\mu} = 1$)

$$
\begin{aligned}
p_0^{n+1} &= p_c^{n+1}, & j &= 0, \\
-3p_1^{n+1} + 4p_2^{n+1} - p_3^{n+1} &= 2h(\mathcal{D}u_1^{n+1}), & j &= 1, \\
3p_j^{n+1} - 4p_{j-1}^{n+1} + p_{j-2}^{n+1} &= 2h(\mathcal{D}u_j^{n+1}), & j &= 2, ..., N_z,
\end{aligned}
\tag{4.2.7}
$$

where p_c^{n+1} is the pressure at the compressor side, which is assumed to be given.

4.2.2   One-dimensional regenerator discretisation with real gas

We rearrange the dimensionless form of the equation of state (3.4.35) into a third-degree polynomial in ρ_g

$$
\mathcal{MBN}\rho_g^3 - \mathcal{MB}\rho_g^2 + (p\mathcal{BN} + T_g)\rho_g - p\mathcal{B} = 0.
\tag{4.2.8}
$$

We apply Newton's method to find the density at each discretised point in the regenerator with old values of p, the pressure in the regenerator, which is not uniform in space, and T_g. The algorithm of the iteration method will be explained later on in this section. We then solve the equation (3.4.37) for the gas temperature T_g in the regenerator simultaneously with equation (3.4.33) for the solid temperature T_r with just computed values for the density and using old data for the velocity, material properties (k_g, k_r, c_g, c_r) and second term of enthalpy H_p. For the interior points the result for (3.4.37) is

$$
\begin{aligned}
&T_{g,j}^{n+1} - \triangle t^n \theta \frac{1}{\rho_{g,j}^{n+1}} \Big(\frac{\gamma(1 - \mathcal{N}\rho_{g,j}^{n+1})}{\gamma c_{g,j}^n(1 - \mathcal{N}\rho_{g,j}^{n+1}) - (\gamma - 1)(1 - \rho_{g,j}^{n+1}H_{p,j}^n)} \Big) \\
&\qquad \left(\frac{k_{g,j}^n}{Pe_g} \Big(\frac{T_{g,j+1}^{n+1} - 2T_{g,j}^{n+1} + T_{g,j-1}^{n+1}}{h^2} \Big) + \mathcal{E}(T_{r,j}^{n+1} - T_{g,j}^{n+1}) \right) \\
&= T_{g,j}^n + (1 - \theta)\triangle t^n \frac{1}{\rho_{g,j}^{n+1}} \Big(\frac{\gamma(1 - \mathcal{N}\rho_{g,j}^{n+1})}{\gamma c_{g,j}^n(1 - \mathcal{N}\rho_{g,j}^{n+1}) - (\gamma - 1)(1 - \rho_{g,j}^{n+1}H_{p,j}^n)} \Big) \\
&\qquad \left(\frac{k_{g,j}^n}{Pe_g} \Big(\frac{T_{g,j+1}^n - 2T_{g,j}^n + T_{g,j-1}^n}{h^2} \Big) + \mathcal{E}(T_{r,j}^n - T_{g,j}^n) \right) \\
&\quad - \Big[\frac{(\gamma - 1)(1 - \rho_{g,j}^{n+1}H_{p,j}^n)[T_{g,j}^n - 2\mathcal{MB}\rho_{g,j}^{n+1}(1 - \mathcal{N}\rho_{g,j}^{n+1})^2]}{(1 - \mathcal{N}\rho_{g,j}^{n+1})[c_{g,j}^n(1 - \mathcal{N}\rho_{g,j}^{n+1}) - (\gamma - 1)(1 - \rho_{g,j}^{n+1}H_{p,j}^n)]} \Big] \Big(\frac{u_{j+1}^n - u_{j-1}^n}{h^2} \Big) \\
&\qquad - c_j^n \left(1 + \frac{1}{2}(1 - c_j^n) \left(\frac{\Phi_{j+\frac{1}{2}}^n}{r_{j+\frac{1}{2}}^n} - \Phi_{j-\frac{1}{2}}^n \right) \right) (T_{g,j}^n - T_{g,j-1}^n) \\
&\qquad j = 2, ..., N_z - 2, \quad n = 0, ..., N_t - 1.
\end{aligned}
\tag{4.2.9}
$$

Equation (3.4.33) is discretised in the same way as for the ideal gas (4.2.1). The pressure equation (3.4.32) is discretised the same as equation (4.2.7). The velocity equation (3.4.36) is discretised using a one-sided second-order formulation for the velocity gradient, the second-order central difference scheme for the diffusion term and a one-sided second-order formulation for the pressure time-derivative. This yields

$$
u^{n+1}_{r,N_z} = \left(\frac{A_t}{A_r \phi} \frac{\rho^{n+1}_{g,t_0}}{\rho^{n+1}_{g,r_{N_z}}} \right) u^{n+1}_{t,0}, \qquad\qquad j = N_z,
$$

$$
u^{n+1}_{N_z-1} - 4u^{n+1}_{N_z-2} + 3u^{n+1}_{N_z-3} = \frac{2hk^n_{g,N_z-1}}{\left(\frac{T^n_{g,N_z-1}}{B(1-\mathcal{N}\rho^n_{g,N_z-1})^2} - 2\mathcal{M}\rho^n_{g,N_z-1} \right)\mathcal{B}c^n_{g,N_z-1}\rho^n_{g,N_z-1}(1-\mathcal{N}\rho^n_{g,N_z-1})}
$$

$$
\left(\mathcal{E}(T^{n+1}_{r,N_z} - T^{n+1}_{g,N_z}) + \frac{1}{Pe_g} \frac{T^{n+1}_{g,N_z} - 2T^{n+1}_{g,N_z-1} + T^{n+1}_{g,N_z-2}}{h^2} \right)
$$

$$
- \frac{2h}{\rho^n_{g,N_z-1}\left(\frac{T^n_{g,N_z-1}}{B(1-\mathcal{N}\rho^n_{g,N_z-1})^2} - 2\mathcal{M}\rho^n_{g,N_z-1} \right)} \left(1 - \frac{(\gamma-1)(1-\rho^n_{g,N_z-1}H^n_{p,N_z-1})}{\gamma c^n_{g,N_z-1}(1-\mathcal{N}\rho^n_{g,N_z-1})} \right)
$$

$$
\left[\frac{3p^{n+1}_{N_z-1} - 4p^n_{N_z-1} + p^{n-1}_{N_z-1}}{2\Delta t} \right].
$$

$$
j = N_z - 1,
$$

$$
-3u^{n+1}_j + 4u^{n+1}_{j+1} - u^{n+1}_{j+2} =
$$

$$
\frac{2hk^n_{g,j}}{\left(\frac{T^n_{g,j}}{B(1-\mathcal{N}\rho^n_{g,j})^2} - 2\mathcal{M}\rho^n_{g,j} \right)\mathcal{B}c^n_{g,j}\rho^n_{g,j}(1-\mathcal{N}\rho^n_{g,j})} \left(\mathcal{E}(T^{n+1}_{r,j} - T^{n+1}_{g,j}) + \frac{1}{Pe_g} \frac{T^{n+1}_{g,j+1} - 2T^{n+1}_{g,j} + T^{n+1}_{g,j-1}}{h^2} \right)
$$

$$
- \frac{2h}{\rho^n_{g,j}\left(\frac{T^n_{g,j}}{B(1-\mathcal{N}\rho^n_{g,j})^2} - 2\mathcal{M}\rho^n_{g,j} \right)} \left(1 - \frac{(\gamma-1)(1-\rho^n_{g,j}H^n_{p,j})}{\gamma c^n_{g,j}(1-\mathcal{N}\rho^n_{g,j})} \right) \frac{3p^{n+1}_j - 4p^n_j + p^{n-1}_j}{2\Delta t}.
$$

$$
j = 0, ..., N_z - 2.
$$

$$
(4.2.10)
$$

The five equations (4.2.1), (4.2.7), (4.2.8), (4.2.9) and (4.2.10) for the five variables ρ_g, u, T_r, T_g, p are solved by the prediction-correction algorithm given below.

Algorithm 4.4 (Prediction-correction algorithm)
Step 1: (Prediction)
Solve the density equation (4.2.8) using Newton's method and initial guess by old density in the entire domain, with old data for the gas temperature and pressure as

$$
\mathcal{MBN}\tilde{\rho_g}^3 - \mathcal{MB}\tilde{\rho_g}^2 + (p^n\mathcal{BN} + T^n_g)\tilde{\rho_g} - p^n\mathcal{B} = 0.
$$

Step 2.
Solve (4.2.1), (4.2.7), (4.2.9) and (4.2.10) with corresponding boundary conditions simul-

taneously to obtain $\tilde{p}, \tilde{T}_r, \tilde{u}$ and $\tilde{T}_g$ with density computed in step 1

$$\frac{\partial \tilde{p}}{\partial x} = -D\tilde{u},$$

$$c_r^n \frac{\partial \tilde{T}_r}{\partial t} = \mathcal{E}\mathcal{F}(\tilde{T}_g - \tilde{T}_r) + \frac{k_r^n}{Pe_r} \frac{\partial^2 \tilde{T}_r}{\partial x^2},$$

$$\frac{\partial \tilde{u}}{\partial x} = \frac{1}{\left(\frac{T_g^n}{B(1-\mathcal{N}\tilde{\rho_g})^2} - 2\mathcal{M}\tilde{\rho_g}\right)\mathcal{B}c_g^n\tilde{\rho_g}(1-\mathcal{N}\tilde{p})}[\mathcal{E}(\tilde{T}_r - \tilde{T}_g) + \frac{1}{Pe_g}\frac{\partial^2 \tilde{T}_g}{\partial x^2}]$$

$$-\frac{1}{\tilde{\rho_g}\left(\frac{T_g^n}{B(1-\mathcal{N}\tilde{\rho_g})^2} - 2\mathcal{M}\tilde{\rho_g}\right)}[1 - \frac{(\gamma-1)(1-\tilde{\rho}H_p^n)}{\gamma c_g^n(1-\mathcal{N}\tilde{\rho_g})}]\frac{D\tilde{p}}{Dt},$$

$$\frac{D\tilde{T}_g}{Dt} = \frac{1}{\tilde{\rho_g}}\left(\frac{\gamma(1-\mathcal{N}\tilde{\rho_g})}{\gamma c_g^n(1-\mathcal{N}\tilde{\rho_g}) - (\gamma-1)(1-\tilde{\rho_g}H_p^n)}\right)[\mathcal{E}(\tilde{T}_r - \tilde{T}_g) + \frac{1}{Pe_g}\frac{\partial^2 \tilde{T}_g}{\partial x^2}]$$

$$-[\frac{(\gamma-1)(1-\tilde{\rho_g}H_p^n)[T_g^n - 2\mathcal{M}\mathcal{B}\tilde{\rho_g}](1-\mathcal{N}\tilde{\rho_g})^2}{(1-\mathcal{N}\tilde{\rho_g})[\gamma c_g^n(1-\mathcal{N}\tilde{\rho_g}) - (\gamma-1)(1-\tilde{\rho_g}H_p^n)]}]\frac{\partial \tilde{u}}{\partial x}.$$

Step 3: (Correction)
Solve the density equation with predicted data $\tilde{T}_g$ and $\tilde{p}$ for the gas temperature and the pressure from

$$\mathcal{M}\mathcal{B}\mathcal{N}(\rho_g^{n+1})^3 - \mathcal{M}\mathcal{B}(\rho_g^{n+1})^2 + (\tilde{p}\mathcal{B}\mathcal{N} + \tilde{T}_g)\tilde{\rho_g}^{n+1} - \tilde{p}\mathcal{B} = 0.$$

Step 4.
Solve (4.2.1), (4.2.7), (4.2.9) and (4.2.10) again to obtain the corrected solution

$$\frac{\partial p^{n+1}}{\partial x} = -Du^{n+1},$$

$$\tilde{c}_r \frac{\partial T_r^{n+1}}{\partial t} = \mathcal{E}\mathcal{F}(T_g^{n+1} - T_r^{n+1}) + \frac{\tilde{k}_r}{Pe_r}\frac{\partial^2 T_r^{n+1}}{\partial x^2},$$

$$\frac{\partial u^{n+1}}{\partial x} = \frac{1}{\left(\frac{\tilde{T}_g}{B(1-\mathcal{N}\rho_g^{n+1})^2} - 2\mathcal{M}\rho_g^{n+1}\right)\mathcal{B}\tilde{c}_g\rho_g^{n+1}(1-\mathcal{N}\rho_g^{n+1})}[\mathcal{E}(T_r^{n+1} - T_g^{n+1}) + \frac{1}{Pe_g}\frac{\partial^2 T_g^{n+1}}{\partial x^2}]$$

$$-\frac{1}{\rho_g^{n+1}\left(\frac{\tilde{T}_g}{B(1-\mathcal{N}\rho_g^{n+1})^2} - 2\mathcal{M}\rho_g^{n+1}\right)}[1 - \frac{(\gamma-1)(1-\rho_g^{n+1}\tilde{H}_p)}{\gamma\tilde{c}_g(1-\mathcal{N}\rho_g^{n+1})}]\frac{Dp^{n+1}}{Dt},$$

$$\frac{DT_g^{n+1}}{Dt} = \frac{1}{\rho_g^{n+1}}\left(\frac{\gamma(1-\mathcal{N}\rho_g^{n+1})}{\mathcal{B}\tilde{c}_g(1-\mathcal{N}\rho_g^{n+1}) - (\gamma-1)(1-\rho_g^{n+1}\tilde{H}_p)}\right)[\mathcal{E}(T_r^{n+1} - T_g^{n+1}) + \frac{1}{Pe_g}\frac{\partial^2 T_g^{n+1}}{\partial x^2}]$$

$$-[\frac{(\gamma-1)(1-\rho_g^{n+1}\tilde{H}_p)[T_g^n - 2\mathcal{M}\mathcal{B}\rho_g^{n+1}](1-\mathcal{N}\rho^{n+1})^2}{(1-\mathcal{N}\rho_g^{n+1})[\gamma\tilde{c}_g(1-\mathcal{N}\rho_g^{n+1}) - (\gamma-1)(1-\rho_g^{n+1}H_p^n)]}]\frac{\partial u^{n+1}}{\partial x}.$$

■

4.3 Tube-regenerator coupling

To couple the two main parts of the system, the pulse-tube and the regenerator, we need to apply the interface conditions (3.2.73) for ideal gas or (3.4.40) for non-ideal gas

together with (3.2.71) in the case of the single-stage PTR. In the case of multi-stage PTR the interface conditions are (3.5.3), (3.5.6) for ideal gas, and (3.5.7), (3.5.8) for non-ideal gas, together with (3.5.1) for the pressure continuity at the junction. The iterative methods used to solve the governing equations for the pulse-tube and the regenerator, also include updating the interface and junction conditions. In this section we show various strategies for coupling the 1D regenerator and the 1D pulse-tube, the 1D regenerator and the 2D pulse-tube, and finally the coupling in multi-stage PTR where two regenerators and one pulse-tube are connected.

4.3.1   Coupling the 1D pulse-tube with the 1D regenerator

For ideal gas and non-ideal gas we can solve the problem numerically in a similar way. It turns out that after time discretisation we can decouple the temperature equations from the flow equations. Let the temperature vectors at time t^n be denoted by $(\theta_{g_r}^T, \theta_r^T, \theta_{g_t}^T)^T$, where θ_{g_r} is the vector of gas temperatures in the regenerator, θ_r is the vector of regenerator material temperature and θ_{g_t} is the vector of gas temperature in the tube at the discretised points. Denote, the corresponding source terms in the equations by $(\zeta_1^T, \zeta_2^T, \zeta_3^T)^T$, then the temperature at time t^{n+1} typically satisfies an equation like

$$\begin{bmatrix} \mathbf{A} & \mathbf{B} & \mathbf{C} \\ \mathbf{D} & \mathbf{E} & \\ \mathbf{F} & & \mathbf{G} \end{bmatrix}^n \begin{bmatrix} \theta_{g_r} \\ \theta_r \\ \theta_{g_t} \end{bmatrix}^{n+1} = \begin{bmatrix} \zeta_1 \\ \zeta_2 \\ \zeta_3 \end{bmatrix}^n . \tag{4.3.1}$$

The blocks $\mathbf{A}$, $\mathbf{E}$ and $\mathbf{G}$ are three-diagonal matrices, $\mathbf{B}$ and $\mathbf{D}$ are one-diagonal matrices representing the coupling in the regenerator of the gas and the solid material, and $\mathbf{C}$ and $\mathbf{F}$ represent the coupling between the gas temperature in the tube and in the regenerator at the interface. The first grid point of the tube is coupled with the last grid point of the regenerator. Of course, if we assume a pre-assigned fixed temperature for the CHX at the interface, the blocks $\mathbf{C}$ and $\mathbf{F}$ become vectors of zeros.

The global system of temperature equations for a three-stage PTR without by-pass takes the form

$$\begin{bmatrix} \mathbf{A}_1 & \mathbf{B}_1 & \mathbf{C}_1 & \mathbf{H} & & & & & \\ \mathbf{D}_1 & \mathbf{E}_1 & & & & & & & \\ \mathbf{F}_1 & & \mathbf{G}_1 & & & & & & \\ \mathbf{J} & & \mathbf{K} & \mathbf{A}_2 & \mathbf{B}_2 & \mathbf{C}_2 & \mathbf{L} & & \\ & & & \mathbf{D}_2 & \mathbf{E}_2 & & & & \\ & & & \mathbf{F}_2 & & \mathbf{G}_2 & & & \\ & & & \mathbf{M} & & \mathbf{N} & \mathbf{A}_3 & \mathbf{B}_3 & \mathbf{C}_3 \\ & & & & & & \mathbf{D}_3 & \mathbf{E}_3 & \\ & & & & & & \mathbf{F}_3 & & \mathbf{G}_3 \end{bmatrix}^n \begin{bmatrix} \theta_{g,r1} \\ \theta_{r1} \\ \theta_{g,t1} \\ \theta_{g,r2} \\ \theta_{r2} \\ \theta_{g,t2} \\ \theta_{g,r3} \\ \theta_{r3} \\ \theta_{g,t3} \end{bmatrix}^{n+1} = \begin{bmatrix} \zeta_{11} \\ \zeta_{12} \\ \zeta_{13} \\ \zeta_{21} \\ \zeta_{22} \\ \zeta_{23} \\ \zeta_{31} \\ \zeta_{32} \\ \zeta_{33} \end{bmatrix}^n \tag{4.3.2}$$

The first index refers to the stage. The global coupling blocks $\mathbf{H}$, $\mathbf{J}$, $\mathbf{K}$, $\mathbf{L}$, $\mathbf{M}$, $\mathbf{N}$ for the temperature in the three-stage PTR represent the discretised form of (3.5.3) in the case of ideal gas and (3.5.8) in the case of non-ideal gas. In the case of ideal gas $\mathbf{H}$ is $\mathbf{0}$ since

in discretised form (3.5.3) reads

$$T_{(g,r1,N_{z1})}^{n+1} = \left(\frac{T_{(g,r2,0)}^n T_{(t1,0)}^n}{u_{(r2,0)}^n (A\phi)_{r2} T_{(t1,0)}^n + u_{(t1,0)}^n A_{t1} T_{(g,r2,0)}^n} \right) u_{(r1,N_{z1})}^n (A\phi)_{r1}. \quad (4.3.3)$$

It is a block of zeros. For real gas (3.5.8) maintains T_{g,r_2} at the new time level,

$$\left[\rho_{(g,N_{z1})}^{n+1} u_{N_{z1}}^n \phi A \left(c_{(g,N_{z1})}^n T_{(g,N_{z1})}^{n+1} + \frac{1}{M} H_{(p,N_{z1})}^n P^n \right) \right]_{r1}$$

$$= \left[\rho_{(g,0)}^{n+1} u_0^n \phi A \left(c_{(g,0)}^n T_{(g,0)}^{n+1} + \frac{1}{M} H_{(p,0)}^n P^n \right) \right]_{r2} \quad (4.3.4)$$

$$+ \left[\rho_{(g,0)}^{n+1} u_0^n A \left(c_{(g,0)}^n T_{(g,0)}^{n+1} + \frac{1}{M} H_{(p,0)}^n P^n \right) \right]_{t1}.$$

The other global blocks consist of zeros with the only non-zero component arising from discretising (3.5.3) or (3.5.8). If we assume pre-assigned fixed temperatures for the CHXs at the junctions, the blocks **H**, **J**, **K**, **L**, **M** and **N** become vectors of zeros. This means that the temperature equations are completely decoupled.
The discretised equations for the gas velocities and pressures are combined in

$$\begin{bmatrix} P & Q & R \\ S & V & \\ & W & X \end{bmatrix}^n \begin{bmatrix} u_r \\ p \\ u_t \end{bmatrix}^{n+1} = \begin{bmatrix} \eta_1 \\ \eta_2 \\ \eta_3 \end{bmatrix}^n. \quad (4.3.5)$$

Here $\mathbf{u}_r$ is the velocity vector of unknowns for the regenerator, $\mathbf{p}_r$ is the pressure vector of unknowns for the regenerator and $\mathbf{u}_t$ is the velocity vector of unknowns for the pulse-tube. The blocks **P**, **V** and **X** are three-diagonal matrices for discretisation of $\mathbf{u}_r$, $\mathbf{p}$ and $\mathbf{u}_t$ in the interior points. The blocks **Q** and **S** represent the coupling between the velocity and the pressure in the regenerator, the block **R** represents the coupling between the velocities in the last point of the regenerator and the first point of the tube consisting of zeros with the only non-zero component coming from the discretised formulation of (3.2.73) for ideal gas

$$u_{r,N_z}^{n+1} = \left(\frac{A_t}{\phi A_r} \frac{T_{N_z,r}^{n+1}}{T_{0,t}^{n+1}} \right) u_{0,t}^{n+1}. \quad (4.3.6)$$

In the case of non-ideal gas the discretised form of (3.4.40) is

$$u_{r,N_z}^{n+1} = \left(\frac{\rho_{(g,t,0)}^{n+1} A_t}{\rho_{(g,r,N_z)}^{n+1} A_r \phi} \right) u_{0,t}^{n+1}. \quad (4.3.7)$$

The block **W** represents the pressure continuity at the interface between the regenerator and the tube (3.2.71).
The global system of discretised formulations for the velocities and pressures of the

three-stage PTR takes the form

$$
\begin{bmatrix}
\mathbf{P}_1 & \mathbf{Q}_1 & \mathbf{R}_1 & \mathbf{M}_1 & & & & & & \\
\mathbf{S}_1 & \mathbf{V}_1 & \mathbf{O} & \mathbf{O} & & & & & & \\
\mathbf{M}_2 & \mathbf{W}_1 & \mathbf{X}_1 & \mathbf{M}_3 & & & & & & \\
\mathbf{M}_4 & \mathbf{O} & \mathbf{M}_5 & \mathbf{P}_2 & \mathbf{Q}_2 & \mathbf{R}_2 & \mathbf{M}_6 & & & \\
& \mathbf{N}_1 & \mathbf{O} & \mathbf{S}_2 & \mathbf{V}_2 & \mathbf{O} & \mathbf{O} & & & \\
& & & \mathbf{M}_7 & \mathbf{W}_2 & \mathbf{X}_2 & \mathbf{M}_8 & & & \\
& & & \mathbf{M}_9 & \mathbf{O} & \mathbf{M}_{10} & \mathbf{P}_3 & \mathbf{Q}_3 & \mathbf{R}_3 & \\
& & & & \mathbf{N}_2 & \mathbf{O} & \mathbf{S}_3 & \mathbf{V}_3 & \mathbf{O} & \\
& & & & & & & & \mathbf{W}_3 & \mathbf{X}_3
\end{bmatrix}^{n}
\begin{bmatrix}
\mathbf{u}_{r1} \\
\mathbf{p}_1 \\
\mathbf{u}_{t1} \\
\mathbf{u}_{r2} \\
\mathbf{p}_2 \\
\mathbf{u}_{t2} \\
\mathbf{u}_{r3} \\
\mathbf{p}_3 \\
\mathbf{u}_{t3}
\end{bmatrix}^{n+1}
=
\begin{bmatrix}
\eta_{11} \\
\eta_{12} \\
\eta_{13} \\
\eta_{21} \\
\eta_{22} \\
\eta_{23} \\
\eta_{31} \\
\eta_{32} \\
\eta_{33}
\end{bmatrix}^{n} ,
$$

$$(4.3.8)$$

where the blocks $\mathbf{N}_1$ and $\mathbf{N}_2$ represent pressure continuity, and the blocks $\mathbf{M}_1$-$\mathbf{M}_{10}$ represent the coupling of the velocities in the tubes and the regenerators at the junctions. Such couplings come from the discretised form of (3.5.6) for ideal gas, which at the junction I is the following

$$
u_{r1,N_{z1}}^{n+1} (\phi A)_{r1} = u_{r2,0}^{n+1} (\phi A)_{r2} + u_{t1,0}^{n+1} A_{t1}, \tag{4.3.9}
$$

or the the discretised form of (3.5.7) for real gas

$$
\rho_{(g,r1,N_{z1})}^{n+1} u_{(r1,N_{z1})}^{n+1} (A\phi)_{r1} = \rho_{(g,r2,0)}^{n+1} u_{(r2,0)}^{n+1} (A\phi)_{r2} + \rho_{(g,t1,0)}^{n+1} u_{(t1,0)}^{n+1} A_{t1}. \tag{4.3.10}
$$

Now we have two systems of algebraic equations (4.3.1) and (4.3.5) for a single-stage PTR with the size of $(3N_z \times 3N_z)$, and two systems of algebraic equations (4.3.2) and (4.3.8) for a three-stage PTR with the size of $([2(N_{z1} + N_{z2} + N_{z3}) + N_{t1} + N_{t2} + N_{t3}] \times [2(N_{z1} + N_{z2} + N_{z3}) + N_{t1} + N_{t2} + N_{t3}])$, where N_{z1}, N_{z2}, N_{z3} are the number of grid points in the regenerators 1,2,3 and N_{t1}, N_{t2}, N_{t3} are the number of grid points in the tubes 1,2,3.

The system of governing PDEs has turned into systems of algebraic equations by discretisation in space and time. We have two linear systems of algebraic equations, $A^1 X^1 = b^1$ for the temperature and $A^2 X^2 = b^2$ for the velocity and pressure, where their sizes depend on the number of stages and the computational grids used. The algorithm of the numerical solution for each time step $t^{n+1} = t^n + \Delta t$ is summarized as follows.

Algorithm 4.5
Step 1: (Initialisation)
Choose an initial vector for $(\theta_{g_r}(t_0), \theta_r(t_0), \theta_{g_t}(t_0))^\mathsf{T}$ in (4.3.1) and $(\mathbf{u}_r(t_0), \mathbf{p}(t_0), \mathbf{u}_t(t_0))^\mathsf{T}$ in (4.3.5).
Step 2:
We solve the first system $A^1 X^1 = b^1$ with old data for the velocity and pressure to predict the temperatures at t^{n+1}.
Step 3:
We solve the second system $A^2 X^2 = b^2$ using the just computed temperatures to find new values for the velocities and pressure at t^{n+1}.

Step 4:
We repeat step 1 using the new values of the velocities and pressure and update the temperatures until a predefined tolerance is reached for the estimated error. ∎

In the case of non-ideal gas, there is an internal iteration loop described in Sections 4.1.3 and 4.2.2, which updates all variables via a predictor-corrector algorithm. Therefore the above mentioned iteration algorithm can be combined with this predictor-corrector algorithm to update not only the internal point values but also the interface values.

4.3.2   Coupling the 2D pulse-tube with the 1D regenerator (ideal gas)

At the interface of the regenerator and the pulse-tube there are three conditions to be satisfied: pressure continuity, conservation of mass and conservation of energy as described in Chapter 3. In PTR simulation we assume ideal heat exchangers, in the sense that we assign a constant temperature in the heat-exchanger at the cold end. This means that when the flow exits from the heat exchanger we replace the energy conservation condition by $T_g = $ constant (given). In the coupling of 2D pulse-tube to 1D regenerator we apply the discretised mass conservation (4.3.6) such that the gas velocity at the tube side is computed by cross-sectionally averaging of the axial velocity (3.3.34) as

$$u_{t,0}^{n+1} = \frac{1}{r_0^2} \sum_{j=0}^{N_r-1} (u_{0,j}^{n+1} + u_{0,j+1}^{n+1}) r_j \Delta r. \tag{4.3.11}$$

The thermodynamic pressure in the pulse-tube is only a function of time. To find this pressure at each time level together with imposing (4.3.6) for the gas velocity in the regenerator, we apply an iterative method with the following steps:

Algorithm 4.6
Step 1:
Solve the temperature equations (4.1.9) or (4.1.10) for the 2D tube, and (4.2.1), (4.2.2) or (4.2.3) for the 1D regenerator.
Step 2: (Initial guess)
Solve simultaneously the one-dimensional momentum equations in the pulse-tube and the regenerator (4.3.5) to find p_0, $P(t)$ and u. The values at the interface are taken as initial guess for the iteration loop below.
Step 3: (Iteration loop)

   i. Solve the velocity and pressure equations (4.2.6) and (4.2.7) in the regenerator to find the predicted value for the pressure at the cold end, $P(L_r, t)$.

   ii. Use the pressure calculated in *i* at the interface as the thermodynamic pressure in the pulse-tube.

iii. Apply the pressure-correction algorithm (4.1.18), (4.1.19), (4.1.36), (4.1.32), (4.1.33) and (4.1.34) to find u^*, v^*, q, u^{n+1}, v^{n+1} and p^{n+1} in the 2D pulse-tube.

iv. Compute the cross-sectionally averaged axial velocity at the cold end of the pulse tube (4.3.11). Use equation (4.3.6) as the boundary condition for the velocity $u^{new}_{(r,N_z)}$ at the cold end of the regenerator.

v. Compute the velocity change at the cold end of the regenerator

$$u_{diff} = u^{new}_{(r,N_z)} - u^{old}_{(r,N_z)}.$$ (4.3.12)

vi. If $|u_{diff}|$ is less than a predefined tolerance then go to the next time-step, otherwise go back to step *"i"* with $u^{new}_{(r,N_z)}$ as the new boundary condition for the regenerator velocity in (4.2.6).
Loop end. ∎

4.4   2-D code implementation and validation

The discretised formulae described in this section are implemented in C++ and coded together with PETSc (Portable, Extensible Toolkit for Scientific Computation) [63], which is a suite of data structures and routines for the scalable solution of scientific applications modeled by partial differential equations. In order to assess the code performance a number of standard fluid dynamics problems have been simulated. The chosen examples are Hagen-Poiseuille flow which demonstrates the pressure-correction Algorithm 4.2, then fluid in a pipe subjected to an oscillating pressure gradient which represents the oscillatory behaviour of the gas in the pulse tube, and finally the Graetz problem dealing with heat transfer being a test for the temperature distribution computation by (4.1.9) or (4.1.10).

4.4.1   Hagen-Poiseuille flow in a circular tube

Consider a steady laminar viscous and incompressible flow through a tube with constant circular cross-section. The tube is significantly longer than its diameter. The fully developed flow is called *Hagen-Poiseuille flow* because it was first investigated by Hagen (1839) and Poiseuille (1840). If the length of the tube is long enough, the radial component of the flow (3.3.3) is negligible away from the tube's entrance. Consequently the axial velocity gradient, $\partial u/\partial z$, will be zero according to the continuity equation for incompressible flow. This analysis gives us an important result which relates the pressure gradient to the axial shear stress (3.3.2) (neglecting τ_{zz})

$$\frac{\partial p}{\partial z} = \mu \frac{1}{r} \frac{\partial}{\partial r} \left(r \frac{\partial u}{\partial r} \right).$$ (4.4.1)
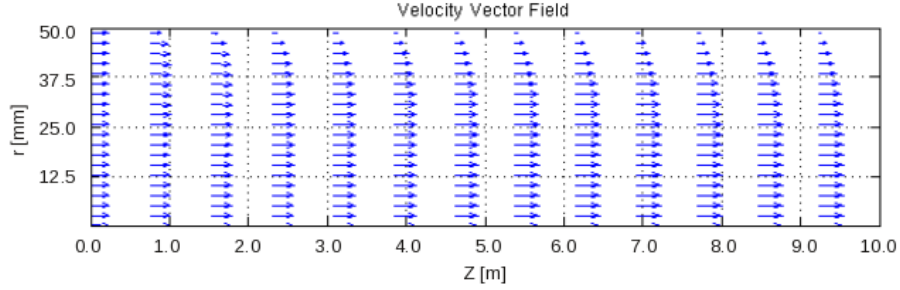
Figure 4.1: The axial velocity field at $t = 1$ s for Hagen flow problem.

We can solve this equation analytically by integrating (4.4.1) with proper boundary conditions: $u = 0$ at the wall ($r = r_0$) and zero velocity gradient at the centre line ($r = 0$), i.e. the symmetry requires $\partial u / \partial r = 0$. The analytical solution reads

$$u(r) = \frac{1}{4\mu} \frac{\partial p}{\partial z} (r^2 - r_0^2). \tag{4.4.2}$$

The maximum velocity, $u(0) = u_{max}$, occurs at the centre line and the average cross-sectional velocity is $u_{av} = u_{max}/2$. The pressure gradient is proportional to the viscosity and the maximum velocity

$$\frac{\partial p}{\partial z} = -\frac{4\mu}{r_0^2} u_{max}. \tag{4.4.3}$$

The pressure gradient is a constant quantity in steady flow. Substitution of (4.4.3) into (4.4.2) gives

$$u(r) = u_{max}(1 - r^2/r_0^2). \tag{4.4.4}$$

This analytical solution is now used to validate our numerical method (the pressure-correction algorithm) for the 2D pulse-tube. We consider the momentum equations in the axial and radial directions and the continuity equation for an incompressible flow (3.3.1), (3.3.2), (3.3.3)

$$\rho \left(\frac{\partial u}{\partial t} + u \frac{\partial u}{\partial z} + v \frac{\partial u}{\partial r} \right) = -\frac{\partial p}{\partial z} + \mu \left(\frac{1}{r} \frac{\partial u}{\partial r} + \frac{\partial^2 u}{\partial r^2} \right), \tag{4.4.5a}$$

$$\rho \left(\frac{\partial v}{\partial t} + u \frac{\partial v}{\partial z} + v \frac{\partial v}{\partial r} \right) = -\frac{\partial p}{\partial r} + \mu \left(\frac{1}{r} \frac{\partial v}{\partial r} + \frac{\partial^2 v}{\partial r^2} - \frac{v}{r^2} \right), \tag{4.4.5b}$$

$$\frac{\partial u}{\partial z} + \frac{\partial v}{\partial r} + \frac{v}{r} = 0. \tag{4.4.5c}$$

The problem is solved numerically with Algorithm 4.2. Then we choose the following parameters: length of tube $L = 10$[m], diameter $D = 2r_0 = 0.1$[m], viscosity $\mu = 2.5 \times$

$10^{-3}[\text{kg.m}^{-1}.\text{s}^{-1}]$, density $\rho = 10^3[\text{kg.m}^{-3}]$ and the inflow velocity $u_{av} = 5[\text{cm.s}^{-1}]$. The Reynolds number is $Re = D\rho u_{av}/\mu = 2000 < 2500$ so that the flow is laminar. The following initial and boundary conditions are taken

$$\text{inflow:} \qquad u(0,r,t) = u_{av}, \qquad u(0,r_0,t) = 0, \qquad v(0,r,t) = 0, \qquad (4.4.6a)$$

$$\text{outflow:} \qquad\qquad\qquad\qquad v(L,r,t) = 0, \qquad p(L,r,t) = 0, \qquad (4.4.6b)$$

$$\text{tube wall:} \qquad\qquad\qquad u(z,r_0,t) = 0, \qquad v(z,r_0,t) = 0, \qquad (4.4.6c)$$

$$\text{symmetry line:} \qquad v(z,0,t) = 0, \qquad \frac{\partial u(z,0,t)}{\partial r} = 0, \qquad \frac{\partial p(z,0,t)}{\partial r} = 0, \qquad (4.4.6d)$$

$$\text{initial conditions:} \qquad u(z,r,0) = u_{av}, \qquad v(z,r,0) = 0, \qquad p(z,r,0) = 0. \qquad (4.4.6e)$$

If we use the non-dimensionalisation procedure (3.2.11), we get the following non-dimensional equations for (4.4.5) (omitting the hats)

$$\frac{\partial u}{\partial t} + u\frac{\partial u}{\partial z} + v\frac{\partial u}{\partial r} = -\frac{\partial p}{\partial z} + \frac{1}{Re}\left(\frac{1}{r}\frac{\partial u}{\partial r} + \frac{\partial^2 u}{\partial r^2}\right), \qquad (4.4.7a)$$

$$\frac{\partial v}{\partial t} + u\frac{\partial v}{\partial z} + v\frac{\partial v}{\partial r} = -\frac{\partial p}{\partial r} + \frac{1}{Re}\left(\frac{1}{r}\frac{\partial v}{\partial r} + \frac{\partial^2 v}{\partial r^2} - \frac{v}{r^2}\right), \qquad (4.4.7b)$$

$$\frac{\partial u}{\partial z} + \frac{\partial v}{\partial r} + \frac{v}{r} = 0, \qquad (4.4.7c)$$

where Re is the oscillatory Reynolds number. Solving the problem by Algorithm (4.2) gives the velocity vector field shown in Figure 4.1. The initial uniform profile will evolve to a parabolic profile. At the entrance the non-zero values of the radial velocity are not visible. The radial velocity becomes zero along the pipe when the flow profile gets fully developed. The parabolic shape of the axial velocity is most visible at the developed part of the flow at $z = L$. In Figure 4.2 the axial velocity distribution at $t = 1000$ s is displayed. It takes about 20 times the tube diameter before the flow is fully developed. In Table 4.1 the numerical results obtained for different grids are shown. The L_∞ error is a measure for the difference between the numerical solution at the end of the tube (developed part of the flow, $z = L$) and the analytical solution (4.4.4) defined by $\|\epsilon\|_\infty = \|u_{exact} - u_{num}\|_\infty = \max_j(u_{exact} - u_{num}) = u_{exact}(r = r_0) - u_{num}(r = r_0)$. Apparently we have first-order convergence as expected, see Algorithm 4.2 in Section 4.1.3.

4.4.2 Pipe flow subject to an oscillating pressure gradient

Consider an unsteady laminar incompressible flow in a circular pipe that experiences an oscillatory pressure gradient. The flow is assumed to be independent of the axial
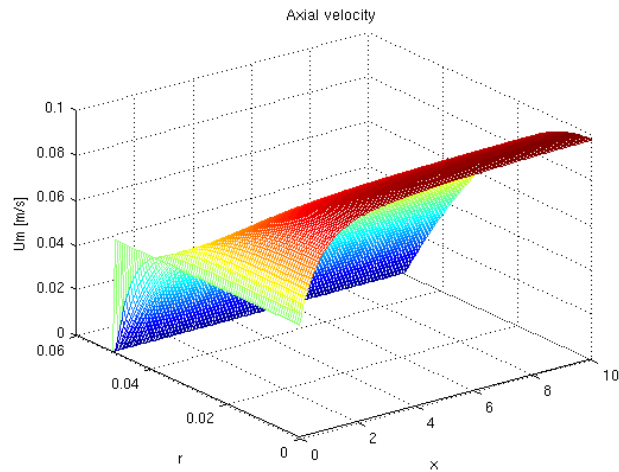
Figure 4.2: The axial velocity profile for the Hagen-Poiseuille flow at t = 1000 s.

$N_z \times N_r$	N_t	$\Delta\hat{z}$	$\Delta\hat{r}$	$\Delta\hat{t}$	error
50×25	9600	2.0	2×10^{-2}	2×10^{-2}	4.17×10^{-3}
100×50	19600	1.0	1×10^{-2}	1×10^{-2}	2.33×10^{-3}
200×100	39600	0.5	5×10^{-3}	5×10^{-3}	1.41×10^{-3}
400×200	79600	0.25	2.5×10^{-3}	2.5×10^{-3}	0.78×10^{-3}
800×400	159600	0.125	1.25×10^{-3}	1.25×10^{-3}	0.40×10^{-3}

Table 4.1: The error at $z = L$ and t = 1000 [sec] found with different grids for the Hagen-Poiseuille flow problem.

coordinate, so that the radial velocity is zero. The equation of motion then takes the form

$$\frac{\partial u}{\partial t} = -\frac{1}{\rho}\frac{\partial p}{\partial z} + \nu[\frac{\partial^2 u}{\partial r^2} + \frac{1}{r}\frac{\partial u}{\partial r}], \qquad (4.4.8)$$

where ν is the kinematic viscosity. The axial pressure gradient is defined as a sinusoidal function of time by

$$\frac{\partial p}{\partial z} = -\rho K \cos(\omega t),$$

where $K[m.s^{-2}]$ is a constant and ω is the angular frequency. We now non-dimensionalise (4.4.8) with the following variables

$$u = \bar{u}\hat{u}, r = r_0\hat{r}, t = \frac{1}{\omega}\hat{t}, p = \bar{\rho}\bar{u}^2\hat{p}.$$

The equation (4.4.8) will then take the following dimensionless form (omitting hats)

$$\frac{\partial u}{\partial t} = \frac{K}{\bar{u}\omega}\cos(t) + \frac{1}{Re_\omega}[\frac{\partial^2 u}{\partial r^2} + \frac{1}{r}\frac{\partial u}{\partial r}], \qquad (4.4.9)$$

with the boundary conditions

$$u(z, r_0) = 0, \quad \frac{\partial u}{\partial r}(z, 0) = 0. \qquad (4.4.10)$$

Here Re_ω is the so-called *kinematic Reynolds number* defined as $Re_\omega := r_0^2\omega/\nu$. The analytical solution found by cf. [31], [32] and [61] and discussed by [77] is ($Re_\omega > 4$)

$$u(r, t) = \mathcal{Re}\left\{\frac{K}{i\omega}e^{i\omega t}[1 - \frac{J_0(r\sqrt{-i\omega/\nu})}{J_0(R_0\sqrt{-i\omega/\nu})}]\right\}, \qquad (4.4.11)$$

where $\mathcal{Re}$ denotes the real part of the solution and J_0 is a Bessel function of the first kind and zero order. To have a kinematic Reynolds number in the range of laminar flow, we take a sample problem with parameter values (water is the fluid) $L = 1.0[m], r_0 = 2.5[mm], \bar{u} = 1[m/s], \nu = 10^{-6}[m^2.s^{-1}], K = 10[m.s^{-2}], \omega = 40\pi[s^{-1}]$; the kinematic Reynolds number is then $Re_\omega = 785$ with $\bar{u}\sqrt{2/(\omega\nu)} = 126$ and $2r_0/\sqrt{2\nu/\omega} = 39.7$. We see from Figure 3.2 that our reciprocating flow is in the perturbed laminar region. The numerical simulation is using the second-order central difference formula for the first and the second spatial derivatives of the axial velocity in (4.4.9) implicitly. In Figure 4.3 we see the steady oscillatory results of our simulation during one full pressure cycle. For better visualisation reason the dimensions have been scaled up. Note: the steady state is independent of the initial situation. There is a high activity region close to the wall that has a phase lag of almost $\pi/2$ with the pressure cycle. This effect is characteristic for oscillating flow at high frequencies, and it is called *Richardson's annular effect*. Figure 4.4 shows the radial variation of the axial velocity at $z = L/2$ [m] at t = 4.0125 [s] obtained numerically and analytically (4.4.11). Figure 4.4.a and 4.4.b show the velocity profiles in the case of very low-frequency and low-frequency oscillation, $fr = 0.01$ [Hz] and $fr = 1$ [Hz], respectively. Figure 4.4.c displays the velocity profile for high-frequency with fr = 20 [Hz]. The numerical and analytical solutions are in perfect agreement. The numerical errors obtained with different grids are shown in Table 4.2 where

(a) $\hat{t} = \pi/2$

(b) $\hat{t} = \pi$

(c) $\hat{t} = 3\pi/2$

(d) $\hat{t} = 2\pi$
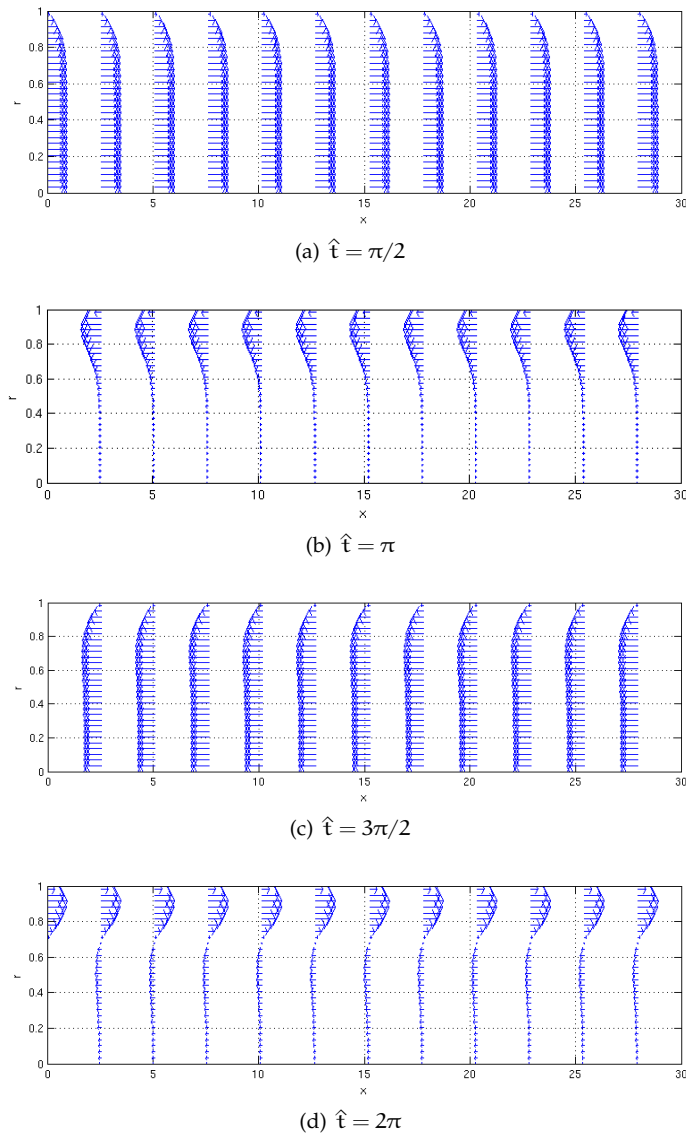
Figure 4.3: Velocity fields at different time steps for oscillating flow problem (fr = 20 [Hz]).

(a) $fr = 0.01\,\mathrm{Hz}$, $t = 100\,\mathrm{s}$

(b) $fr = 1\,\mathrm{Hz}$, $t = 10\,\mathrm{s}$

(c) $fr = 20\,\mathrm{Hz}$, $t = 4.0125\,\mathrm{s}$
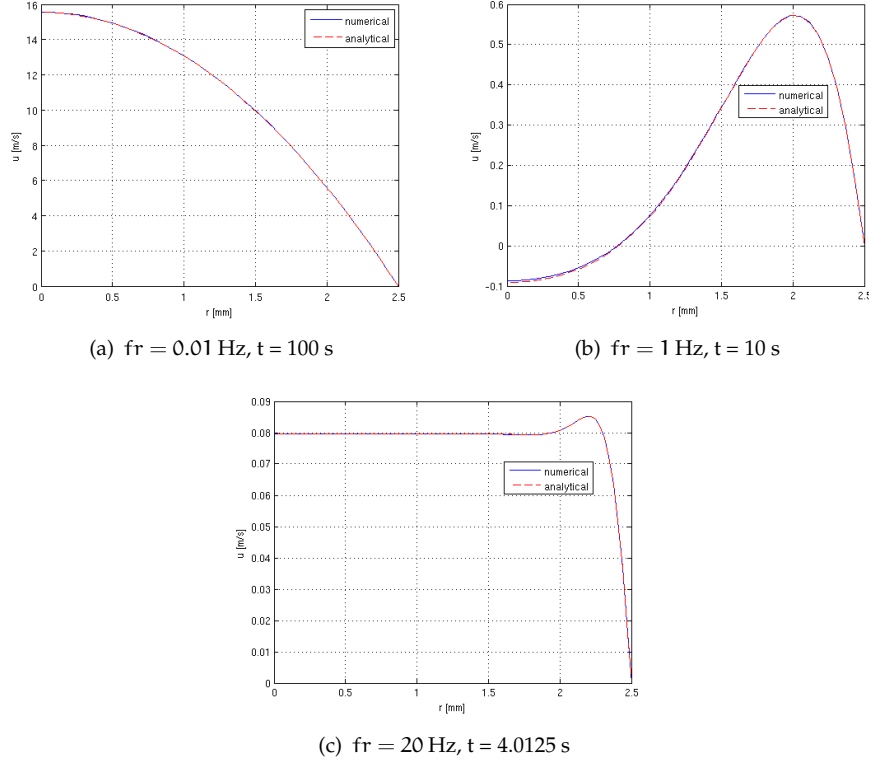
Figure 4.4: The radial variation of the axial velocity at $z = L/2$; numerical solution (solid line) and analytical solution (dashed line).

the L_∞-norm of the errors computed as the difference between the numerical results and the analytical solution of the axial velocity profile (4.4.11) as $\|\epsilon\|_\infty = \|u_{\mathrm{exact}} - u_{\mathrm{num}}\|_\infty$. Second-order convergence is achieved as it confirms the second-order discretisation method applied to the velocity equation (4.4.9).

4.4.3 Temperature distribution in fully developed pipe flow

Finally we test our code with respect to temperature distribution in the *Graetz problem*. Consider the following convection-conduction equation for the temperature

$$\rho c_p u(r)\frac{\partial T}{\partial z} = k_g \frac{\partial}{\partial r}(r\frac{\partial T}{\partial r}),\tag{4.4.12}$$

where $u(r)$ is the steady velocity profile given by the Hagen-Poiseuille

$$u(r) = 2u_{av}(1 - (\frac{r}{r_0})^2).\tag{4.4.13}$$

$N_z \times N_r$	N_t	$\Delta \hat{z}$	$\Delta \hat{r}$	$\Delta \hat{t}$	error
61×31	9580	20	0.05	0.05	2.63×10^{-3}
121×61	19664	10	0.025	0.025	5.92×10^{-4}
241×121	39833	5	0.0125	0.0125	1.42×10^{-4}

Table 4.2: The error in the axial velocity of the oscillatory flow problem at $z = L/2$ and $t = 4.0125$ [s].

Here u_{av} is the mean velocity in a fully developed laminar tube flow where r_0 is the radius of the tube. The solution can be expressed as a series, cf. [40]

$$T(z, r) = 1 - 1.477 e^{-3.658(1/Pe)z} R_0(r) + 0.81 e^{-22.178(1/Pe)z} R_1(r)$$
$$-0.385 e^{-53.05(1/Pe)z} R_2(r) + ... \tag{4.4.14}$$

For the functions $R_0(r), R_1(r), R_2(r)$ we use the form given in [21], Table 22-1. We note that on the central axis $R_0(0) = R_1(0) = R_2(0) = ... = 1$.

We solve the equation (4.4.12) by taking it in unsteady and dimensionless form (omitting hats),

$$\frac{\partial T}{\partial t} = -u(r) \frac{\partial T}{\partial z} + \frac{1}{Pe} \left(\frac{1}{r} \frac{\partial T}{\partial r} + \frac{\partial^2 T}{\partial r^2} \right), \quad \text{where} \quad Pe = \frac{\rho c_p u_{av} r_0}{k_g}. \tag{4.4.15}$$

The following dimensionless initial and boundary conditions are imposed

$$T(0, r) = T_0 = 0, \tag{4.4.16}$$
$$T(z, r_0) = T_w = 1,$$
$$\frac{\partial T}{\partial r}(z, 0) = 0.$$

We take the following dimensionless parameters in our test problem: length of tube $L = 30$, radius of tube $r_0 = 1$, mean velocity $u_{av} = 1$, the Peclet number $Pe = 60$. We use the same numerical method as we do for the pulse-tube in Chapter 5 and 6, i.e. θ-method in time with $\theta = 0.5 + \Delta t$, central difference for the first and second radial derivatives
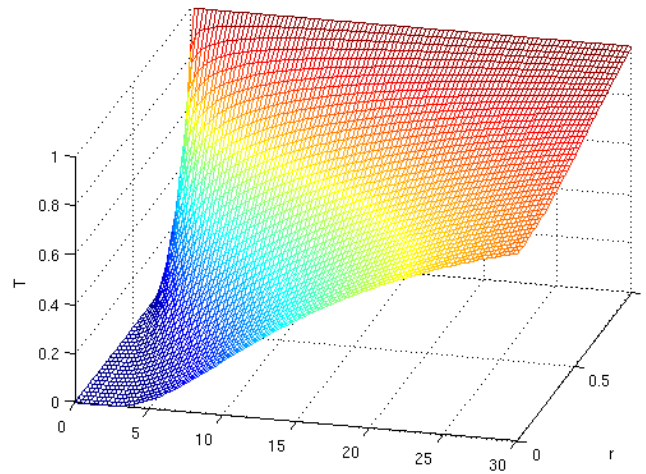
Figure 4.5: Steady-state numerical solution of the temperature in the Graetz problem.
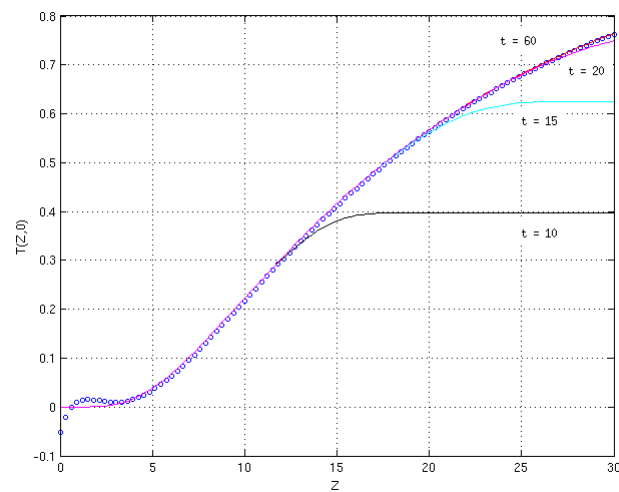
Figure 4.6: The dimensionless temperatures at the central axis in the Graetz problem at different times compared with the steady-state analytical solution (dots)).

$N_z \times N_r$	N_t	$\Delta\hat{z}$	$\Delta\hat{r}$	$\Delta\hat{t}$	error
25×10	1080	1.2	0.1	0.05	2.2×10^{-2}
50×20	2280	0.6	0.05	0.025	5.3×10^{-3}
100×40	4680	0.3	0.025	0.0125	1.05×10^{-3}

Table 4.3: The numerical errors on the central axis in the Graetz problem.

of the temperature and a second-order high-resolution method for the convection term. The unsteady problem is solved until the steady state. Figure 4.5 shows the steady temperature distribution. The unsteady temperatures distribution at the central axis are shown in Figure 4.6 at different non-dimensional times $t = 10, t = 15, t = 20, t = 60$. As observed, the numerical steady state is in good agreement with the analytical solution except at the central axis and small distance away from it. Of course, the numerical results are correct in respect with $T(0,0) = 0$, but the analytical solution (4.4.14) needs more terms of the series to reach the assigned BC at the inflow. The numerical errors, obtained with different grids and calculated away from the inflow ($z \geq 3$), are shown in Table 4.3. The errors are computed as the difference between the numerical results on the central axis and the analytical solution (4.4.14) at dimensionless time $\hat{t} = 60$ as $\|\epsilon\|_\infty = \|T_{\text{exact}} - T_{\text{num}}\|_\infty$. Second-order convergence is approximately achieved as expected

4.5   Domain decomposition

There has been a great deal of interest in adaptive local mesh refinement procedures for solving steady and time-dependent unsteady partial differential equations. Such techniques are used to calculate solutions for prescribed levels of accuracy. If the solution is behaving smoothly in the majority of the domain, but move fast in some other area a uniform grid is far from optimal. Therefore we need fine grids in regions where the solution changes rapidly, i.e. in the high-activity regions, and coarse in regions where it varies slowly, i.e. in low-activity regions. One choice is to use separate uniform grids (with different grid sizes) on different parts of the domain. The mesh size in each grid is chosen in such a way that a globally required accuracy is achieved. This approach can be even more computationally efficient when combined with *domain decomposition*. Here the storage of data and computations can be done with smaller systems than in the case of an entirely uniform grid. We only need to deal with a structured A-matrix which

has big advantages compared with tensor grids. This domain decomposition (DD) approach can also be used with adaptive local mesh refinement. There are two main categories for adaptive methods, *moving-grid*(or dynamic-regridding) methods and *static-regridding* methods. When the high-activity region is changing its spatial position during computations, the dynamic-regridding domain decomposition is needed. Adaptive local mesh refinement methods have been used for different problems on stationary and non-stationary partial differential equations, i.e. elliptic equations [26], [33], parabolic equations [27], [70] and hyperbolic equations [2], [6].

We now discuss a domain decomposition method that can be applied to either non-uniform stationary or moving meshes to solve vector systems of partial differential equations of the form

$$u_t + f(x, y, t, u, u_x, u_y) = \left[D^1(x, y, t, u) u_x \right]_x + \left[D^2(x, y, t, u) u_y \right]_y ,$$

$$\text{for} \qquad t > 0, (x, y) \in \Omega \qquad (4.5.1)$$

with initial conditions

$$u(x, y, 0) = u_0(x, y) \qquad \text{for} \qquad (x, y) \in \Omega \cup \partial\Omega \qquad (4.5.2)$$

with suitable well-posed boundary conditions on $\partial\Omega$. We apply our computations in two space dimensions on rectangular regions Ω, as is the case for the pulse-tube in two-dimensional cylindrical coordinates. The boundary layer close to the wall in the pulse-tube is rather crucial. In addition the regions at the hot and cold ends have high activity too. Therefore we have three high-activity regions that are dealt with by static-regridding.

4.5.1 A test problem

We demonstrate the static-regridding domain-decomposition method by applying it to the problem of *"flow subject to an oscillating pressure gradient"* presented in Section 4.4.2. This problem has some similarity with the pulse-tube problem as it has a boundary layer close to tube wall. The governing equation (4.4.9) for the velocity profile reads

$$\frac{\partial u}{\partial t} = \frac{K}{\bar{u}\omega} \cos(t) + \frac{1}{Re_\omega} [\frac{\partial^2 u}{\partial r^2} + \frac{1}{r} \frac{\partial u}{\partial r}],$$

with the boundary conditions (4.4.10). We take the same parameter values as before, i.e. $L = 1.0[m], r_0 = 2.5[mm], \nu = 10^{-6}[m^2.s^{-1}], K = 10[m.s^{-2}], \omega = 40\pi[s^{-1}]$; the kinematic Reynolds number is then $Re_\omega = 785$. As it can be seen from the velocity profiles in Figures 4.4.a,b the variations in the boundary layer are high in the high-frequency problem than in the low-frequency one. In high-frequency oscillatory problems, we have a high-activity region with a certain width near the wall, and for the rest of the domain the solution behaves smoothly. To optimise the number of fine grid points, we need to find the location and the size of the high activity regions. We refine the grid in the high activity regions and we keep the rest of the domain as coarse as possible to still satisfy for the desired global error. This error is calculated by the difference between

the analytical solution (4.4.11) and the numerical domain decomposition solution as $\|\epsilon\|_\infty = \|u_{exact} - u_{num}\|_\infty$. In this example we take uniform grid with ($N_z \times N_r = 241 \times 61$) to consider the discrete approximation of the radial gradient of the axial velocity in the domain at various radial positions of the domain as (see Figure 4.7)

$$\frac{\partial u}{\partial r}. \tag{4.5.3}$$

Here (Fig.4.4) the thickness of the high-activity layer is about one quarter of the pipe radius. In the rest of the domain $\partial u/\partial r$ is close to zero.
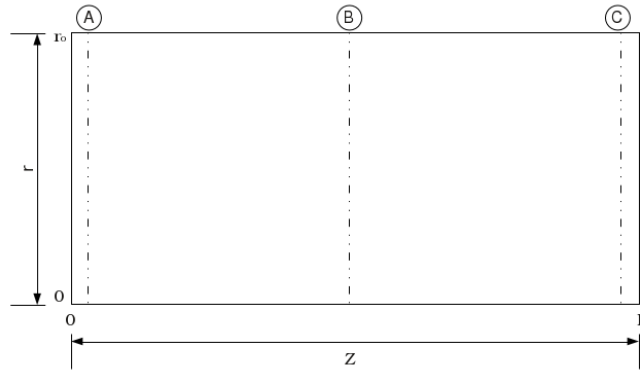
Figure 4.7: View lines in the radial direction for detecting width of the boundary layers at three axial positions A,B and C.

4.5.2   DD method

We use a global uniform coarse grid with ($N_z \times N_r$) points and with step size $\Delta z = L/(N_z - 1)$ and $\Delta r = r_0/(N_r - 1)$

$$\Omega^{\Delta r}_{[0,L] \times [0,r_0]} = \{(z_i, r_j), i = 1, ..., N_z, j = 1, ..., N_r\}. \tag{4.5.4}$$

Suppose we refine the r-grid on a typical interval $[a, b]$. In Figure 4.8, $b = r_0$ indicates the wall boundary. The points a and b are always grid points of the coarse grid. The fine grid has ($N_z \times N_b$) points and step size $\delta r = (b - a)/(N_b - 1)$.

$$\Omega^{\delta r}_{[0,L] \times [a,b]} = \{(z_i, r_j), i = 1, ..., N_z, j = 1, ..., N_b\}. \tag{4.5.5}$$

Define the *refinement factor* as

$$f := \frac{N_b - 1}{N_r - N_0}.$$

In Figure 4.8 the refinement factor $f = 2$. We proceed with the following steps to advance the solution from t^n to t^{n+1} with time step Δt.
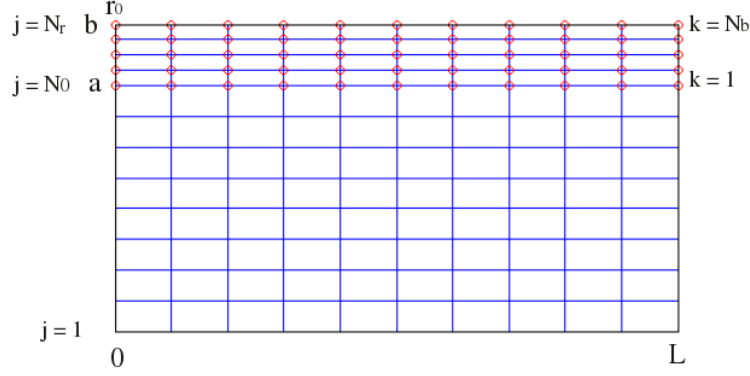
Figure 4.8: Fine and coarse grids for an axisymmetrical domain with refinement factor $f = 2$.

Algorithm 5.1
Step 1: (*Coarse grid solution*)
Discretising (4.4.9) using second-order differences implicitly gives

$$U_{i,j}^{n+1} = U_{i,j}^n + \Delta t\theta \left\{ \frac{K}{\bar{u}\omega}\cos(t^{n+1}) + \frac{1}{Re_\omega}[\frac{U_{i,j+1}^{n+1} - 2U_{i,j}^{n+1} + U_{i,j-1}^{n+1}}{\Delta r^2} + \frac{1}{r_{i,j}}\frac{U_{i,j+1}^{n+1} - U_{i,j-1}^{n+1}}{2\Delta r}] \right\}$$

$$+ \Delta t(1-\theta)\left\{ \frac{K}{\bar{u}\omega}\cos(t^n) + \frac{1}{Re_\omega}[\frac{U_{i,j+1}^n - 2U_{i,j}^n + U_{i,j-1}^n}{\Delta r^2} + \frac{1}{r_{i,j}}\frac{U_{i,j+1}^n - U_{i,j-1}^n}{2\Delta r}] \right\}$$

$$i = 1, 2, ..., N_z, \quad j = 2, 3, ..., N_r - 1$$

$$\frac{\partial U^{n+1}}{\partial r}(z, 0) = 0, \quad U_{i,N_r}^{n+1} = 0.$$

$$(4.5.6)$$

where $U_{i,j}^{n+1}$ denotes the solution of the coarse grid and $\theta = 0.5 + \Delta t$. The solutions U^{n+1} for $r = a$ and $r = b$ are used to define the initial boundary value problem as Dirichlet boundary conditions on the fine grid.
Step 2: (*Interpolation*)
The time step for the fine grid is $\delta t = \Delta t/f$. To proceed the fine grid solution we need to update the fine grid boundary condition provided by the coarse grid at each time level $t^n + \delta t$. These Dirichlet boundary conditions at the points $\{(z_i, a), (z_i, b); \quad i = 1, ..., N_z\}$ are found by interpolation of the old U^n and new U^{n+1} coarse grid values. For instance, if $\delta t = \frac{1}{2}\Delta t$ we proceed the computations two times on the fine grid with δt and $U^{n+\frac{1}{2}} = (U^{n+1} + U^n)/2$.
Step 3: (*Fine grid solution*)

We advance the solution on the fine grid f times for discretised (4.4.9)

$$u_{i,j}^{n+\frac{1}{2}} = u_{i,j}^n + \delta t\theta_0 \left\{ \frac{K}{\bar{u}\omega} \cos(t^{n+\frac{1}{2}}) + \frac{1}{Re_\omega}[\frac{u_{i,j+1}^{n+\frac{1}{2}} - 2u_{i,j}^{n+\frac{1}{2}} + u_{i,j-1}^{n+\frac{1}{2}}}{\delta r^2} + \frac{1}{r_{i,j}} \frac{u_{i,j+1}^{n+\frac{1}{2}} - u_{i,j-1}^{n+\frac{1}{2}}}{2\delta r}] \right\}$$

$$+ \Delta t(1 - \theta_0) \left\{ \frac{K}{\bar{u}\omega} \cos(t^n) + \frac{1}{Re_\omega}[\frac{u_{i,j+1}^n - 2u_{i,j}^n + u_{i,j-1}^n}{\delta r^2} + \frac{1}{r_{i,j}} \frac{u_{i,j+1}^n - u_{i,j-1}^n}{2\delta r}] \right\}$$

$$i = 1, 2, ..., N_z, \quad j = 2, 3, ..., N_b - 1$$

$$u_{i,1}^{n+\frac{1}{2}} = U_{i,N_0}^{n+\frac{1}{2}}, \quad u_{i,N_b}^{n+\frac{1}{2}} = U_{i,N_r}^{n+\frac{1}{2}},$$

$$(4.5.7)$$

$$u_{i,j}^{n+1} = u_{i,j}^{n+\frac{1}{2}} + \delta t\theta_0 \left\{ \frac{K}{\bar{u}\omega} \cos(t^{n+1}) + \frac{1}{Re_\omega}[\frac{u_{i,j+1}^{n+1} - 2u_{i,j}^{n+1} + u_{i,j-1}^{n+1}}{\delta r^2} + \frac{1}{r_{i,j}} \frac{u_{i,j+1}^{n+1} - u_{i,j-1}^{n+1}}{2\delta r}] \right\}$$

$$+ \Delta t(1 - \theta_0) \left\{ \frac{K}{\bar{u}\omega} \cos(t^{n+\frac{1}{2}}) + \frac{1}{Re_\omega}[\frac{u_{i,j+1}^{n+\frac{1}{2}} - 2u_{i,j}^{n+\frac{1}{2}} + u_{i,j-1}^{n+\frac{1}{2}}}{\delta r^2} + \frac{1}{r_{i,j}} \frac{u_{i,j+1}^{n+\frac{1}{2}} - u_{i,j-1}^{n+\frac{1}{2}}}{2\delta r}] \right\}$$

$$i = 1, 2, ..., N_z, \quad j = 2, 3, ..., N_b - 1$$

$$u_{i,1}^{n+1} = U_{i,N_0}^{n+1}, \quad u_{i,N_b}^{n+1} = U_{i,N_r}^{n+1},$$

$$(4.5.8)$$

where $\theta_0 = 0.5 + \delta t$.

Step 4: (Composite solution)
We have computed two series of values for points of the global coarse grid that lie within the local fine grid. We then make a composite solution combining the fine grid solution at these points and the coarse grid solution elsewhere as

$$u_{i,j}^{n+1}(\text{comp}) = \begin{cases} u_{(i,f(j-1)+1)}^{n+1} & i = 1, ..., N_z; \quad j = 1, ..., (N_b - 1)/f + 1 \\ \\ U_{i,j}^{n+1} & \text{otherwise} \end{cases}$$

$$(4.5.9)$$

■

4.5.3   Computational efficiency

We assume that the coarse grid prediction provides accurate enough boundary values for the fine grid. In the local defect correction method we have to iterate on these results. However, in evolution problems like those herein the iterations can be omitted, see [53]. The efficiency of the DD method is indicated by the *complexity*, i.e. the number of flops (floating points operations). Typically we need $\sim O(n^2)$ flops for solving a sparse $n \times n$ matrix A. In our approach we have two grids: a coarse grid with radial dimension r_0 (dimensionless value of tube radius) and a fine grid with dimension $(b - a)$ (dimensionless value). See Figure 4.8. Thus we need to solve a matrix of dimension $(N_z \times N_r)$ for the coarse grid and thus with complexity $O(N_z \times N_r)^2$, as well as a matrix of dimension

$(N_z \times N_b)$ for the fine grid with complexity $O(N_z \times N_b)^2$. The number of fine grid points is given by

$$N_b = N_r \times (\frac{b - a}{r_0})f.$$

where N_b should be rounded. To assess the computational gain by our domain decomposition technique we now define the *gain factor* (*gf*) as the ratio between number of operations for the uniform grid and for the DD grid for one time step Δt as

$$gf = \frac{\text{complexity for uniform grid}}{\text{complexity for DD}}. \tag{4.5.10}$$

Thus we have

- uniform grid:
    - core grid: $(N_z \times fN_r)$
    - flops: $f(N_z \times fN_r)^2$
- DD grid:
    - coarse grid: $(N_z \times N_r)$
    - fine grid: $(N_z \times N_r(\frac{b-a}{r_0})f)$
    - flops: $(N_z \times N_r)^2 + f(N_z \times N_r(\frac{b-a}{r_0})f)^2$

Then the gain factor (4.5.10) becomes

$$gf = \frac{f^3}{1 + f^3(\frac{b-a}{r_0})^2} \approx f^3 \quad \text{if} \quad \frac{b-a}{r_0} \ll \frac{1}{f^3}. \tag{4.5.11}$$

Say if $(b - a)/r_0 = 1/10$, we see a gain factor of about f^3. The gain factor approaches 1 if the layer width is large.

Remark: We may choose tensor grid, where the dense part is in high-activity layer, whenever the variation in the layer is too sharp, but here we do not do this.

Table 4.4 shows the domain decomposition errors in the velocity $\|\epsilon\|_\infty = \|u_{exact} - u_{DD}\|_\infty$ at $t = 4.0124$ (s) of the flow, due to an oscillating pressure gradient, for two different grids with various number of refinements. Here $(b - a)/r_0 = 0.25$. The error has been computed at one view line in the middle of the tube (line B in Figure 4.7).

In Figure 4.9 we can see the velocity profile at $t = 4.0125$ [s] obtained by the Domain Decomposition method. The solution has smooth behaviour in the core of the domain and has sharp variation at the boundary layer where the grid has been refined.

4.6 Conclusion

We solved the governing equations by proper numerical methods. Since the domain of computation in 1D and 2D is of simple shape, a finite difference (FD) method is an appropriate way to discretise the equations. In addition, a domain-decomposition method

f	gf	$(N_z \times N_r) = (61 \times 11)$ $N_r(\frac{b-a}{r_0})f$	$\|\epsilon\|_\infty$	$(N_z \times N_r) = (61 \times 21)$ $N_r(\frac{b-a}{r_0})f$	$\|\epsilon\|_\infty$
2	5.33	6	2×10^{-3}	10	1.15×10^{-3}
4	12.80	11	1.2×10^{-3}	21	5.1×10^{-4}
8	15.15	21	1×10^{-3}	41	2.35×10^{-4}

Table 4.4: Domain Decomposition errors in the velocity $\|\epsilon\|_\infty = \|u_{exact} - u_{DD}\|_\infty$ at $t = 4.0124$ (s) of oscillating flow for two different coarse grids.

is applied in the two-dimensional computations for the pulse-tube so that an accurate solution is obtained in an efficient way. The regenerator is still modelled as a 1D body where friction and heat transfer with the solid are automatically taken into account by Darcy's law.

New in this chapter is the domain decomposition method to improve the efficiency of the 2D computation at least for the single-stage PTR. The storage of data and computations are done with smaller systems than in the case of an entirely uniform grid. We only need to deal with a structured A-matrix which has big advantages compared with tensor grids [48]. In addition, we are allowed to take much larger time steps because of a less restrictive CFL condition in comparison with that of the tensor grid. To assess the computational gain by our domain decomposition technique we defined the gain factor (gf) as the ratio between the number of operations for the fine uniform grid and for the DD grid for one time step.

Another new element is to couple the main parts of the system, the pulse-tube, the regenerator(s) and the bypasses. In both cases of ideal and non-ideal gas we applied the proper interface (junction) conditions. Depending on the final model chosen for the single- and multi-stage PTR we may choose different coupling algorithms. The final model chosen for the multi-stage PTR in this thesis introduces fully decoupled gas temperature equations between the pulse tubes and the regenerators. Of course whithin each regenerator the gas and solid temperatures are still fully coupled.
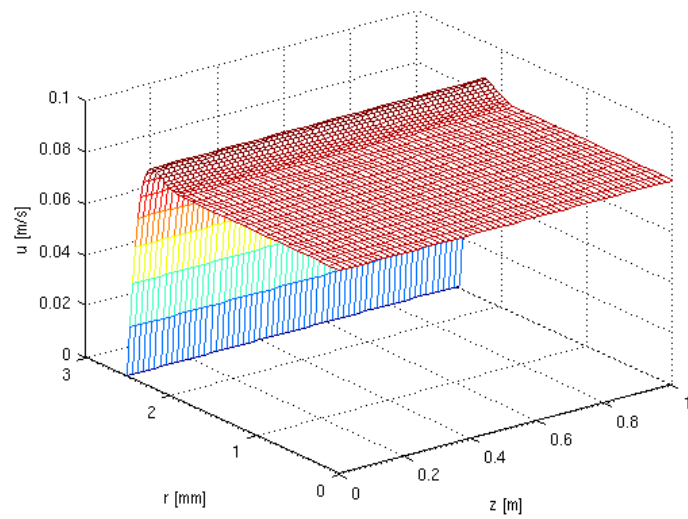
Figure 4.9: Uniform velocity profiles at t = 2.0125 [s] of the pipe flow due to an oscillating pressure gradient using Domain Decomposition method, $N_z = 61, N_r = 21, N_b = 21, f = 4$.

Chapter 5

Numerical results for the single-stage PTR

In Chapter 3 we derived the mathematical models describing the single-stage PTR in 1D and 2D. The governing equations were discretised in Chapter 4 and numerical algorithms were given to solve the equations and boundary conditions. In this chapter we show numerical results obtained for a typical single-stage PTR. First we present the one-dimensional results for the velocity and the temperature of the gas in the pulse-tube together with the gas velocity, gas temperature, material temperature and pressure in the regenerator. Meanwhile we explain the importance of choosing the initial condition for the temperature in the pulse tube. Second we present the two-dimensional results of a typical single-stage PTR (that is 2D pulse-tube and 1D regenerator), where all effects of friction at and heat transfer with the wall are included. Third we improve our 2D computations by using a domain decomposition method to increase the efficiency in terms of CPU complexity and memory storage. Finally we present the physical efficiency of the PTR in terms of mass and enthalpy flow and we check the coefficient of performance of the system. The lowest temperature that can be reached at the point where there is no cooling power anymore. The computation takes much time to reach the full oscillatory steady state when starting from room temperature, which is the initial temperature in reality. Therefore, an efficient initial temperature distribution is proposed.

5.1   One-dimensional simulation of a single-stage PTR

The mathematical model consists of the equations for the pulse tube (3.2.32), (3.2.33) with the boundary conditions (3.2.60), (3.2.68), (3.2.69) and initial conditions for the velocity (3.2.70) and the temperature, which will be explained in more detail later on, together with the equations for the regenerator (3.2.47), (3.2.49), (3.2.53) and (3.2.54) with
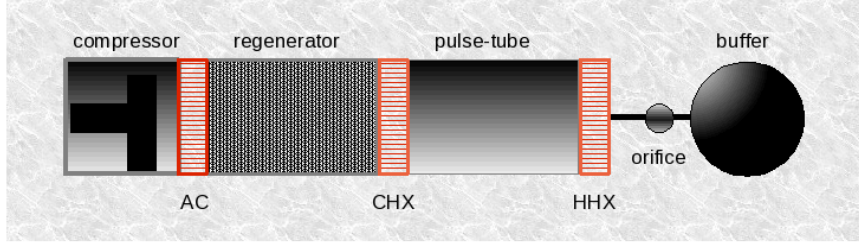
Figure 5.1: Stirling Pulse-Tube Refrigerator with orifice and reservoir.

the boundary equations (3.2.73), (3.2.74), (3.2.75), (3.2.76). The pressure at the compressor side is defined by $p_c(t) = p_{av} - \overline{p}sin(\omega t)$, with given values p_{av}, $\overline{p}$ and ω. The results for a typical single-stage pulse-tube refrigerator are obtained with the numerical methods described in Algorithm 4.1, Section 4.2.1 and Algorithm 4.5. The fluid flowing in the PTR is helium. The length of tube and regenerator is 200 mm each, the inner diameter is 50 mm. The physical parameters and corresponding non-dimensional numbers used in our single-stage PTR simulation are given in Appendix B. The frequency of the system is 20 Hz which makes it a high-frequency orifice pulse-tube refrigerator. See Fig. 5.1

5.1.1 Results of one-dimensional simulation with linear initial temperature

The tube and the regenerator domains are each discretised into 100 equi-spaced intervals of length Δz, i.e. the number of grid points $N = 101$ each. The dimensionless time-step is $\Delta t = 0.1\Delta z$. The heat exchangers are assumed to be already in steady state; they have constant temperature. We take the CHX's temperature $T_C = 60$ K and the HHX's $T_H = 300$ K. It turns out that after a number of cycles an oscillatory steady state is reached. That is the maximum norm of the difference of the gas temperature distribution ($\|T_g\|_\infty$) at all discretisation points in the tube of two consecutive cycles is less than a pre-defined tolerance (Tol). In other words, the solution shows full periodic behaviour.
Figure 5.2.a displays the computed regenerator pressure at two different positions, one at the compressor side, AC, and one at the interface with the pulse tube, CHX. There is a phase difference between the pressure at these two positions caused by the resistance to the flow by the regenerator (porous medium) and the porosity. Here $\phi = 0.7$. For the same reason the amplitude of the pressure at the end of the porous medium (CHX) is less than that at the compressor side. The pressure in the frictionless tube is uniform and only a function of time so that it is equal to the pressure computed at the interface. In Figure 5.2.b the gas velocity at the two end positions of the tube, one at CHX and one at HHX, is shown. The resistance law at the orifice (3.2.60) gives the velocity at
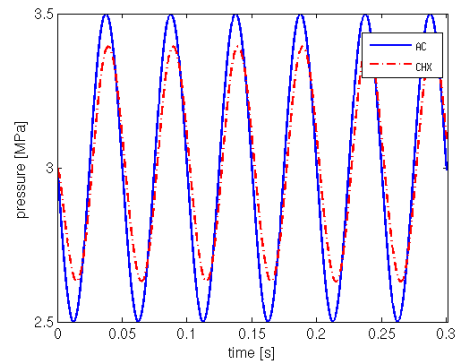
(a) Pressure
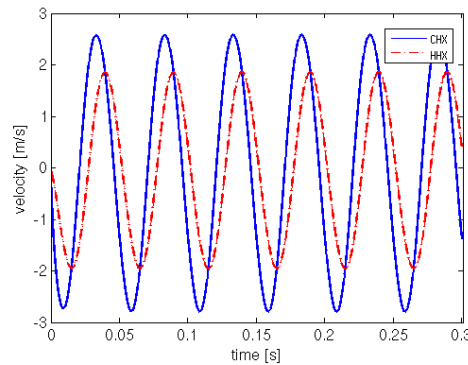
(b) Velocity

Figure 5.2: Pressure in the regenerator at AC and CHX and velocity in the tube at CHX and HHX.

HHX. The orifice conductance (C_{or}) which is optimised based on the thermodynamic analysis of PTRs described in [15]. There is a phase difference of about $\pi/4$ between the velocities at the cold and hot ends. In Figure 5.3 the gas velocity distribution in the tube at various times is shown. It has a nearly linear behaviour during the gas oscillation and it is nearly constant at the instant that the pressure gradient is zero. To explain this, consider the velocity equation (3.2.32). The second derivative of the temperature has a small coefficient, $b_1 \ll 1$, i.e. the Peclet number Pe is very small, which makes the velocity gradient practically proportional to the pressure time-derivative, which is constant in space. In the transition, from compression to decompression and vice versa, the pressure time-derivative becomes zero and the velocity in the tube becomes spatially uniform.

Figure 5.4 shows temperature using a linear distribution as initial condition. There is a part of the temperature which stays practically linear during the oscillation. This part of the profile - called the *gas piston* - never leaves the tube as it moves up and down, and left and right and remains unchanged. It undergoes adiabatic compression and expansion during the oscillation. However, the gas adjacent to the cold and hot ends leaves
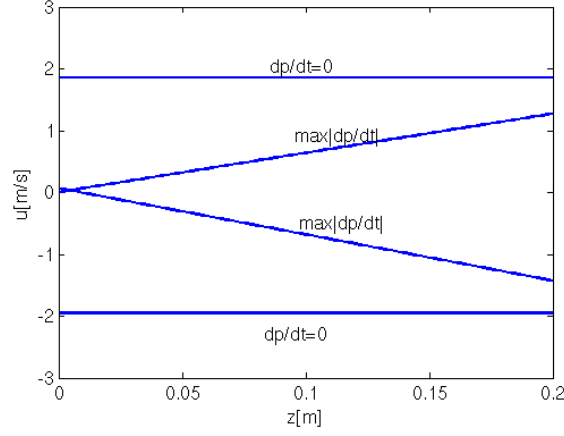
Figure 5.3: Velocity profile in the tube at different times.

the tube during each cycle. The gas adjacent to the hot end moves into the buffer and comes back into the tube, and at the cold end it flows into the regenerator and comes back. Figure 5.5 shows the temperature at the cold end and at the hot end obtained with the linear initial condition for the gas temperature. They exhibit either overshooting peaks at the cold end or undershooting peaks at the hot end. In Figure 5.5 we have indicated the "peaks" by a circle. These peaks remain in the temperature profile even for a rather long time. Although in reality the system has to cool down from room temperature, we have taken the initial shape of the gas temperature close to the steady oscillatory state [23], [24].

5.1.2   Choice of initial condition based on oscillatory steady state

We can choose any function as the initial condition for the temperature in the tube. An obvious choice is a straight line from the cold end temperature (T_C at CHX) to the hot end (T_H at HHX). However, as shown in Figure 5.5, this gives unsteady peaks in the temperature profile in the first cycles of the oscillation; they slowly decay in later cycles, but never vanish entirely [50], [48]. To obviate the peaks we take as initial condition a third-degree polynomial as:

$$T_g(z) = a_1 z^3 + a_2 z^2 + a_3 z + a_4, \qquad (5.1.1)$$

that interpolates four points in the temperature-distance diagram shown in Figure 5.6. The four points are: one point at the CHX with T_C, one point at the HHX with T_H, a point with its distance to CHX equal to the maximum penetration of the flow at the cold end (z_C) with T_C, and likewise the fourth point with its distance from the HHX equal to the maximum penetration of the flow at the hot end (z_H) with T_H. Figure 5.6 shows an example where $T_C = 60$ K and $T_H = 300$ K. The maximum penetration depths can be found either by trial and error from preliminary numerical simulations or they can be

(a) $\hat{t} = 10\pi, (p_{av})$

(b) $\hat{t} = 10.5\pi, (p_{av} - \bar{p})$

(c) $\hat{t} = 11\pi, (p_{av})$

(d) $\hat{t} = 11.5\pi, (p_{av} + \bar{p})$
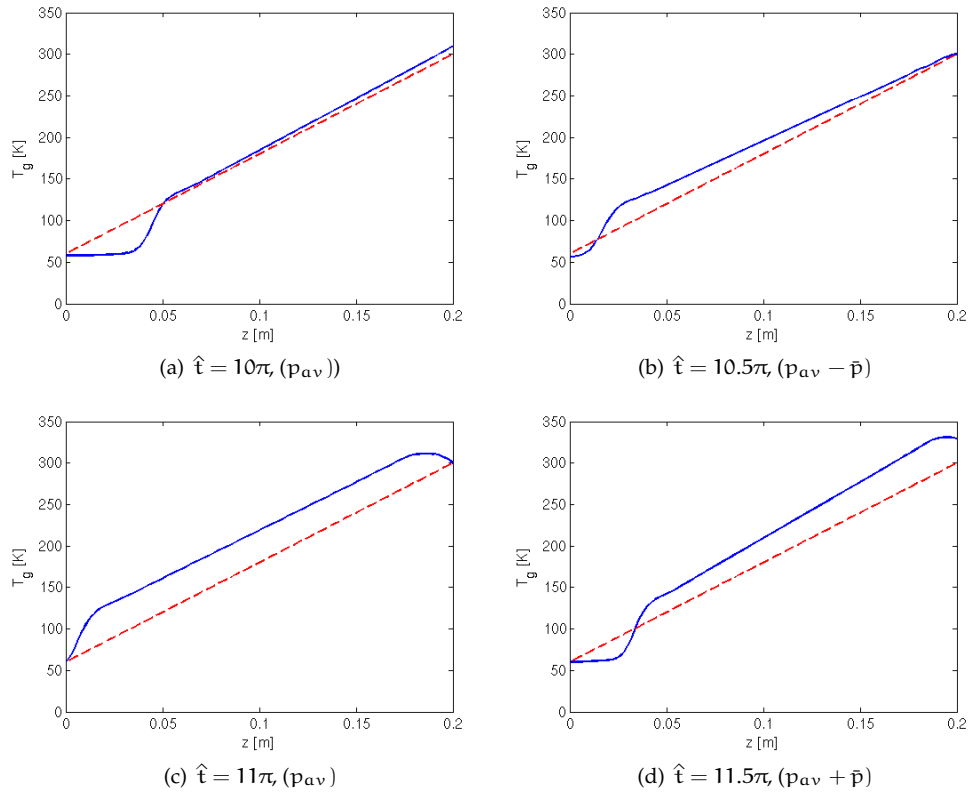
Figure 5.4: The temperature profile (continuous line) at four different times of a full steady oscillatory cycle with linear initial gas temperature (dashed line).

(a) cold end
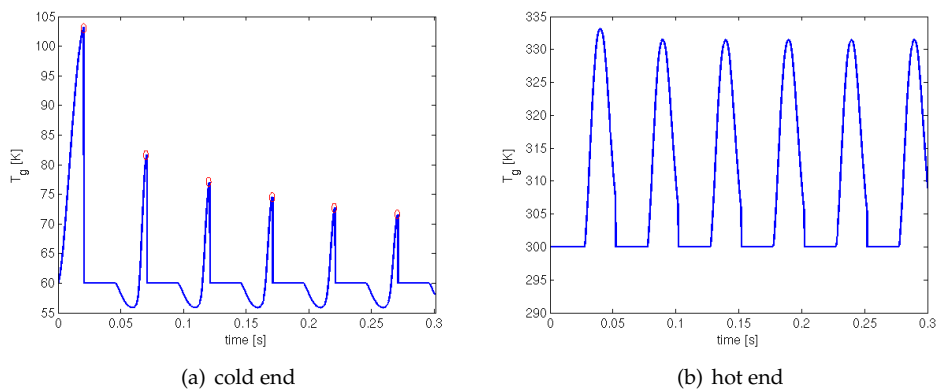
(b) hot end

Figure 5.5: Temperature history at the cold and hot end obtained with a linear initial temperature.

estimated from physical formula (based on harmonic analysis), [15, 16]. The analytical formula for the dimensional maximum penetration depths read

$$
z_H = \left(\frac{2\bar{p}}{\alpha \gamma p_{av}} \right) L_t = \frac{2\bar{p}C_{or}}{A_t \omega},
$$

$$
z_C = L_t - \left(2\sqrt{\frac{1+\alpha^2}{\alpha^2}} \frac{\bar{p}}{\gamma p_{av}} \right) L_t = L_t - \sqrt{1+\alpha^2} z_H,
$$

(5.1.2)

where

$$
\alpha := \frac{A_t L_t \omega}{\gamma C_{or} p_{av}}.
$$

Here the dimensional maximum penetration depths, using (5.1.2), are at $z_C = 5.64$ cm
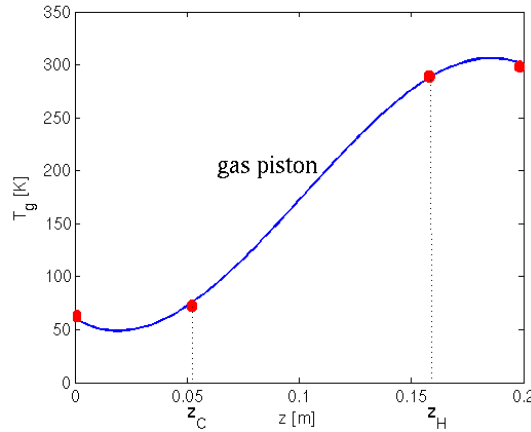
Figure 5.6: Initial temperature profile defined by a third-degree polynomial interpolating the four points: T_C at $z = 0$, T_H at $z = L_t$, T_C at $z_C :=$ '*maximum penetration at the cold end*' and T_H at $z_H :=$ '*maximum penetration at the hot end*'.

and $z_H = 16.02$ cm.

The interpolation makes the profile adjacent to the gas piston, $z_H \leq z \leq L_t$, have a temperature higher than T_H (while flowing towards the hot end, heat is released to the environment at HHX) and for the range of $0 \leq z \leq z_C$ a temperature lower than T_C is used (while flowing towards the cold end, cooling takes place at CHX). This initial condition prevents the temperature profile to have unwanted peaks in the beginning of the oscillations. Figure 5.4 shows that in each first half of a cycle some amount of gas leaves the system with a lower temperature than T_C and in the next half of the cycle returns back to the system with T_C, according to the reciprocating nature of the flow. The same behaviour occurs at the hot end.

5.1.3 Results of one-dimensional simulation with a dedicated initial temperature

In Figure 5.7 temperature profiles calculated with initial condition (5.1.1), (5.1.2) are shown at two different times corresponding to the maximum penetration (displacement) of the gas into the tube at the cold and hot end. Figure 5.8 shows that no undesired peak is created anymore at the cold or hot end, i.e. the temperature does not get higher than T_C at the cold end and not lower than T_H at the hot end.

(a) Max. penetration at the cold end at $\hat{t} = 10\pi$ (b) Max. penetration at the hot end at $\hat{t} = 11\pi$
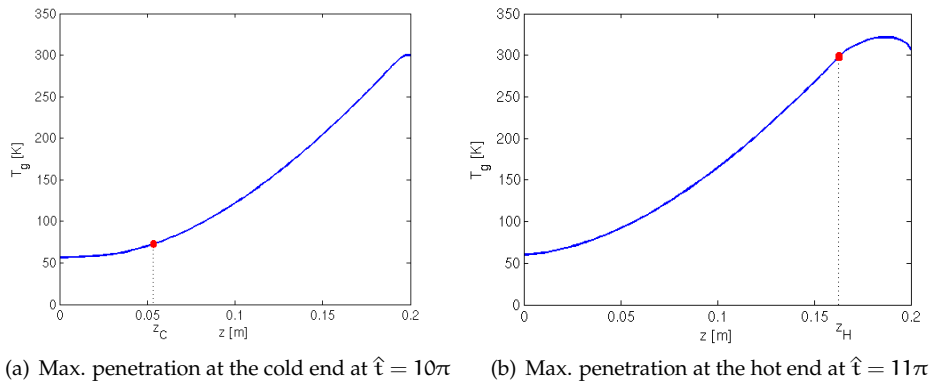
Figure 5.7: Temperature profiles in the pulse tube at two different times when maximum penetration of the gas into the domain occurs.

(a) cold end   (b) hot end
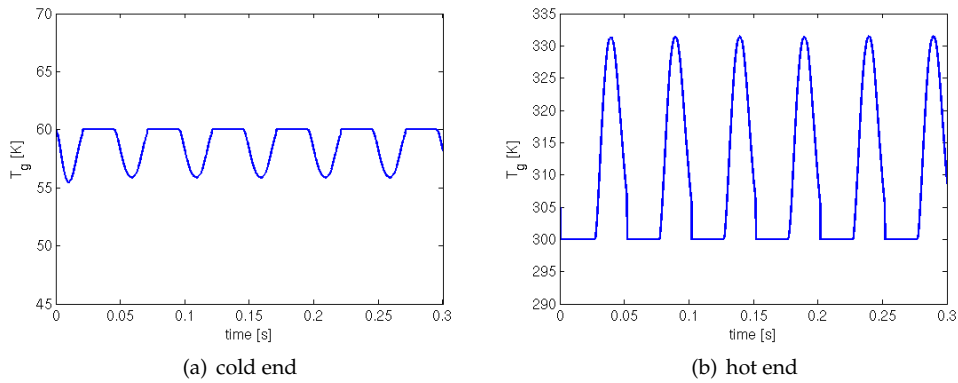
Figure 5.8: Temperature at the cold and hot end during the first 6 cycles, obtained with a cubic initial temperature.

Figures 5.8.a and 5.8.b display the temperature at the cold and the hot end of the tube calculated for the first six cycles. No peaks occur.
To verify our numerical results we compare the temperature in the middle of the tube with an analytical solution (for $k_g = 0$; see Appendix A). Figure 5.9 shows that the
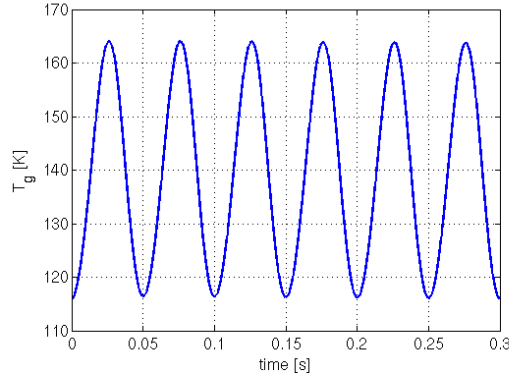
Figure 5.9: Temperature in the middle of the tube obtained by numerical and analytical methods. There are no visible differences.

results are practically the same.

5.2 Two-dimensional simulation of a single-stage PTR

To improve our 1D simulation of the pulse-tube refrigerator, especially in view of wall effects due to friction and heat transfer, we implement a two-dimensional model for the tube.   The two-dimensional tube model consists of the equations (3.3.26) for the gas temperature T_g and (3.3.28) for the wall temperature T_w, the equations (3.3.21), (3.3.22) and (3.3.25) for the axial velocity u, the radial velocity v and the hydrodynamic pressure p. The boundary conditions are presented in Table 3.1 and the initial conditions similar to 1D IC plus initial radial velocity as $v(z, r, 0) = 0$. The pressure of the compressor is defined by $p_c(t) = p_{av} - \overline{p} \sin(\omega t)$, where $p_{av}, \overline{p}$ and ω are assumed to be given. The same physical parameters as in the one-dimensional model are used (Appendix B). In our simulation we discretise the axisymmetrical tube domain with $N_z = 101, N_r = 101$ and $N_w = 5$ grid points in the axial direction, radial direction and in the wall, respectively.

The numerical results are obtained with the pressure-correction Algorithm 4.2 and the high-resolution method for the energy equation explained in Section 4.1.2. We solve the energy equations for the gas and the wall (3.3.26) and (3.3.28) simultaneously with the boundary and interface conditions given in Table 3.1.

Figures 5.10, 5.11 show the gas and the wall temperature profiles in the tube during a full cycle of the compressor oscillation together with the corresponding flow fields. The wall effect due to heat transfer with the wall is clearly visible. There exists a significant difference in temperature for the gas near the wall and the smooth part in the core of the domain. The penetration effect (5.1.2) at the cold end and at the hot end is evident. The temperature profile has most variation near the cold entrance in the "*cold layer*", near the hot entrance in the "*hot layer*" and near the wall in the "*wall layer*". The boundary layer at the wall is thin. The majority of the temperature profile between the cold layer,
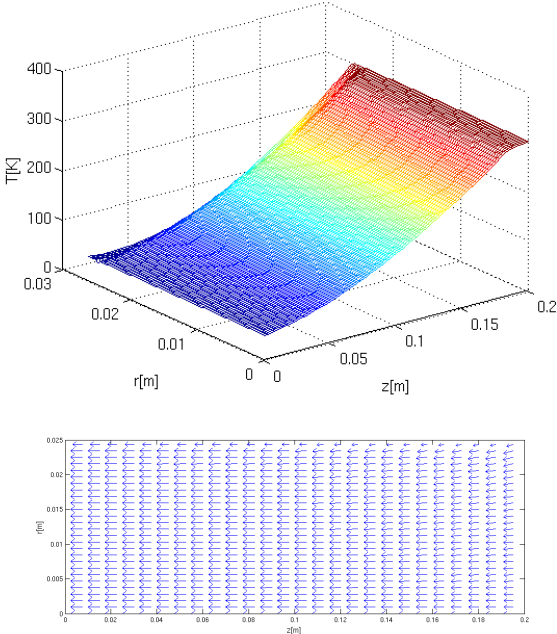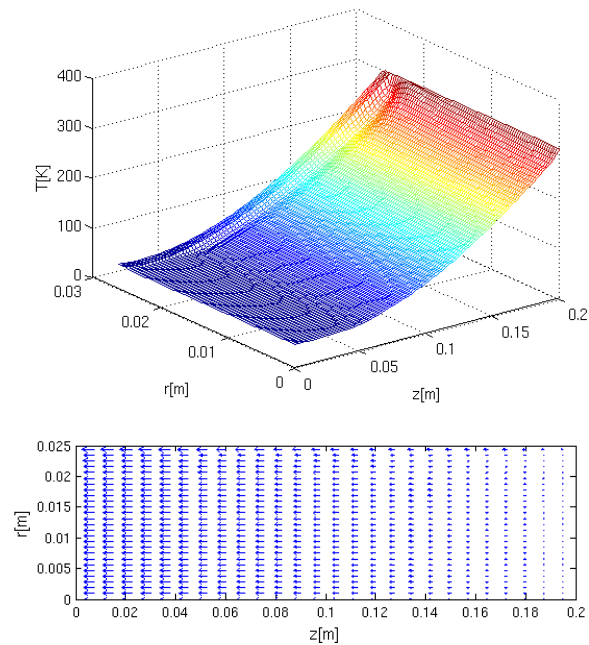
(b) $\hat{t} = 4.5\pi \, (p_c = p_{av} - \bar{p})$
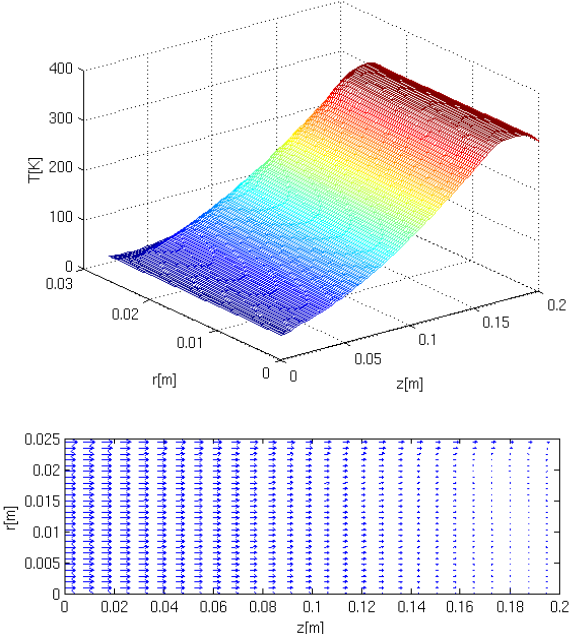
(d) $\hat{t} = 5\pi \, (p_c = p_{av})$

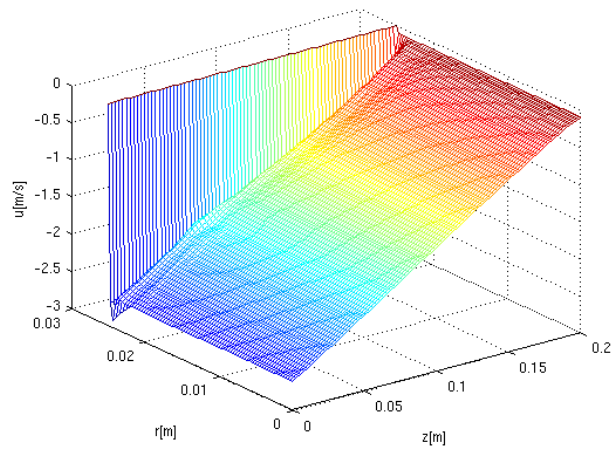Figure 5.10: Temperature profiles and velocity fields during the third cycle of the compressor oscillation.
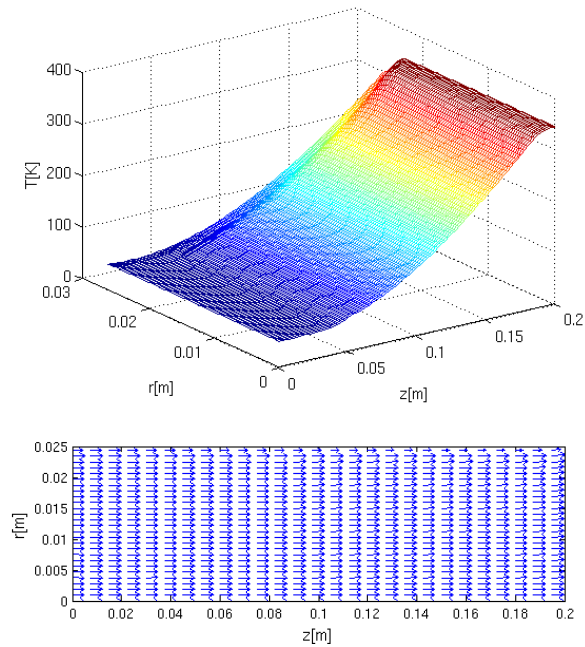
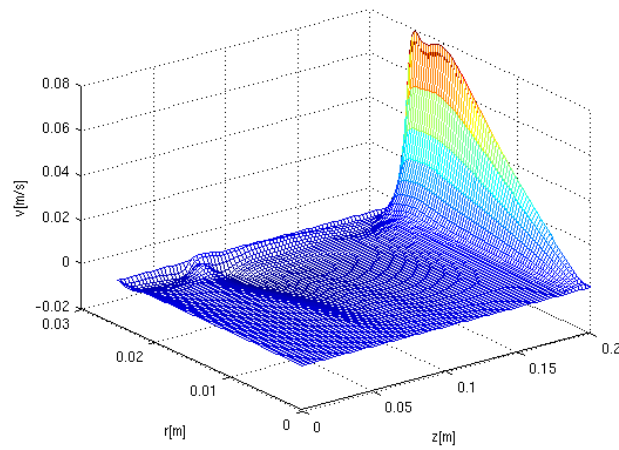(b) $\hat{t} = 5.5\pi \, (p_c = p_{av} + \bar{p})$

(d) $\hat{t} = 6\pi \, (p_c = p_{av})$

Figure 5.11: Temperature profiles and velocity fields during the third cycle of the compressor oscillation.

(a) Axial velocity

(b) Radial velocity

Figure 5.12: Axial and radial velocities at the end of the third cycle ($\hat{t} = 6\pi$, $p = p_{av}$).

hot layer and the wall layer, i.e. the core of the domain the so-called gas piston, stays smooth.

Figure 5.12 shows the results of the pressure-correction algorithm (Algorithm 4.2) for the axial and radial velocities. The wall effect is clearly visible in the axial velocity distribution. The no-slip condition for the velocities and the heat flux at the interface with the wall create viscous and thermal boundary layers. The entrance effect is well visible in the radial velocity distributions in Figure 5.12. As observed the radial velocity varies from zero (the BC at the hot end) with a very big gradient to $v = 0.08$ [m/s].

5.3   Domain Decomposition method

As explained in the previous section, the cold layer, the hot layer and the boundary layer on the wall are the high-activity regions in the table. See Figure 5.13. Therefore, we use the same domain decomposition method as introduced in Section 4.5.
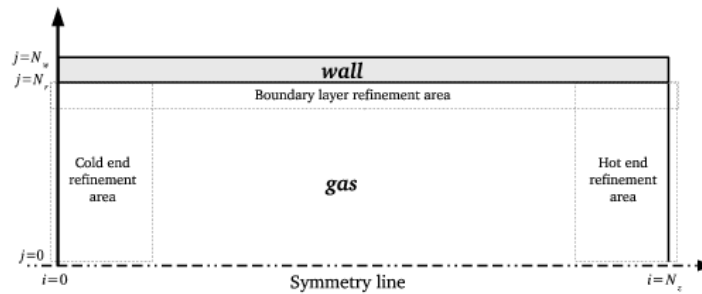
Figure 5.13: The domain decomposition areas in the tube.

5.3.1   Refinement conditions

To optimise the computational efficiency by taking fine sub-grids rather than one fine uniform grid, we need to find the thicknesses of the high-activity zones. In the core of the domain the flow and temperature oscillates and behaves quite smoothly. We refine the grid in the high-activity regions and we keep the core of the domain gridded as coarse as possible thereby still meeting the desired global tolerance. We take a uniform grid to obtain a desirable tolerance for all variables in all high-activity regions as depicted in Figure 5.14. To determine the layer thicknesses we use discrete approximations of the gradients of T, u, v and p both in radial and axial directions namely

$$\frac{\partial T}{\partial z}, \quad \frac{\partial T}{\partial r}, \quad \frac{\partial u}{\partial z}, \quad \frac{\partial u}{\partial r}, \quad \frac{\partial v}{\partial z}, \quad \frac{\partial v}{\partial r}, \quad \frac{\partial p}{\partial z}, \quad \frac{\partial p}{\partial r}. \tag{5.3.1}$$

The final result is the maximum layer's thickness at the cold end, hot end and the boundary layer at the wall. The analysis is done for all the variables T, u, v, p at $\hat{t} = \pi/2$, $\hat{t} = \pi$, $\hat{t} = 3\pi/2$, $\hat{t} = 2\pi$ in the first cycle. For instance, the discrete temperature gradient at $\hat{t} = \pi/2$ is shown in Figure 5.15. The radial variation of the temperature is high in the boundary layer at the wall. This variation slowly vanishes after almost one tenth of the tube's radius. The axial variation of the temperature is high at the one fifth of the tube's length at the hot layer and one tenth of the tube's length at the cold layer. Similar results are obtained for the other variables. Table 5.1 summarises the high-activity regions.

Layer	Width
Wall layer	$L_w = r_0/10$
Cold layer	$L_c = L_t/10$
Hot layer	$L_h = L_t/5$

Table 5.1: High-activity layer widths.

5.3.2   Numerical results

We now have four systems to solve, according to sub-domains sketched in Figure 5.16:

- one is for the coarse grid of dimension $(N_z \times N_r)$,

- one is for the boundary layer at the wall of width L_w, with radial refinement factor f_1 with dimension $(N_z \times f_1 N_r)$,

- one is for the cold layer of width L_c, with axial refinement factor f_2 with dimension $(f_2 N_z \times N_r)$ and

- one is the hot layer of width L_h, with axial refinement factor f_3 with dimension $(f_3 N_z \times N_r)$.

Let the dimensionless boundary layer thicknesses be L_w, L_c and L_h (Table 5.1). Since the radius of the tube is much smaller than its length, we get axial space steps in the domains $(L_c \times r_0)$ and $(L_h \times r_0)$ that are larger than the radial space step

$$\delta z_{(L_c \, or \, L_h)} > \Delta r.$$

Thus we may still obtain the time step, Δt, for these two systems. Let us summarise the number of grid points and the resulting complexity
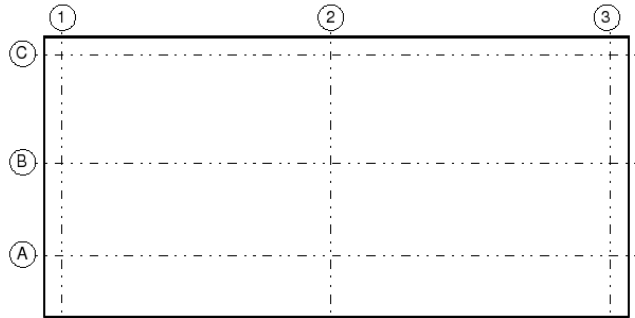
Figure 5.14: View lines at different positions in the tube to monitor the width of the high-activity regions.
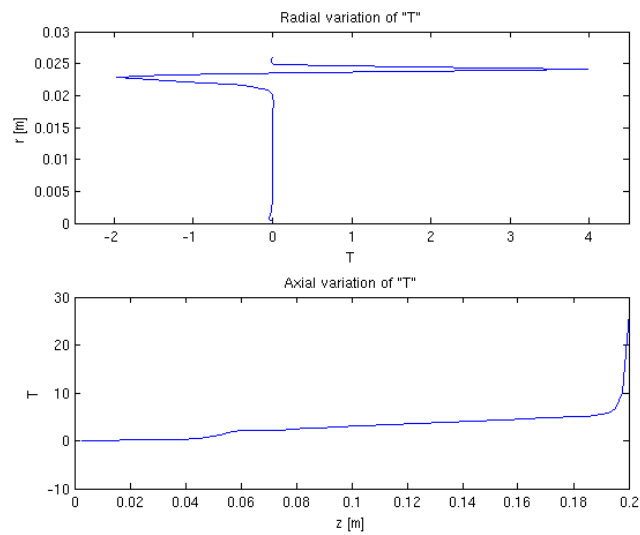

Figure 5.15: Radial and axial variation of the gas temperature at $\hat{t} = \pi/2$ using (5.3.1).

- *fine uniform grid*:
  - uniform grid: $(\max(f_2, f_3) N_z \times f_1 N_r)$,
  - flops: $\max(f_1, f_2, f_3).(\max(f_2, f_3) N_z \times f_1 N_r)^2$

- *DD grid*:
  - coarse grid: $(N_z \times N_r)$,
  - L_b grid: $(N_z \times N_r(\frac{L_b}{r_0}) f_1)$,
  - L_c grid: $((\frac{L_c}{L_t}) f_2 N_z \times N_r)$,
  - L_h grid: $((\frac{L_h}{L_t}) f_3 N_z \times N_r)$,
  - flops:
    $(N_z \times N_r)^2 + f_1 (N_z \times N_r(\frac{L_b}{r_0}) f_1)^2 + ((\frac{L_c}{L_t}) f_2 N_z \times N_r)^2 + ((\frac{L_h}{L_t}) f_3 N_z \times N_r)^2.$

Let us denote $f := \max(f_1, f_2, f_3)$, then the gain factor, cf. (4.5.10) is

$$gf \approx \frac{f^5}{1 + f_1{}^3 (\frac{L_b}{r_0})^2 + f_2{}^2 (\frac{L_c}{L_t})^2 + f_3{}^2 (\frac{L_h}{L_t})^2} \approx f^3 : f^4. \tag{5.3.2}$$

Notice that $\delta t_{L_c}, \delta t_{L_h}$ are equal to Δt. In Table 5.1 we have $L_b/r_0 = 1/10, L_c/L_t = 1/10$ and $L_h/L_t = 1/5$, for refinement factor $f = 10$, the gain factor is achieved as 6250 which is in the order of f^4.

The domain decomposition error is computed at one view line in the middle of the tube (line 2 in Figure 5.14) radially and one axial view line (line B in Figure 5.14) by $\|\epsilon\|_\infty = \|x_{\text{Ref}} - var_{\text{DD}}\|_\infty$, where var denotes one of the variables, T_g, u, v and p. Also, var_{Ref} is the solution obtained on a fine uniform grid with $N_z = 201$, $N_r = 201$ and $N_w = 11$. Table 5.2 shows the estimated error for all the variables calculated with domain compositions in radial and axial directions at the end of the third pressure cycle.

In Figures 5.17 and 5.18 the velocity distribution and the temperature profile at the end of the third pressure cycle obtained by the domain decomposition method are displayed. The solution has quite smooth behaviour in the core of the domain and sharp variation in the boundary layer where it has been refined. The high-activity regions have refined grids so that the behaviour in these regions is represented more accurately.

5.4 Mass and enthalpy flow, cooling power and efficiency

The *mass flow* is defined by

$$\dot{m} := \int_A \rho_g u \, dA, \tag{5.4.1}$$

where A is the cross-sectional area of the tube, u is the axial velocity and ρ_g is the gas density. The integration gives the average value in the cross section where for a cylinder
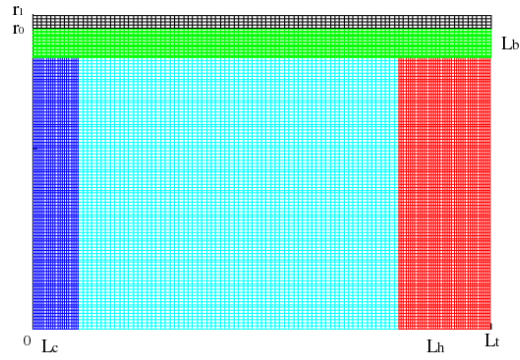
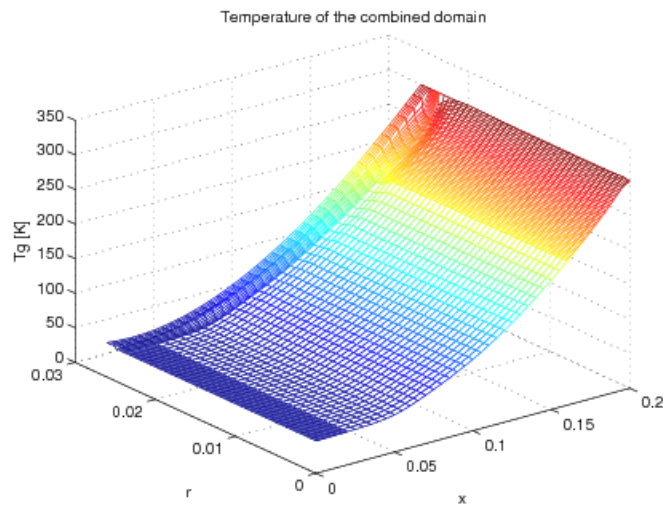Figure 5.16: Domain decomposition grids in the tube.

Figure 5.17: Temperature distribution obtained by DD.

$(N_z \times N_r)|_{uniform} = (201 \times 201)$			
f	2	5	10
coarse	(101×101)	(41×41)	(21×21)
L_b	(101×21)	(41×21)	(21×21)
L_c	(21×101)	(21×41)	(21×21)
L_h	(41×101)	(41×41)	(41×21)
$\|\epsilon_T(\text{axial})\|_\infty$	0.131×10^{-2}	0.58×10^{-2}	2.22×10^{-2}
$\|\epsilon_T(\text{radial})\|_\infty$	0.45×10^{-2}	1.98×10^{-2}	4.03×10^{-2}
$\|\epsilon_u(\text{axial})\|_\infty$	0.674×10^{-2}	2.82×10^{-2}	1.94×10^{-2}
$\|\epsilon_u(\text{radial})\|_\infty$	1.25×10^{-2}	4.59×10^{-2}	8.49×10^{-2}
$\|\epsilon_v(\text{axial})\|_\infty$	1.01×10^{-6}	1.59×10^{-5}	6.42×10^{-5}
$\|\epsilon_v(\text{radial})\|_\infty$	1.24×10^{-6}	2.8×10^{-5}	2.2×10^{-4}

Table 5.2: Absolute errors $\|\epsilon\|_\infty = \|x_{Ref} - x_{DD}\|_\infty$ computed by domain decomposition for all variables T_g, u, v in the tube at the end of the third pressure cycle for three different grids.

$dA = 2\pi r dr$. The mass flow is almost harmonic in time. The net or *cycle-averaged mass flow* is

$$\bar{\bar{m}} := \frac{2\pi}{t_c} \int_t^{t+t_c} \int_0^{r_0} (\rho_g u r) dr dt, \tag{5.4.2}$$

where t_c is the cycle period. The calculated net mass flow at the cold end, the middle and the hot end are of the order of 10^{-6} [kg/s]. This is small compared to the mass flow amplitudes at the cold and hot ends which are of the order of 10^{-2} [kg/s] after 100 full cycles.

The cycle-averaged enthalpy flow for ideal gas is computed by

$$\bar{H} := \frac{1}{t_c} \int_t^{t+t_c} \int_A (\rho_g u h) dA dt = \frac{2\pi}{t_c} \int_t^{t+t_c} \int_0^{r_0} (\rho_g u c_p T_g r) dr dt. \tag{5.4.3}$$

In the harmonic approach [65] the cycle-averaged enthalpy flow is estimated by the following relation (valid only for sinusoidal driving pressure of small amplitude)

$$\bar{H} = \frac{1}{2} C_{or} \bar{p}^2, \tag{5.4.4}$$

where C_{or} is the orifice conductance and $\bar{p}$ is the pressure variation. The time-averaged enthalpy flow in the tube is 225 [W]. The estimated enthalpy flow from (5.4.4) given for comparison is 188 [W]. This shows the numerical enthalpy flow is of the same order as the estimated one.

The input power is the energy that we supply to the system. A control section at the hot end of the regenerator is taken such that it contains the AC and a short part of the regenerator as shown in Figure 5.19. The input power is

$$\text{Input Power} = \frac{1}{t_c} \int_t^{t+t_c} \int_{A_r} (p_c u_c) dA_r dt = \frac{2\pi}{t_c} \int_t^{t+t_c} p_c \int_0^{r_0} (u_c r) dr dt, \tag{5.4.5}$$

where p_c is the driving pressure, u_c is the velocity at the compressor side and A_r is the regenerator cross-sectional area. The *coefficient of performance* is the ratio of of the cooling power, which for ideal gas is the cycle-averaged enthalpy flow at the cold end, divided by the input power,

$$\text{COP} := \frac{\bar{H}_{CHX}}{\text{Power}}. \tag{5.4.6}$$

This coefficient gives the efficiency of the machine which is always smaller than the *Carnot efficiency*

$$\text{COP}_{\text{Carnot}} := \frac{T_C}{T_H - T_C}. \tag{5.4.7}$$

After 150 pressure cycles, the following numerical results are obtained:

- the *cooling power*: 225 [W]

- the *input power*: 1873 [W]

- *COP*: 0.12.

The efficiency of the simulated machine is about 50% of the Carnot efficiency which is $(60/240) = 0.25$. This, of course, is too much over-estimated for a real system, but our computation is based on ideal heat exchangers and constant material properties of gas and solid.

5.5   Conclusion

In this chapter we have presented numerical results obtained for a typical single-stage PTR. We have shown the one-dimensional results for the velocity and the temperature of the gas in the pulse-tube together with the gas velocity, gas temperature, material temperature and pressure in the regenerator. The regenerator simulation as well as the implicit coupling method between the pulse tube and the regenerator are new compared to previous work at TUE.

We have explained the importance of choosing the initial condition for the temperature in the pulse tube. In this method we have applied the new idea of using the maximum penetration depths at both sides of the pulse tube, of the HHX and of the CHX, to prevent the temperature profile to have unwanted peaks in the oscillations.

We have presented two-dimensional results for a typical single-stage PTR (that is 2D pulse-tube and 1D regenerator), where all the effects of friction and heat transfer with the wall are included. New in this part is that an implicit coupling algorithm has been applied to connect the 2D pulse tube and the 1D regenerator properly. In this way, pressure continuity, mass and enthalpy conservation are maintained at the interface. The initial condition for the 2D gas temperature was imposed in the same style as that in the 1D model, so to prevent unwanted peaks of the 2D gas temperature profile of the oscillations.

One new addition is that the 2D simulation was improved by using a domain decomposition method to increase the efficiency of computation in terms of CPU complexity and memory storage. The corresponding efficiency parameter introduced in Chapter 4, namely the gain factor, is of the order of 10^4.
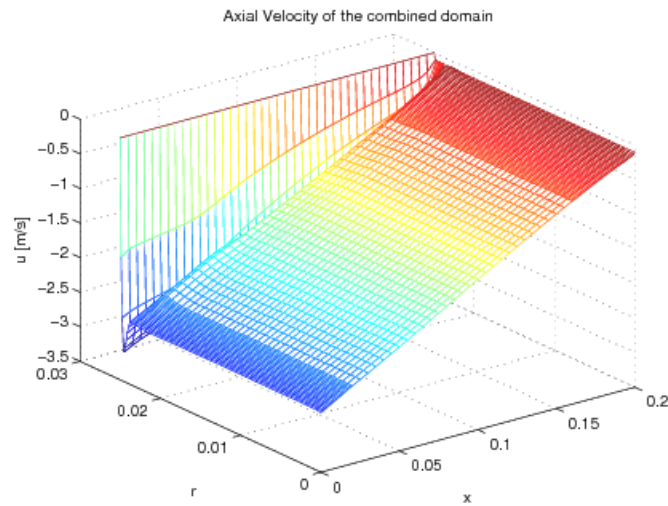
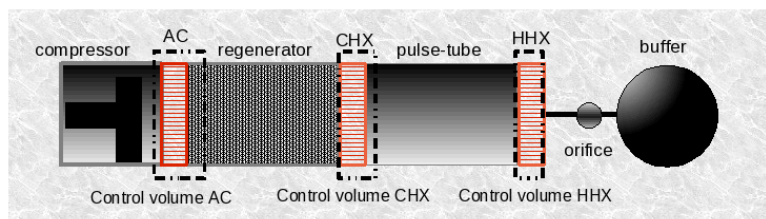Figure 5.18: Axial velocity distribution obtained by DD.

Figure 5.19: Control volumes for computing the enthalpy flows at CHX and HHX and the input power at AC.

Chapter 6

Numerical results for the three-stage PTR

In this chapter we simulate two different three-stage double-inlet PTRs, one existing laboratory system operating at low frequency to illustrate our code and the other one operating at high frequency as stated in the final goal of this project. The numerical results obtained for a real gas are in terms of velocity, density, and gas and solid temperatures. The pressure and temperature dependent material properties of gas and solids are taken into account because these are significant in the very low temperature range reached in the third regenerator and tube. Our numerical simulations show that the settings of the three main orifices and the three double-inlets are crucial in finding the lowest possible temperature.

6.1 Three-stage PTR configurations

A schematic picture of a three-stage PTR is shown in Figure 6.1. First, we simulate the three-stage PTR set-up in the laboratory of the Applied Physics Department of TU Eindhoven operating at low frequency (1.2 Hz) and reaching a lowest reported temperature of 2.19 K [67] at CHX3. The average pressure $p_{av} = 16.40$ [bar] and the pressure amplitude $\bar{p} = 3.77$ [bar]. The dimensions and the solid material properties of this three-stage PTR, referred to as PTR3-I, are presented in Table 6.1. The physical parameters and corresponding non-dimensional numbers used in the PTR3-I simulation are given in Appendix C.

Figure 6.2 is a schematic picture of the original set-up of PTR3-I [67]. The machine is a GM-type cooler with 9 tuning orifices. These are: three main orifices, three double-inlets and three minor orifices. The other valves are either fully open or fully closed. In the simulation we replace the GM compressor by a Stirling piston operating at the same
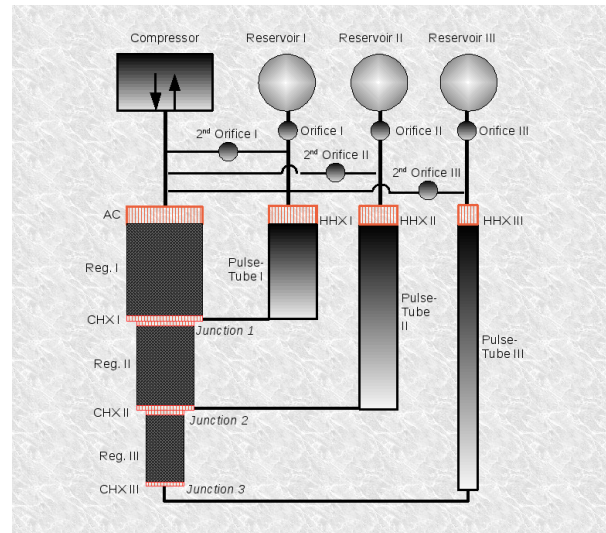
Figure 6.1: Schematic picture of the three-stage pulse-tube refrigerator.

PTR3-I		Stage I	Stage II	Stage III
Pulse tube	Inner diameter [mm] Length [mm]	20.0 141	12.1 204	7.65 430
Regenerator	Inner diameter [mm] Length [mm] Material Porosity	34 141 Stainless steel 0.682	20 130 Lead 0.60	14 155 ErNi 0.60

Table 6.1: Dimensions and solid material properties of the low-frequency PTR3-I.

frequency of 1.2 Hz. The three main orifices and the three double-inlets, whose roles are more prominent than the remaining three, are taken into account in the simulation. See Fig. 6.1. The simulation is that of a low-frequency PTR, for which experimental data is available, and it serves as a validation for the developed model.
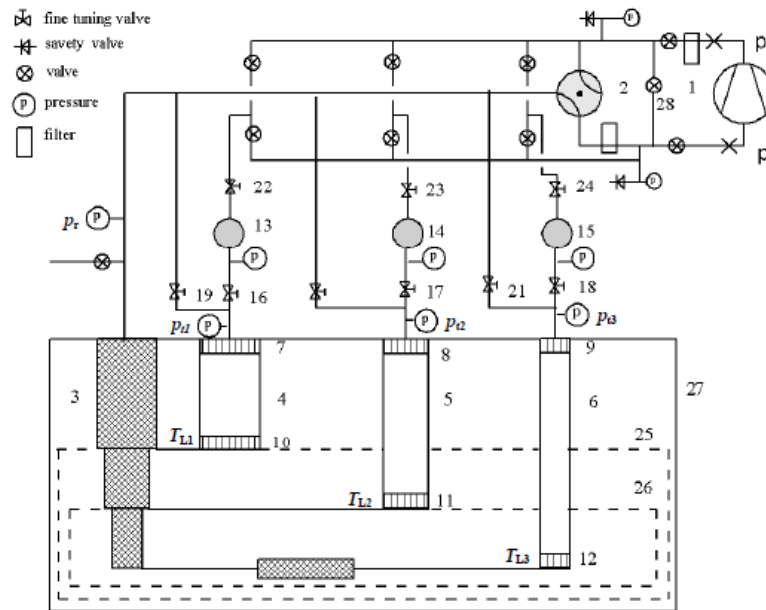
Figure 6.2: Schematic picture of PTR3-I. 1 - compressor; 2 - rotary valve; 3 - regenerator; 4-6 pulse tubes; 7-9 hot heat exchangers; 10-12 cold heat exchangers; 13-15 buffers; 16-18 first orifices; 19- 21 double-inlet valves; 22-24 minor orifices; 25 1st heat shield; 26 2nd heat shield; 27 cryostat; 28 bypass valve [67].

Second, a high-frequency PTR (20 Hz), referred to as PTR3-II, is modeled using the same materials as PTR3-I but with different geometry. The geometry of PTR3-II is given in Table 6.2. These data have been provided by the low-temperature group of the Applied Physics Department of TU Eindhoven. The physical parameters and corresponding non-dimensional numbers used for the PTR3-II simulation are given in Appendix C.

6.2 Mass and enthalpy flow, cooling power and efficiency

In this section the essential quantities that determine the efficiency of PTRs are given. All of them are found by post-processing the data computed in the simulations.
The mass flow is

$$\dot{m} = \rho_g u A \qquad (6.2.1)$$

PTR3-II		Stage I	Stage II	Stage III
Pulse tube	Inner diameter [mm] Length [mm]	24.6 67.5	7.0 246	5.0 285
Regenerator	Inner diameter [mm] Length [mm] Material Porosity	72 65 Stainless steel 0.682	32 78.5 Lead 0.60	19 70 ErNi 0.60

Table 6.2: Dimensions and solid material properties of the high-frequency PTR3-II.

and the cycle-averaged mass flow is computed by

$$\overline{\dot{m}} = \frac{1}{t_c} \int_t^{t+t_c} (\rho_g u A) dt', \tag{6.2.2}$$

where t_c is the cycle period. The cycle-averaged or net mass flow is theoretically zero when the system has reached its steady oscillating state. The cycle-averaged enthalpy flow in the tube is computed for ideal gas by

$$\overline{\dot{H}}_t = \frac{1}{t_c} \int_t^{t+t_c} (\rho_g u A_t h) dt' = \frac{A_t c_p}{t_c} \int_t^{t+t_c} (\rho_g u T_g) dt'. \tag{6.2.3}$$

The enthalpy flow calculation in terms of real gas and temperature dependent heat capacity c_p and temperature-pressure dependent H_p is given by

$$\overline{\dot{H}}_t = \frac{1}{t_c} \int_t^{t+t_c} (\rho_g u A_t \partial h) dt' = \frac{A_t}{t_c} \int_t^{t+t_c} \rho_g u (c_p \partial T_g + \frac{1}{M} H_p \partial p) dt', \tag{6.2.4}$$

where c_p is given by (2.2.3) and H_p is given by (3.4.7). Since the heat capacity and H_p depend on the temperature and/or pressure, we need to compute the average enthalpy for small changes of temperature ∂T_g and pressure ∂p which are calculated locally in the post-processing, i.e. they are the properties at the discretised point at CHX.

The basic cooling power, which is equal to the cycle-averaged enthalpy flow in the pulse tube, can be estimated for ideal gas by [15, 16]

$$\overline{\dot{H}}_t = \frac{1}{2} C_{or3} \bar{p}_{t_3}^2, \tag{6.2.5}$$

where $\bar{p}_{t_3}$ is the pressure amplitude in the third tube and C_{or_3} is the conductance of the third orifice.

The cycle-averaged enthalpy flow for real gas in the regenerator is computed by

$$\overline{\dot{H}}_r := \frac{1}{t_c} \int_t^{t+t_c} (\rho_g u \phi A_r \partial h) dt' = \frac{\phi A_r}{t_c} \int_t^{t+t_c} \rho_g u (c_p \partial T_g + \frac{1}{M} H_p \partial p) dt'. \tag{6.2.6}$$

The cooling power Q_L, which is the cycle-averaged (net) enthalpy flow at the cold end of stage III minus the net enthalpy flow in the third regenerator, is then computed by

$$Q_L = \overline{H}_t - \overline{H}_r. \qquad (6.2.7)$$

If the heat flow due to conduction in the regenerator is taken into account, energy conservation gives

$$\overline{H}_r + Q_c + Q_L = \overline{H}_t, \qquad (6.2.8)$$

where Q_c is the heat flow at CHX in the regenerator towards inside the regenerator. Since the conductivity of the solid depends on the temperature, Q_c is calculated numerically for small changes of conduction at the cold part of the solid. The more realistic relation (6.2.8) shows that the cooling power is diminished by the heat and enthalpy flow in the regenerator if the gas is real. For ideal gas and an ideal regenerator solid

$$Q_L^{ideal} = \overline{H}_t. \qquad (6.2.9)$$

6.3 Numerical results

The simulation of a three-stage PTR with ideal gas and constant material properties is described in [25]. Here we use a real-gas equation of state, which is the Van der Waals equation (3.1.12), and real material properties for gas and regenerator solid (Section 2.3) in the whole system. The heat exchangers are still considered to be ideal. This assumption may lead to over-estimation of cooling power in all stages. We solve the governing equations for the three tubes consisting of (3.4.15), (3.4.18), (3.4.19) with the boundary conditions (3.2.60), (3.4.38), (3.4.39) and initial conditions for the velocity (3.2.70) and the temperature (in the way that was explained in Section 5.1.2), together with the equations for the three regenerators including (3.4.32), (3.4.33), (3.4.35), (3.4.36), (3.4.37) with the boundary equations (3.4.41), (3.4.42) and (3.5.7). The pressure at the compressor side is defined by $p_c(t) = p_{av} + \overline{p} \sin(\omega t)$, with given values p_{av}, $\overline{p}$ and ω, as the boundary condition for regenerator I in (3.4.32). The boundary condition for equation (3.4.32) is pressure continuity (3.5.1) at the junctions. The results for the three-stage PTRs are obtained with the numerical methods summarised in Algorithm 4.3, Algorithm 4.4 and Algorithm 4.5. The working fluid in the PTR is helium.

6.3.1 Low frequency PTR3-I

To validate our code to a certain extent we simulate the three-stage PTR set-up in the laboratory of the Applied Physics Department of TU Eindhoven that operates at a low-frequency of 1.2 Hz [67]. See Section 6.1. The tubes are discretised in $N_{T_1} = 114$, $N_{T_2} = 126$, $N_{T_3} = 266$ points and the regenerators in $N_{R_1} = 88$, $N_{R_2} = 81$, $N_{R_3} = 95$ points so that Δz is identical in all regenerators and tubes. The time-step is $\Delta t = 0.25 \Delta z$. We assign constant temperatures at the junctions one, two, and three, together with

Test-case	α_1 [-]	α_2 [-]	α_3 [-]	α_{d_1} [-]	α_{d_2} [-]	α_{d_3} [-]	T_{C_1} [K]	T_{C_2} [K]	T_{C_3} [K]	Q_{L_1} [W]	Q_{L_2} [W]	Q_{L_3} [W]
Trial-1	1.5	2.5	3.5	1.0	1.0	1.0	60	30	10	-1.77	2.77	0.2
Trial-2	1.5	2.5	3.5	1.0	1.0	1.0	58	30	10	-3.30	2.64	0.19
Trial-3	2.0	2.2	2.9	1.0	1.0	1.0	55	23	6.5	-0.3	3.29	-0.27
Trial-4	1.9	2.3	2.8	1.0	1.0	1.0	56	23.5	7	-0.66	3.34	-0.24
Trial-5	1.9	2.3	2.65	1.0	1.0	1.0	56.5	23	7.5	-0.41	3.42	-0.14
Trial-6	1.9	2.2	2.75	1.0	1.0	1.0	57	23.5	9	-0.08	2.81	0.22
Trial-7	1.9	2.2	2.75	1.0	1.0	1.0	57	23.5	8	2.87	3.74	-0.19
Trial-8	2.0	2.5	3.0	0.05	0.07	0.095	89.0	28.0	8.0	-1.210	-0.270	-0.180
Trial-9	2.0	2.5	3.0	0.01	0.07	0.095	96.0	35.0	8.7	-6.730	0.320	0.150
Trial-10	2.0	2.5	3.0	0.02	0.06	0.095	96.0	33.0	8.5	-2.280	0.160	0.120
Trial-11	2.0	2.5	3.0	0.02	0.06	0.095	101.0	31.0	8.0	-2.40	-0.055	0.0006
Trial-12	2.0	2.5	3.0	0.023	0.062	0.09	103.0	31.0	8.0	-1.77	-0.090	-0.080
Trial-13	2.0	2.5	3.0	0.023	0.061	0.092	105.0	31.0	8.0	-1.80	-0.210	-0.120
Trial-14	2.0	2.5	3.0	0.015	0.06	0.095	107.0	31.0	8.0	-4.10	-0.020	-0.010
Trial-15	2.0	2.5	3.0	0.025	0.062	0.099	91.0	25.0	8.2	-1.120	0.040	-0.004
Trial-16	2.0	2.5	3.0	0.02	0.06	0.095	101	31	7	-3.54	2.68	-1.05

Table 6.3: Cooling powers calculated at three CHXs with three fixed CHX temperatures based on six orifice settings for PTR3-I; α_i: main orifice settings, α_{d_i}: double-inlet settings, T_{C_i}: cold temperatures at CHXs, Q_{L_i}: cooling power at the junctions.

the settings for the orifices and double-inlets. Other physical properties such as average pressure, the driving pressure amplitude and material properties of gas and regenerator solids are fixed. The three initial temperature distributions in the tubes are based on the approach presented in Section 5.1.2. Three linear profiles, connecting the junction temperatures, are defined as initial conditions of the gas and solid temperatures in the regenerators. The lowest possible temperature in the system is found at CHX3. This temperature occurs when the cooling power at CHX3 is zero. The six orifice settings, α, have crucial roles in the efficiency of the system. They are used to calculate the flow orifice conductance C_{or} according to [16]

$$C_{or} = \frac{A_t \omega L_t}{\alpha \gamma p_{av}}, \tag{6.3.1}$$

where A_t is the cross section of the tube, ω is the angular frequency, L_t is the length of the tube, γ is the heat capacity ratio and p_{av} is the average pressure in the system. The double-inlet is used to reduce the flow resistance in the system to affect the final cooling power.

The cooling power at the third CHX and the corresponding lowest temperature determine the efficiency of the PTR. We are left with a problem with six degrees of freedom, namely the six orifice settings. To find the optimal values of these parameters we need to employ a sophisticated algorithm of optimisation. Alternatively, we can use a trial-and-error method to minimise the lowest temperature. This means that first the temperatures at the CHXs are assigned fixed values. These temperatures are initially much higher than the ones achieved (after much tuning) in the physical experiment. The cooling powers are then positive. We lower the temperatures in small steps using the same
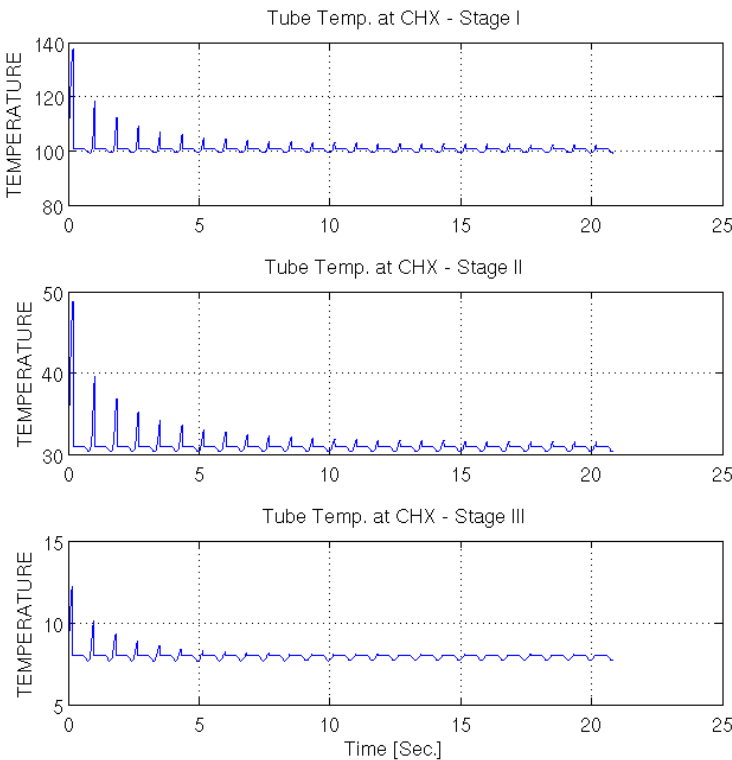
Figure 6.3: Cold end temperatures in the three-stage low-frequency PTR3-I (Trial-11).

orifice settings. The calculated cooling powers decrease too. Whenever we calculate negative cooling powers, we change the orifice settings to increase the cooling powers to values close to zero. This procedure is indeed cumbersome and normally it is not straightforward, because increasing or decreasing one parameter causes completely irregular result in the final cooling power which is not necessarily lower than that of the last case. The final calculated cooling power at each CHX is highly sensitive to modification of each of the six orifice settings. In addition, as the numerical experiments showed, the varied parameters have different contributions to the final cooling power for different PTR systems, i.e. they may be different and follow even multiple tracks for the low-frequency and high-frequency PTRs. Therefore, in this section, we only demonstrate the cooling power achieved by the low-frequency PTR3-I for a fixed number of orifice settings. See Table 6.3.

The main orifice settings α_1, α_2, α_3 are fixed such that almost zero net mass flow remains. The global behaviour of the system is very sensitive to changes in the double-inlet settings. Fig. 6.3 shows the temperature plots at three CHXs for a typical choice of the orifice settings (Trial-11) for which the second and the third CHX's almost zero cooling (heating) powers are -0.020 [W] and 6.0×10^{-4} [W]. The temperature histories show an initial unsteady transition period. To get an idea of the experimental temperatures at the CHXs: they were reported as $T_{C_1} = 79.5$ [K], $T_{C_2} = 26.1$ [K] and $T_{C_3} = 2.19$ [K] [67].

It is worth mentioning that in practice the cooling down process takes much longer time than in the simulation, because initially the whole system is at the ambient temperature. There are some other features, such as enthalpy loss due to non-adiabatic insulating chamber, non-ideal heat exchangers and wall effects, which make the process even longer to reach a low temperature at steady oscillatory state.

6.3.2   High frequency PTR3-II

We simulate the PTR3-II high-frequency system. The tubes are discretised in $N_{T_1} = 53$, $N_{T_2} = 193$, $N_{T_3} = 224$ points and the regenerators in $N_{R_1} = 51$, $N_{R_2} = 62$, $N_{R_3} = 55$ points so that Δz is identical in all regenerators and tubes. The time-step is $\Delta t = 0.1\Delta z$. Since we have a system with faster oscillating gas and shorter cycles, the CFL condition is taken stricter than in the low-frequency PTR. We define initial temperatures for the tubes and the regenerators in the same way as in the low-frequency system. We follow a trial-and-error method (as in Section 6.3.1) to find the optimal values of the orifice settings. Here, we calculate the three cooling powers in the high-frequency PTR3-II by changing the orifice settings. See Table 6.4. The trial simulations aim to find the lowest temperature at cooling powers approaching zero at all CHXs. The lowest temperature reached in this way is $T_{C_3} = 5.0$ [K] (Trial-35). Our simulations are based on assumptions and simplifications. Therefore, the final settings for such a high-frequency system in practice could be different. Nevertheless, the values suggested here may be reasonably good choices for the practical cases to start with. The simulations also indicate what is theoretically possible. Figure 6.4 shows the temperature versus cooling power plot for real gas. The orifice settings for these simulations are $\alpha_1 = 2.0$, $\alpha_2 = 2.5$, $\alpha_3 = 3.0$, $\alpha_{d_1} = 0.16$, $\alpha_{d_2} = 0.15$, $\alpha_{d_3} = 0.41$. A zero cooling power is computable and

occurs at about T = 8.35 [K]. Temperature and/or pressure dependent material properties together with real gas is crucial in such a range of temperature. Using real gas, it is not possible to reach temperatures lower than 7.0 [K] with these orifice settings, i.e. the simulation collapses after a couple of full cycles when specifying temperatures at CHX3 lower than 7.0 [K]. We need to find the optimal values of orifice settings for which the simulation stays stable, with no net mass flow and possibly with zero cooling power at CHX3. The optimal values of the orifice settings causing the lowest possible temperatures at CHX3 are listed in Table 6.4, which is the result of more than one thousand runs with different orifice settings and CHX temperatures.
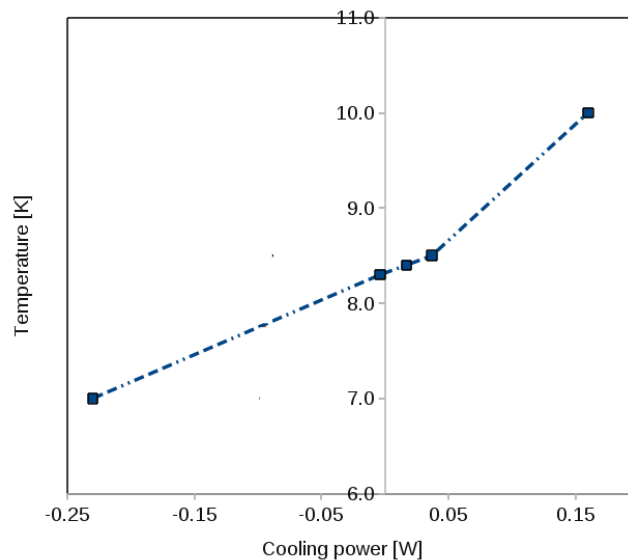
Figure 6.4: Temperature versus cooling power for real gas with temperature and/or pressure dependent material properties based on the orifice settings $\alpha_1 = 2.0$, $\alpha_2 = 2.5$, $\alpha_3 = 3.0$, $\alpha_{d_1} = 0.16$, $\alpha_{d_2} = 0.15$, $\alpha_{d_3} = 0.41$ (Trial-5).

In the remaining of this section the results of the PTR3-II simulation obtained in Trial-27 are discussed. Fig. 6.5 shows the pressure variations in the three buffers. The pressure variations are in phase and reach an oscillatory steady state ensuring zero net mass flow towards the buffers. This occurs after approximately 1.5 seconds.
Fig. 6.6 and Fig. 6.7 show the velocities and pressures at different positions for all three stages during gas oscillation. The small pressure drop is caused by the combined resistance of the regenerators and the double-inlets. Using double-inlets reduces the dissipation in the regenerator which causes the pressure drop to be lower than in the case without double-inlets. The velocity decrease is caused by the compressibility and

Test-case	α_1 [-]	α_2 [-]	α_3 [-]	α_{d_1} [-]	α_{d_2} [-]	α_{d_3} [-]	T_{C_1} [K]	T_{C_2} [K]	T_{C_3} [K]	Q_{L_1} [W]	Q_{L_2} [W]	Q_{L_3} [W]
Trial-1	2.0	2.5	3.0	0.16	0.15	0.41	100	25	10	2.61	1.57	0.16
Trial-2	2.0	2.5	3.0	0.16	0.15	0.41	100	25	7	3.1	2.3	-0.23
Trial-3	2.0	2.5	3.0	0.16	0.15	0.41	100	25	8.5	2.84	1.93	0.037
Trial-4	2.0	2.5	3.0	0.16	0.15	0.41	100	25	8.4	2.85	1.96	0.017
Trial-5	2.0	2.5	3.0	0.16	0.15	0.41	100	25	8.3	2.87	1.99	-0.0036
Trial-6	2.0	2.5	3.0	0.2	0.2	0.2	75	25	6.0	4.0	-3.0	-6.0
Trial-7	2.0	2.5	3.0	0.15	0.16	0.35	60	15	6.0	1.71	1.27	-0.2
Trial-8	2.0	2.5	3.0	0.14	0.15	0.38	60	15	6.0	-1.1	0.47	-0.16
Trial-9	2.0	2.5	3.0	0.11	0.13	0.42	65	18	5.0	-4.50	0.02	-0.17
Trial-10	2.0	2.5	3.0	0.13	0.125	0.44	65	18	5.0	-7.30	-1.47	-0.21
Trial-11	2.0	2.5	3.0	0.15	0.15	0.45	75	20	5.0	2.03	1.84	-1.15
Trial-12	2.0	2.5	3.0	0.15	0.15	0.48	73	18	5.0	0.24	1.25	-0.15
Trial-13	2.0	2.5	3.0	0.14	0.15	0.48	73	18	5.0	0.36	1.59	-0.15
Trial-14	2.0	2.5	3.0	0.16	0.15	0.48	73	18	5.0	0.083	1.10	-0.148
Trial-15	2.0	2.5	3.0	0.16	0.16	0.48	73	18	5.0	2.60	2.0	-0.13
Trial-16	2.0	2.5	3.0	0.16	0.14	0.48	73	18	5.0	-3.20	-0.09	-0.18
Trial-17	2.0	2.5	3.0	0.16	0.1415	0.48	75	18	5.0	-2.11	0.91	-0.13
Trial-18	2.0	2.5	3.0	0.15	0.145	0.48	80	16	4.5	-4.38	0.10	-0.12
Trial-19	1.5	2.5	3.0	0.15	0.145	0.48	80	16	4.5	-5.20	-0.53	-0.13
Trial-20	2.5	2.5	3.0	0.15	0.145	0.48	80	16	4.5	-4.50	0.107	-0.13
Trial-21	3.0	3.5	4.0	0.15	0.145	0.48	80	16	4.5	-8.90	-2.0	-0.18
Trial-22	2.5	2.9	3.5	0.15	0.145	0.48	80	16	4.5	-6.30	-1.01	-0.15
Trial-23	2.3	2.8	3.2	0.15	0.145	0.48	82	17	4.5	-4.70	-0.09	-0.13
Trial-24	1.9	2.75	2.9	0.15	0.145	0.48	82	17	4.5	-5.60	0.025	-0.13
Trial-25	2.0	2.5	3.0	0.16	0.16	0.35	74	15	4.5	1.68	1.58	-0.106
Trial-26	2.0	2.5	3.0	0.16	0.16	0.51	78	18	4.5	1.82	2.75	-0.10
Trial-27	2.0	2.5	3.0	0.16	0.16	0.46	78	16	4.5	0.92	2.29	-0.08
Trial-28	2.0	2.5	3.0	0.16	0.16	0.41	78	16	4.5	1.34	2.21	-0.08
Trial-29	2.0	2.5	3.0	0.16	0.16	0.38	71	13	4.5	-1.11	1.03	-0.077
Trial-30	2.0	2.5	3.0	0.16	0.16	0.4	75	15	4.5	0.68	1.67	-0.07
Trial-31	2.0	2.5	3.0	0.16	0.15	0.48	80	17	5.0	-1.1	0.93	-0.14
Trial-32	2.0	2.5	3.5	0.16	0.15	0.48	80	17	5.0	-0.57	-0.31	-0.13
Trial-33	2.0	2.5	4.0	0.16	0.15	0.48	80	17	5.0	-0.18	-0.15	-0.12
Trial-34	2.0	2.5	4.5	0.16	0.15	0.48	80	17	5.0	-1.8	-0.7	-0.13
Trial-35	2.0	1.5	4.5	0.16	0.15	0.48	75	17	5.0	7.04	0.51	-0.086
Trial-36	1.2	1.0	4.5	0.16	0.15	0.48	70	17	5.0	12.92	0.6	-0.047
Trial-37	1.2	1.0	4.5	0.12	0.15	0.48	70	17	5.0	8.83	-1.95	-0.017
Trial-38	1.2	1.0	4.5	0.50	0.15	0.48	70	17	5.0	10.1	-1.23	-0.017
Trial-39	1.2	1.0	4.5	0.80	0.15	0.48	70	17	5.0	9.34	-1.67	-0.015
Trial-40	1.2	1.0	5.0	0.80	0.15	0.48	70	17	5.0	9.60	-1.89	0.0003

Table 6.4: Cooling powers calculated at three junctions with three given CHX temperatures based on six orifice settings for PTR3-II; α_i: main orifice settings, α_{d_i}: double-inlet settings, T_{C_i}: cold end temperatures at CHXs, Q_{L_i}: cooling power at the junctions.
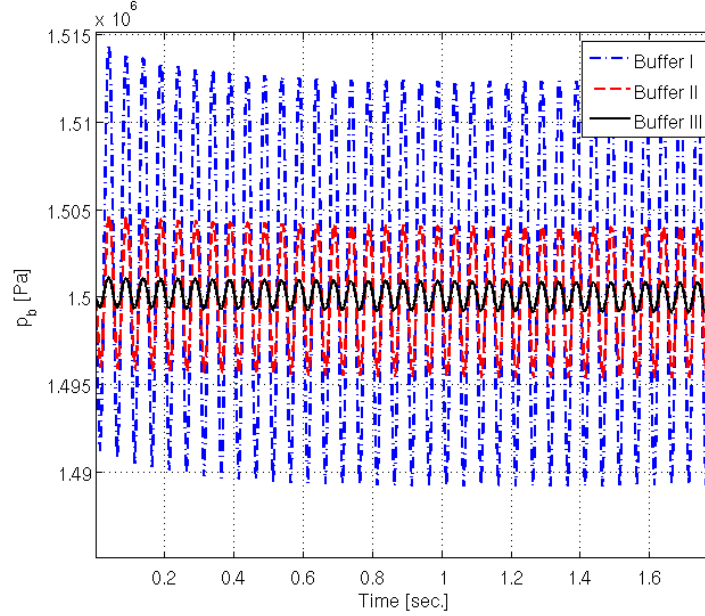
Figure 6.5: Buffer pressure variations for the first 1.75 [sec].

the decrease of temperature and pressure per tube. Due to the specified orifice settings, the velocity amplitudes in tube II are almost twice larger than those in tube I and tube III. See Fig. 6.6. The velocity amplitudes are based on the volume flows assigned at the hot ends of tubes. The main boundary condition for the velocity is the one at the tube's hot end and the volume flow at each tube's hot end is computed by (3.2.56). This relation represents the proportionality of the volume flow to the pressure differences between the tube and the buffer (first term) together with the pressure difference between the compressor and the tube (second term), which are multiplied by the conductance of the main orifices and the double-inlets, respectively. All these variables are depending on each other so that we cannot choose one orifice setting in such a way that the pressure amplitude does not change. Therefore, we can expect different situations for the velocity amplitudes by changing the orifice settings. Here the conductance of the three main orifices are $C_{or_1} = 1.0079 \times 10^{-8} [m^3/Pa.s]$, $C_{or_2} = 2.9742 \times 10^{-9} [m^3/Pa.s]$, $C_{or_3} = 6.8606 \times 10^{-10} [m^3/Pa.s]$, and the conductance of the three double-inlets are $C_{di_1} = 1.0079 \times 10^{-8} [m^3/Pa.s]$, $C_{di_2} = 2.9742 \times 10^{-9} [m^3/Pa.s]$, $C_{di_3} = 6.8606 \times 10^{-10} [m^3/Pa.s]$.

The velocity amplitudes at the cold end of the regenerators I and II indicated as R-Cold I and R-Cold II, respectively, in Fig. 6.6 are decreasing with the distance from the compressor due to the resistance of the porous media. This is more crucial in the third stage where the velocity amplitude is very low. Consequently, according to Darcy's law, this causes the pressure gradient in the third regenerator to be very low. As Fig. 6.7 shows, the pressure amplitudes at both sides of the regenerator III are almost the same, i.e. the
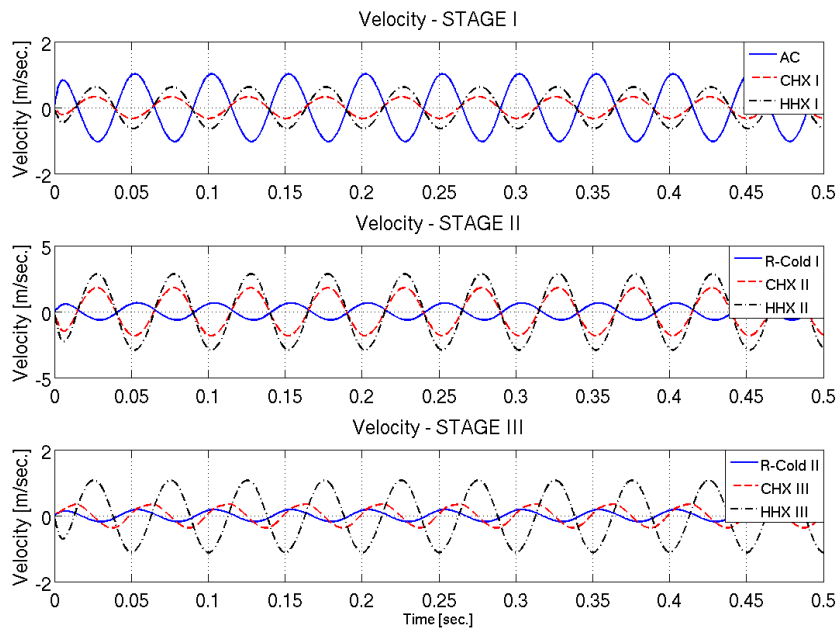
Figure 6.6: Velocity variations in the three-stage PTR.

pressure gradient is almost negligible. This is caused by the short length of the third regenerator and small velocity amplitude. Of course, by changing the orifice settings we may attain different values.

Fig. 6.8 gives the temperatures at the cold ends of the tubes. There are transition times in which the influence of the initial conditions damps out. The temperature profiles attain oscillatory steady state after about 60 cycles, but this can be hugely different in practical cases where the cooling down is from room temperature.

The net mass flows in the tubes per cycle are about 1.15×10^{-8} [kg/s], 3.8×10^{-9} [kg/s] and 4.8×10^{-8} [kg/s], which is to be compared with mass flow amplitudes of the order of 10^{-4} [kg/s] at the middle of the tubes. It means that net mass transport has almost vanished. Of course, based on the numerical errors due to the applied discretisation method we may get net mass flow in the simulation after a very long time. The calculated averaged enthalpy flow (6.2.3) after 7.5 [sec] is 3.20 [W], 1.35 [W] and 0.57 [W] for the first, the second and the third tube, respectively. The corresponding roughly estimated values (6.2.5) are 2.80 [W], 0.71 [W] and 0.39 [W]. The calculated enthalpy and mass flows in the three tubes are shown in Fig. 6.10 and 6.11 respectively. Remark: the average enthalpy is not zero, i.e. $\overline{H} \neq 0$ and the average mass flow is almost zero, i.e. $\overline{\dot{m}} \neq 0$, though both show similar behaviour.
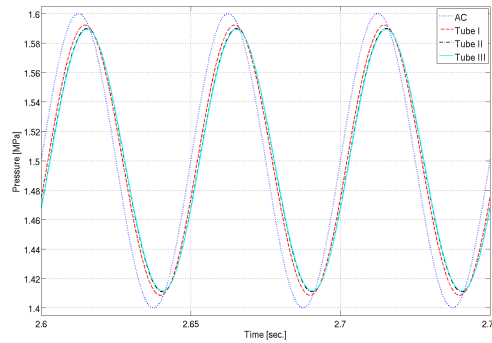
Figure 6.7: Pressure variations in the three-stage PTR3-II during three full cycles.

6.4 Conclusion

We simulated two different three-stage double-inlet PTRs, one existing laboratory system operating at low frequency to qualitative verify our code and the other one operating at high frequency as stated in the final goal of this project. The numerical results obtained for a real gas are in terms of velocity, density and gas and solid temperatures. The pressure and temperature dependent material properties of gas and solids are taken into account because these are significant in the very low temperature range reached in the third regenerator and tube. The method employed here to attain physically steady results is based on three pre-assigned temperatures at the CHXs. This means we are left with an optimisation problem of nine degrees of freedom, namely six orific settings and three cold temperatures. The calculated cooling power at each CHX is highly sensitive to modification of each of the six orifice settings. As the numerical experiments showed, the varied parameters have different contributions to the final cooling power for different PTR systems, i.e. they may be different and follow even multiple tracks for the low-frequency and high-frequency PTRs. Therefore, in our investigation, we only demonstrated the cooling power achieved by the low-frequency PTR3-I for a fixed number of orifice settings and we focused on finding the optimal orifice values for the high-frequency PTR to reach the lowest possible temperature. Our numerical simulations showed that the settings of the three main orifices and the three double-inlets are crucial in finding the lowest possible temperature. We were able to cool down to 5 K.

Finally, the developed software provides a tool for estimating the essential parameters of cooling systems, such as temperature, velocity, mass flow, enthalpy flow, which leads to a deeper understanding of heat transfer, fluid-wall interaction, boundary layers, etc. It is a suitable platform to optimise a three-stage PTR in terms of geometry, pressure amplitude (input power), and material properties, so to reach the lowest possible temperature or to gain the highest coefficient of performance.
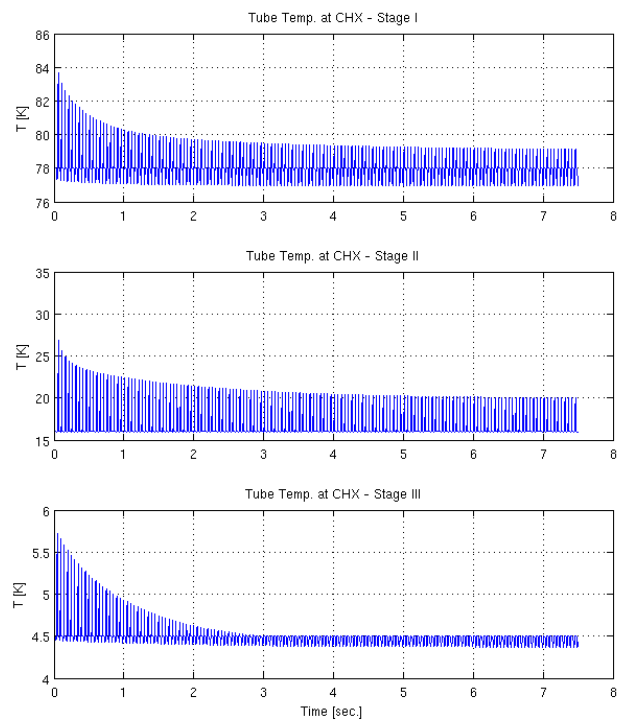
Figure 6.8: Cold end temperatures in the three-stage PTR.
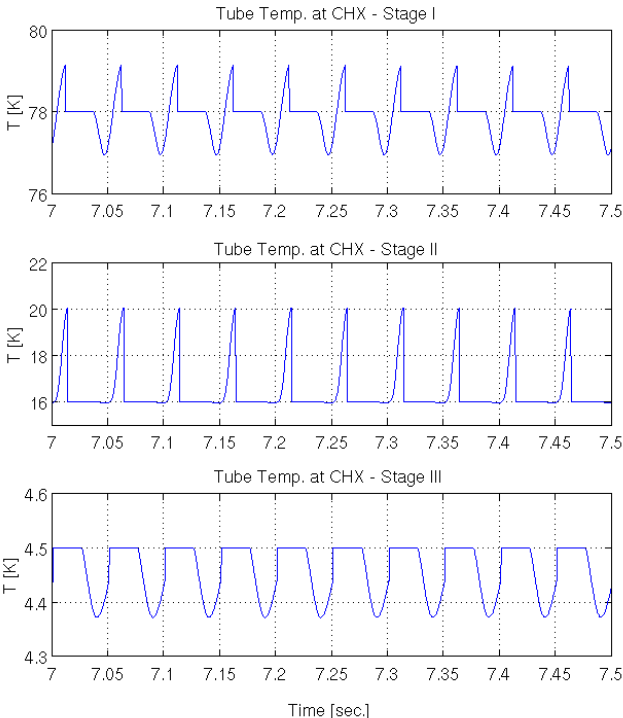
Figure 6.9: Zoom on the CHXs' temperatures for the last 10 cycles of Fig. 6.8.
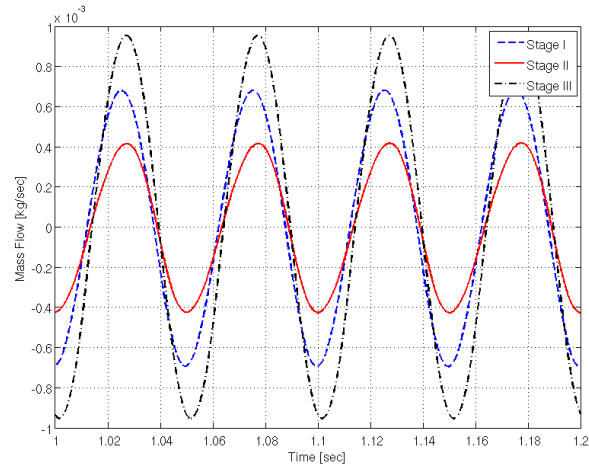
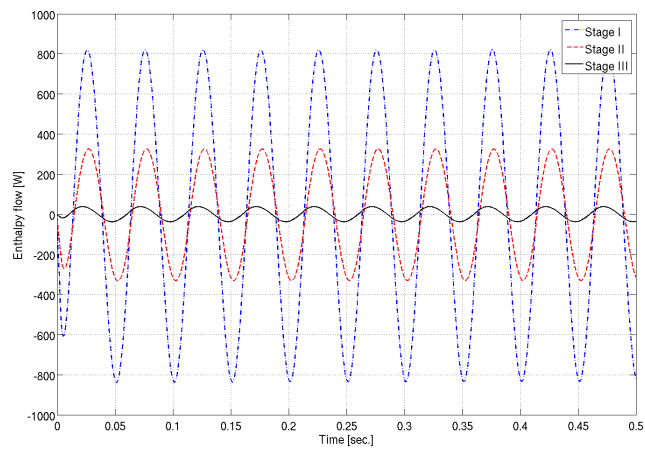Figure 6.10: Mass flow in the middle of the three tubes.

Figure 6.11: Enthalpy flows in middles of three pulse tubes.

Chapter 7

Conclusions and recommendations

The development of an accurate mathematical model and an efficient numerical method to simulate a three-stage PTR operating at high frequencies was the final goal of the project. To accomplish this mission we first improved and extended an existing single-stage model both in 1D and 2D. The improvements included correcting small mistakes and enhancing the accuracy and efficiency of the computation. The extension was the modeling of the regenerator.

The general design and operation of multi-stage PTRs was explained and the physical benefit of a double-inlet described. The necessary temperature and pressure dependent material properties of helium and of the regenerator solid were formulated. We derived a mathematical model describing the fluid flow and heat transfer in PTRs. The flow was shown to be laminar for the systems considered in the Chapters 5 and 6. The heat exchangers were assumed to operate ideally. One-dimensional formulations for the pulse-tube and the regenerator with connecting interface conditions were given. A two-dimensional formulation was derived for the pulse-tube (including solid wall) allowing the investigation of wall effects due to heat transfer and skin friction.

One new item in the modelling of multi-stage PTRs was the use of non-ideal (Van der Waals) gas so that a more realistic behaviour at extremely low temperatures was obtained. Proper junction conditions were formulated based on the local conservation of mass, momentum and energy.

The domain of computation in 2D was of simple cylindrical shape and therefore a finite-difference (FD) method has been used to discretise the equations. The new component here is the domain decomposition (DD) technique that hugely improved the efficiency of the 2D computation of the tube. The storage of data and computations were done with smaller systems than in the case of an entirely uniform grid. We only needed to deal with a structured A-matrix which has big advantages compared with tensor grids [48]. In addition, much larger time steps were allowed because of a less restrictive CFL condition in comparison with that of the tensor grid.

One single-stage and two different three-stage double-inlet PTRs have been simulated and analysed. The cooling power at each CHX in the three-stage machines appeared to be highly sensitive to each of the six varied orifice settings. Nevertheless, the simulated high-frequency machine was able to cool down to 5 K.

A working tool for simulating single- and multi-stage PTRs has been developed. The software can be improved in several ways, for example through a more realistic modelling of the heat exchangers. The 2D simulation of multi-stage PTRs has not been carried out in this project, but would be a logical next step, knowing that the applied DD method guarantees computational efficiency. The biggest challenge however is the development of a smart optimisation algorithm.

Appendix A

Analytical solution

In this appendix an analytical solution is obtained for the 1D pulse tube assuming inviscid flow without heat conduction. Fluid viscosity, thermal conductivity and heat exchange with the wall are ignored in the momentum equation (3.2.8) and energy equation (3.2.9).

A.1   Governing equations

The pressure is uniform in space and the energy equation simplifies to

$$\frac{\partial p}{\partial z} = 0, \tag{A.1.1}$$

$$\rho c_p \left(\frac{\partial T}{\partial t} + u \frac{\partial T}{\partial z} \right) = \frac{dp}{dt}, \tag{A.1.2}$$

We have then two equations for two unknowns velocity u and temperature T. The pressure p is given as a function of time and the density ρ is computed by

$$\rho = p/(R_m T). \tag{A.1.3}$$

The following exact solutions are obtained when using the method of characteristics

Pressure: $$p(t) = p_{av} + \bar{p}\sin(\omega t), \tag{A.1.4}$$

Velocity: $$u(z, t) = \frac{-1}{\gamma} \frac{d}{dt} \ln(p(t))z + u(z_0, t), \tag{A.1.5}$$

Displacement:
$$z(z_0, t_0, t) = \int_{t_0}^{t} u_0(\tau) \left(\frac{p(\tau)}{p(t)} \right)^{\frac{1}{\gamma}} d\tau + z_0 \left(\frac{p(t_0)}{p(t)} \right)^{\frac{1}{\gamma}}, \qquad (A.1.6)$$

Temperature:
$$T(z_0, t_0, t) = T(z_0, t_0) \left(\frac{p(t_0)}{p(t)} \right)^{1 - \frac{1}{\gamma}}, \qquad (A.1.7)$$

Density:
$$\rho(z_0, t_0, t) = \frac{p(t)}{R_m T(z_0, t_0, t)}. \qquad (A.1.8)$$

where z_0, t_0, u_0 are the initial position, time and velocity of the gas at a certain point on the boundary of the z-t domain.

Appendix B

Physical data

B.1 Single-stage Pulse-Tube Refrigerator

The material properties of gas and regenerator material, of the simulated single-stage PTR in this study are listed in Table B1 with the corresponding dimensionless values in Table B.2.

B.2 Three-stage Pulse-Tube Refrigerator.

The geometrical and material properties of the three-stage PTR simulated in this study are listed in Tables B.3-B.7. The values correspond to a machine built in the Department of Applied Physics.

Symbol	Definition	Value
fr	frequency	20 Hz
ω	angular frequency	125.66 s^{-1}
$\bar{\rho}$	gas density	4.7 kg m^{-3}
$\bar{u}$	gas velocity	1.0 m s^{-1}
$\bar{\mu}$	viscosity	$2.0 \times 10^{-5} \text{ Pa s}$
$\bar{k}_g$	gas thermal conductivity	$1.58 \times 10^{-1} \text{ W m}^{-1} \text{ K}^{-1}$
$\bar{c}_g$	gas specific heat capacity	$5.2 \times 10^3 \text{ J kg}^{-1}\text{K}^{-1}$
$\bar{p}$	pressure oscillation amplitude	$5 \times 10^5 \text{ Pa}$
p_{av}	average pressure	$3 \times 10^6 \text{ Pa}$
T_a	ambient temperature	300 K
R_m	specific gas constant	$2.1 \times 10^3 \text{ J kg}^{-1}\text{K}^{-1}$
A_t	cross-sectional area of tube	$1.96 \times 10^{-3} \text{ m}^2$
C_{or}	flow conductance of the orifice	$10^{-8} \text{ m}^3 \text{ Pa}^{-1}\text{s}^{-1}$
L_t	length of tube	0.2 m
L_r	length of regenerator	0.2 m
T_H	hot end temperature	300 K
T_C	cold end temperature	60 K
V_b	buffer volume	10^{-3} m^3
ϕ	porosity	0.7
κ	permeability	$3.2 \times 10^{-10} \text{ m}^2$
β	heat transfer coefficient	$9 \times 10^7 \text{ W m}^{-3}\text{K}^{-1}$
ρ_r	regenerator material density	$7.8 \times 10^3 \text{ kg m}^{-3}$
$\bar{c}_r$	regenerator specific heat capacity	$400 \text{ J kg}^{-1} \text{ K}^{-1}$
$\bar{k}_r$	regenerator thermal conductivity	$1.5 \text{ W m}^{-1} \text{ K}^{-1}$

Table B.1: Physical data for the simulated single-stage pulse-tube refrigerator (material properties at 300 K).

Symbol	Definition	Typical Value (fr = 20 [Hz])
Re	$\bar{\rho}\bar{u}^2/\bar{\mu}\omega$	1.87×10^3
Ma	$\bar{u}/(p_{av}/\bar{\rho})^{1/2}$	1.3×10^{-3}
Pr	$c_p\bar{\mu}/\bar{k}_g$	0.66
Pe_g	$RePr$	1.231×10^3
Pe_r	$\rho_r\bar{c}_r\bar{u}^2/\bar{k}_r\omega$	4.965×10^3
$\mathcal{A}$	$\bar{p}/p_{av}$	0.1667
$\mathcal{B}$	$p_{av}/\bar{\rho}R_mT_a$	1.0132
$\mathcal{C}$	$C_{or}p_{av}/A_t\bar{u}$	15
$\mathcal{D}$	$k\overline{\mu u}^2/\phi p_{av}\omega k$	2.2×10^{-4}
$\mathcal{E}_0$	$\bar{p}_b/p_{av}$	1.008
γ	c_g/c_v	5/3
β_g^*	$\beta/\overline{\rho}c_g\phi\omega$	46.51
β_r^*	$\beta/\rho_r\bar{c}_r(1-\phi)\omega$	0.8502

Table B.2: Dimensionless parameters for the simulated single-stage pulse-tube refrigerator.

Table B.3: Geometrical properties.

Symbol	Definition	Value
d_{t1}	diameter of the 1st tube	24.6 mm
d_{t2}	diameter of the 2nd tube	7 mm
d_{t3}	diameter of the 3rd tube	5 mm
d_{r1}	diameter of the 1st regenerator	72 mm
d_{r2}	diameter of the 2nd regenerator	32 mm
d_{r3}	diameter of the 3rd regenerator	19 mm
L_{t1}	length of the 1st tube	67.5 mm
L_{t2}	length of the 2nd tube	246 mm
L_{t3}	length of the 3rd tube	285 mm
L_{r1}	length of the 1st regenerator	65 mm
L_{r2}	length of the 2nd regenerator	78.5 mm
L_{r3}	length of the 3rd regenerator	70 mm
V_{b1}	1st buffer volume	10^{-3} m^3
V_{b2}	2nd buffer volume	10^{-3} m^3
V_{b3}	3rd buffer volume	10^{-3} m^3

Table B.4: Regenerator material properties.

Symbol	Definition	Value
Material kind	1st regenerator	stainless steel
Material kind	2nd regenerator	lead
Material kind	3rd regenerator	ErNi
$\bar{c}_r$	reg. specific heat capacity	400 J kg^{-1} K^{-1}
κ	reg. permeability	3.0×10^{-11} m^2
$\bar{k}_g$	gas thermal conductivity	1.58×10^{-1} W m^{-1} K^{-1}
$\bar{k}_{r1}$	1st reg. thermal conductivity	10 W m^{-1} K^{-1}
$\bar{k}_{r2}$	2nd reg. thermal conductivity	5 W m^{-1} K^{-1}
$\bar{k}_{r3}$	3rd reg. thermal conductivity	5 W m^{-1} K^{-1}
ρ_{r1}	1st reg. density	7800 kg m^{-3}
ρ_{r2}	2nd reg. density	11350 kg m^{-3}
ρ_{r3}	3rd reg. density	9400 kg m^{-3}
ϕ_1	1st reg. porosity	0.682
ϕ_2	2nd reg. porosity	0.6
ϕ_3	3rd reg. porosity	0.6
β	reg. heat transfer coefficient	10^8 W m^{-3} K^{-1}

Table B.5: ^{4}He properties.

Symbol	Definition	Value
c_p	gas specific heat capacity	5.2×10^3 J kg^{-1}K^{-1}
$\bar{p}$	pressure oscillation amplitude	510^4 Pa
p_{av}	average pressure	1.5×10^6 Pa
R	gas constant	8.4 J mol^{-1}K^{-1}
R_m	specific gas constant	2.1×10^3 J kg^{-1}K^{-1}
T_a	ambient temperature	300 K
T_H	hot temperature	300 K
$\bar{u}$	gas velocity	1.0 m s^{-1}
$\bar{\rho}$	gas density	4.7 kg m^{-3}
$\bar{\mu}$	gas dynamic viscosity	10^{-5} Pa s
a	Van der Waals coefficient	3.47×10^{-3} m^{6}Pa mol^{-2}
b	Van der Waals coefficient	2.37×10^{-5} m^3 mol^{-1}

Table B.6: Compressor and orifice settings.

Symbol	Definition	Value
fr	frequency	$20 \, \text{s}^{-1}$
ω	angular frequency	$125.66 \, \text{s}^{-1}$
α	orifice setting parameter [15]	1
C_{or1}	$L_{t1}\omega/\gamma\alpha\bar{u}$	$1.21^{-9} \, \text{m}^3 \, \text{Pa}^{-1}\text{s}^{-1}$
C_{or2}	$L_{t2}\omega/\gamma\alpha\bar{u}$	$3.57^{-10} \, \text{m}^3 \, \text{Pa}^{-1}\text{s}^{-1}$
C_{or3}	$L_{t3}\omega/\gamma\alpha\bar{u}$	$2.11^{-10} \, \text{m}^3 \, \text{Pa}^{-1}\text{s}^{-1}$

Table B.7: Dimensionless numbers and values.

Symbol	Definition	Value (fr = 20 [Hz])
Ma	$\bar{u}/(p_{av}/\bar{\rho})^{1/2}$	1.5×10^{-3}
Re	$\bar{\rho}\bar{u}^2/\bar{\mu}\omega$	1.87×10^3
$\mathcal{A}$	$\bar{p}/p_{av}$	0.05
$\mathcal{B}$	$p_{av}/\bar{\rho}R_mT_a$	0.675
$\mathcal{C}_1$	$C_{or1}p_{av}/A_{t1}\bar{u}$	5.089
$\mathcal{C}_2$	$C_{or2}p_{av}/A_{t2}\bar{u}$	18.553
$\mathcal{C}_3$	$C_{or3}p_{av}/A_{t3}\bar{u}$	21.49
$\mathcal{D}$	$\bar{\mu}\bar{u}^2/\phi p_{av}\omega k$	2.2×10^{-3}
$\mathcal{E}$	$\beta/\bar{\rho}c_g\phi\omega$	47.74
$\mathcal{E}_0$	$\bar{p}_b/p_{av}$	1.0008
$\mathcal{EF}$	$\beta/[\rho_r\bar{c}_r(1-\phi)\omega]$	1.604
Pe_{r1}	$\rho_{r1}\bar{c}_r\bar{u}^2/\bar{k}_{r1}\omega$	1.24×10^3
Pe_{r2}	$\rho_{r2}\bar{c}_r\bar{u}^2/\bar{k}_{r2}\omega$	1.806×10^3
Pe_{r3}	$\rho_{r3}\bar{c}_r\bar{u}^2/\bar{k}_{r3}\omega$	0.748×10^3
Pe_g	$\rho_g\bar{c}_g\bar{u}^2/\bar{k}_g\omega$	1.231×10^3
γ	c_g/c_v	5/3
Subscripts		
b	buffer	
C	cold end	
H	hot end	
g	gas	
r	regenerator	
t	tube	

Bibliography

[1] R. Akhavan, R. D. Kamm, and A. H. Shapiro. An investigation of transition to turbulence in bounded oscillatory Stokes flows, part i: Experiments. *Journal Fluid Mech*, 225:395–422, 1991.

[2] D. C. Arney and J. E. Flaherty. An adaptive local mesh refinement method for time dependent partial differential equations. *Appl. Numerical Mathematics*, 5:257–274, 1989.

[3] S. H. Baek, E. S. Jeong, and S. Jeong. Two-dimensional model for tapered pulse tubes. part 1: theoretical modeling and net enthalpy flow. *Cryogenics*, 40:379–385, 2000.

[4] S. H. Baek, E. S. Jeong, and S. Jeong. Two-dimensional model for tapered pulse tubes. part 2: mass streaming and streaming-driven enthalpy flow loss. *Cryogenics*, 40:387–392, 2000.

[5] Y. P. Banjare, R. K. Sahoo, and S. K. Sarangi. CFD simulation of a Gifford–Mcmahon type pulse tube refrigerator. *International Journal of Thermal Sciences*, pages 1–8, 2009.

[6] M. J. Berger and P. Colella. Local adaptive mesh refinement for shock hydrodynamics. *Journal of Computational Physics*, 82:64–84, 1989.

[7] G. J. Brereton and R. R. Mankbadi. Review of recent advances in the study of unsteady turbulent internal flows. *ASME, Appl Mech Rev*, 148:189–212, 1995.

[8] P. C. T. de Boer. Thermodynamic analysis of the basic pulse-tube refrigerator. *Cryogenics*, 34:699–711, 1994.

[9] A. T. A. M. de Waele. Regenerator dynamics in the harmonic approximation. *Cryogenics*, 38:995–1006, 1998.

[10] A. T. A. M. de Waele. Optimization of pulse tubes. *Cryogenics*, 39:13–15, 1999.

[11] A. T. A. M. de Waele. Pulse-tube refrigerators: principle, recent developments and prospects. *Physica B, Condensed Matter*, 280:479–482, 2000.

[12] A. T. A. M. de Waele. Regenerator dynamics in the harmonic approximation ii. *Cryogenics*, 41:195–200, 2001.

[13] A. T. A. M. de Waele. *Values of material properties*. Eindhoven university of Technology, 2002.

[14] A. T. A. M. de Waele. *Helium properties*. Eindhoven university of Technology, 2006.

[15] A. T. A. M. de Waele, P. P. Steijaert, and J. Gijzen. Thermodynamical aspects of pulse tubes. *Cryogenics*, 37:313–324, 1997.

[16] A. T. A. M. de Waele, P. P. Steijaert, and J. J. Koning. Thermodynamical aspects of pulse tubes ii. *Cryogenics*, 38:329–335, 1998.

[17] A. T. A. M. de Waele, I. A. Tanaeva, and Y. L. Yu. Multistage pulse tubes. *Cryogenics*, 40:459–464, 2000.

[18] A. T. A. M. de Waele, M. Y. Xu, and Y. L. Ju. Nonideal-gas effect in regenerators. *Cryogenics*, 39:847–851, 1999.

[19] A. T. A. M. de Waele, M. Y. Xu, and Y. L. Ju. Pulse tube performance at very low temperatures. *Physica B, Condensed Matter*, 284:2018–2019, 2000.

[20] B. Y. Du, L. W. Yang, J. H. Cai, and J. T. Liang. Numerical simulation of a regenerator in a two-stage pulse tube refrigerator. In S. D. Miller and R. G. Ross, editors, *Cryocoolers 14*, pages 405–409, 2007.

[21] E. R. G. Eckert and R. M. Drake. *Analysis of Heat and Mass Transfer*. McGraw-Hill, NewYork, 1972.

[22] D. M. Eckmann and J. B. Grotberg. Experiments on transition to turbulence in oscillatory pipe flow. *Journal Fluid Mech*, 222:329–350, 1991.

[23] M. A. Etaati, R. M. M. Mattheij, A. S. Tijsseling, and A. T. A. M. De Waele. One-dimensional analytical and numerical models of pulse-tube coolers. In *Proceedings of ICC14 Conference*, pages 301–306, Maryland, USA, 2006.

[24] M. A. Etaati, R. M. M. Mattheij, A. S. Tijsseling, and A. T. A. M. De Waele. One-dimensional numerical simulation of the Stirling-type pulse-tube refrigerator. In *Proceedings of ICFD Conference on Numerical Methods for Fluid Dynamics*, Reading, UK, 2007.

[25] M. A. Etaati, R. M. M. Mattheij, A. S. Tijsseling, and A. T. A. M. De Waele. One-dimensional simulation of a Stirling three-stage pulse-tube refrigerator. In *Proceedings of the Heat Transfer Conference, ASME*, San Fransisco, USA, 2009. ASME, HT2009-88087.

[26] R. E. Ewing. Adaptive grid refinement for transient flow problems. In J. E. Flaherty, P. J. Paslow, M. S. Shephard, and J. D. Vasilakis, editors, *Adaptive Methods for Partial Differential Equations*, pages 194–205, Philadelphia, 1989. SIAM.

[27] J. E. Flaherty, P. K. Moore, and C. Ozturan. Adaptive overlapping grid methods for parabolic systems. In J. E. Flaherty, P. J. Paslow, M. S. Shephard, and J. D. Vasilakis, editors, *Adaptive Methods for Partial Differential Equations*, pages 176–193, Philadelphia, 1989. SIAM.

[28] K. Frederix. Numerical simulation of streaming in pulse-tube refrigerators. Master's thesis, Eindhoven University of Technology, Department of Mathematics and Computer Science, Eindhoven, the Netherlands, 2006. In English.

[29] D. Gedeon. Sage: object orientated software for stirling-type machine design. In American Institute for Aeronautics and Astonautics, editors, *Proceeding of the 29th intersociety energy conversion and engineering conference vol. 4*, pages 1902–1907. Monterey, CA, USA, 1994.

[30] W. E. Gifford and R. C. Longsworth. Pulse tube refrigeration. *Trans. ASME*, 86:264–268, 1964.

[31] S. F. Grace. Oscillatory motion of viscous liquid in a long straight tube. *The London, Edinburgh and Dublin Philosophical Magazine and J. of Science*, 31:933–939, 1928.

[32] I. B. Grandall. Theory of vibrating systems and sound. *New York: Van Nostrand. Appendix A*, 1926.

[33] W. D. Gropp and D. E. Keyes. Domain decomposition with local mesh refinement. *SIAM J. Sci. Stat. Comput.*, 13:967–993, 1992.

[34] M. Hino, M. Kashiwayanagi, M. Nakayama, and T. Hara. Experiments on the turbulent statistics and the structure of a reciprocating oscillatory flow. *Journal Fluid Mech*, 131:363–400, 1983.

[35] H. W. G. Hooijkaas. *Miniature Stirling-type pulse-tube refrigerators*. PhD thesis, Eindhoven University of Technology, Eindhoven, The Netherlands, 2000.

[36] H. W. G. Hooijkaas and Benschop. A. A. J. Pulse tube development using harmonic simulations. In R. G. Ross, editor, *Cryocoolers 10*, pages 359–367. Jr. Plenum Press New York, 1999.

[37] Y. Hozumi, M. Shiriaishi, and M. Murakami. Simulation of thermodynamics aspects about pulse tube refrigerator. *Advances in Cryogenic Engineering*, 49:1500–1507, 2004.

[38] F. P. Incropera and D. P. DeWitt. *Fundamentals of Heat and Mass Transfer, 4th edition*. John Wiley and Sons Inc., 1996.

[39] A. Iserles. *A first course in Numerical analysis of differential equations*. Cambridge university press, NewYork, 2006.

[40] M. Jakob. *Heat Transfer*. John Wiley and Sons, NewYork, 1949.

[41] Y. L. Ju. Computational study of a 4 k two-stage pulse tube cooler with mixed Eulerian-Lagrangian method. *Cryogenics*, 41:49–57, 2001.

[42] Y. L. Ju, C. Wang, and Y. Zhou. Numerical simulation and experimental verification of the oscillating flow in pulse tube refrigerator. *Cryogenics*, 38:169–176, 1998.

[43] Kaiser, G. and Brehm, H. and Thürk, M. and Seidel, P. Thermodynamic analysis of an ideal fourvalve pulse tube refrigerator. *Cryogenics*, 36:527–533, 1996.

[44] W. M. Kays. *Compact Heat Exchangers*. McGraw-Hill, NewYork, 1955.

[45] R. Klein, N. Botta, T. Schneider, C. D. Munz, S. Roller, A. Meister, L. Hoffmann, T. Sonar, and W. E. Stewart. Asymptotic adaptive methods for multi-scale problems in fluid mechanics. *Journal of Engineering Mathematics*, 39:261–343, 2001.

[46] J. W. L. Kohler and C. O. Jonkers. Fundamentals of the gas refrigeration machine. *Philips Tech. Rev.*, 16:69–78, 1954.

[47] J. M. Lee and P. Kittel. Simple two-dimensional corrections for one-dimensional pulse-tube models. In R. G. Ross, editor, *Cryocoolers 10*, pages 351–358. Jr. Plenum Press New York, 1999.

[48] I. A. Lyulina. *Numerical simulation of pulse-tube refrigerators*. PhD thesis, Eindhoven University of Technology, Eindhoven, the Netherlands, 2005.

[49] I. A. Lyulina, R. M. M. Mattheij, A. S. Tijsseling, and A. T. A. M. de Waele. Numerical simulation of pulse-tube refrigerators, in 1D model. In H. C. de Lange et al., editor, *Eurotherm Seminar, vol.74, ISBN 90-386-2954-0*, pages 91–97, Eindhoven, The Netherlands, 2003. Technische Universiteit Eindhoven.

[50] I. A. Lyulina, R. M. M. Mattheij, A. S. Tijsseling, and A. T. A. M. de Waele. Numerical simulation of pulse-tube refrigerators. *International Journal of Nonlinear Sciences and Numerical Simulation*, 5:79–88, 2004.

[51] R. M. M. Mattheij, S. W. Rienstra, and J. H. M. ten Thije Boonkkamp. *Partial Differential Equations, Modelling, Analysis, Computing*. SIAM Press, 2005.

[52] E. I. Mikulin, A. A. Tarasov, and M. P. Shkrebyonock. Low temperature expansion pulse tubes. *Advances in Cryogenics Engineering*, 29:629–637, 1984.

[53] R. Minero. *Local defect correction for time-dependent problems*. PhD thesis, Eindhoven University of Technologyät, Eindhoven, the Netherlands, 2006. In English.

[54] P. Neveu and C. Babo. A simplied model for pulse tube refrigeration. *Cryogenics*, 40:191–201, 2000.

[55] National Institute of Standards and Technology NIST. *Technical Note 631*. McCarty, 1972.

[56] M. Ohmi, M. Iguchi, K. Kakehachi, and T. Masuda. Transition to turbulence and velocity distribution in an oscillating pipe flow. *Bull JSME*, 25:365–371, 1982.

[57] H. C. Park, E. S. Jeong, and S. Jeong. Two-dimensional model for tapered pulse tubes part 3: unsteady components of second-order mass flux and temperature. *Cryogenics*, 42:485–493, 2002.

[58] R. Radebaugh. Development of the pulse tube refrigerator as an efficient and reliable cryocooler. In W. Hackbusch and G. Wittum, editors, *Numerical Treatment of Coupled Systems*, Institute of Refrigeration, Notes on Numerical Fluid Mechanics, pages 1–27. London, 2000.

[59] A. Razani, T. Roberts, and B. Flake. A thermodynamic model based on exergy flow for analysis and optimization of pulse tube refrigerators. *Cryogenics*, 47:166–173, 2007.

[60] T. Sarpkaya. On the parameter $\beta = Re/kc = D^2/\nu T$. *Journal of Fluids and Structures*, 21:435–440, 2005.

[61] T. Sexl. Uber den von E.G. Richardson entdeckten Annulareffekt (On the annular effect discovered by E.G. Richardson). *Zeitschrift für Physik*, 61:349–362, 1930. In German.

[62] Z. Shaowei, P. Wu, and C. Zhongqi. Double inlet pulse tube refrigerators: an important improvement. *Cryogenics*, 30:514–520, 1990.

[63] PETSc Sientific Computing Software. *Portable and Extensible Toolkit for Scientific Computation software version 2.3.3.* 2007.

[64] W. R. Smith. One-dimensional models for heat and mass transfer in pulse tube refrigerators. *Cryogenics*, 41:573–582, 2001.

[65] P. P. Steijaert. *Thermodynamical aspects of pulse-tube refrigerator.* PhD thesis, Eindhoven University of Technology, Eindhoven, The Netherlands, 1999.

[66] V. V. Sychev and et al. *Thermodynamic Properties of Helium.* Hemisphere Publishing Corporation, 1987.

[67] I. A. Tanaeva. *Low-temperature cryocooling.* PhD thesis, Eindhoven University of Technology, Eindhoven, The Netherlands, 2004.

[68] I. A. Tanaeva and A. T. A. M. de Waele. A small helium-3 pulse-tube refrigerator. *Cryogenics*, 45:578–584, 2005.

[69] A. S. Tijsseling and A. E. Vardy. Time scales and FSI in oscillatory liquid-filled pipe flow. In S. Hunt, editor, *Proc. of the 10th Int. Conf. on Pressure Surges*, pages 553–568, Edinburgh, United Kingdom, 2008. BHR Group.

[70] R. A. Trompert. *Local uniform grid refinement for time-dependent partial differential equations.* PhD thesis, CWI, Amsterdam, The Netherlands, 1994.

[71] B. Van Leer. Towards the ultimate conservative difference scheme ii. monotonicity and conservation combined in a second order scheme. *J. Comp. Phys.*, 14:361–370, 1974.

[72] C. Wang. Numerical analysis of 4 k pulse tube coolers: Part I. numerical simulation. *Cryogenics*, 37:207–213, 1997.

[73] C. Wang. Numerical analysis of 4 k pulse tube coolers: Part II. performances and internal processes. *Cryogenics*, 37:215–220, 1997.

[74] C. Wang, G. Thummes, and C. Heiden. Control of DC gas flow in a single-stage double-inlet pulse tube cooler. *Cryogenics*, 38:843–847, 1998.

[75] C. Wang, P. Y. Wu, and Z. Q. Chen. Numerical modelling of an orifice pulse tube refrigerator. *Cryogenics*, 32:785–790, 1992.

[76] C. Wang, P. Y. Wu, and Z. Q. Chen. Numerical analysis of double-inlet pulse tube refrigerator. *Cryogenics*, 33:526–530, 1993.

[77] F. M. White. *Viscous Fluid Flow, Second edition*. McGraw-Hill, 1991.

[78] M. E. Will. *Counterflow pulse-tube refrigerators*. PhD thesis, Eindhoven University of Technology, Eindhoven, The Netherlands, 2006.

[79] D. W. J. Willems. *High-power cryocooling.* PhD thesis, Eindhoven University of Technology, Eindhoven, The Netherlands, 2007.

[80] D. W. J. Willems and J. A. M. Dam. Three dimensional pulse-tube simulations. *Advances in Cryogenics Engineering*, 47:934–941, 2001.

[81] M. Y. Xu, Y. L. He, and Z. Q. Chen. Analysis of an orice pulse tube refrigerator using the method of characteristics. *Cryogenics*, 39:751–757, 1999.

Index

Acknowledgments

Completing a PhD is truly a marathon event, and I would not have been able to complete this journey without the aid and support of countless people over the past five years. I must first express my gratitude towards my advisors, Professor Dr. Mattheij and Professor Dr. de Waele and my very special appreciation to Dr. Tijsseling for his constant and patient support. Their leadership, help, support and attention to detail were always instructive and kept me enthusiastic about my work. Over the years, I have been funded through a fellowship provided by STW for which I am thankful.

In the Scientific computing group of Prof. Mattheij I had the chance to have several fruitful discussions with numerical analysists. Among all, Dr. Jan ten Thije Boonkkamp was very supportive all the time for any type of numerical problems hitting my mind. In addition, Dr. ir. van der Linden and Dr. ir. Rook were all the time helpful for all the programming issues and other computer-based problems for which I would like to give them my appreciation.

During the last year I was doing research as a Postdoc in the combustion group of Prof. Dr. Roekaerts at TU Delft. During that period, not only I learned a lot of scientific work related to combustion, but also I learned the sense of humor when doing research. In addition, Prof. Roekaerts was so supportive to let me work on my PhD project occasionally. Therefore, I am so thankful to him. I would like to extend words of thanks to Prof. Vardy from the University of Dundee, UK, Prof. Roekaerts, Dr. ir. Jacques Dam of Imtech/TUE for reading my thesis and giving me a lot of delighted comments and constructive remarks which have improved the contents of my thesis a lot. In addition, I would like to give my appreciation to Dr. Wenqing Liang, Southeast University, Nanjing, PR China for the fruitful discussion on our twin project.

Furthermore, I like to be thankful to Enna van Dijk and Marese Wolfs-van de Hurk for their great help with administrative matters and their great and lovely sense of humor.

I would like to thank many PhD and Postdoc students of our group CASA during the four years of my stay, among all Mirela Darau, Darcy Hou, Hans Groot, Yabin Fan, Tasnim Fatima, Malik Furqan, Yves van Gennip, Miguel Patrcio Dias, Shruti Gumaste, Andriy Hlod, Davit Harutyunyan, Zoran Ilievski, Roxana Ionutiu, Godwin Kakuba, Jan Willem Knopper, Kundan Kumar, Agnieszka Lutowska, Oleg Matveichuk, Prof.

Curriculum vitae

The author of this thesis was born on February 24th, 1977, in Shiraz, Iran. He finished his preuniversity education in Physics and Mathematics at Mollasadra high school, Shiraz, in 1994. Ali started studying Civil Engineering at Persian Gulf University and received the Bachelor degree in 1998. Then, he went to Isfahan University of Technology, Isfahan, for doing an MSc in Civil Engineering, Geotechnique and graduated in 2001. The Master project was titled *Numerical study of tapered piles subjected to axial loading*. After that, he started to get working experience at engineering companies for about three years. In 2004 he decided to go back to the academic, but this time with slightly change in discipline and with living abroad. The second MSc in Scientific Computing was awarded to him by the Royal Institute of Technology, Stockholm, in 2005 where he was honored to do his Master project under the supervision of Professor Kreiss. The project was titled *An absorbing layer for non-linear wave equation with first-order formulation*. He decided to continue as a PhD student at Scientific Computing Group of prof.dr. R.M.M. Mattheij at Eindhoven University of Technology in 2006. His research was on the numerical simulation of a cryocooler device, namely the pulse-tube refrigerator, resulting in this thesis. In 2010 he went to the combustion group of Prof. Roekaerts, TUDelft to do his Postdoc. Since May 2011 he works in ASML as a thermal/CFD engineer.